DISTINCT ELEMENT SIMULATION OF THE FEBRUARY 17TH, 2006, LEYTE, PHILIPPINES ROCKSLIDE

PANAGIOTA ASPROUDA

THESIS SUBMITTED TO THE FACULTY OF THE VIRGINIA POLYTECHNIC INSTITUTE AND STATE UNIVERSITY IN PARTIAL FULFILLMENT OF THE REQUIREMENTS FOR THE DEGREE OF

MASTER OF SCIENCE
IN
GEOTECHNICAL ENGINEERING

DR. MARTE S. GUTIERREZ, CHAIR
DR. J. MICHAEL DUNCAN
DR. MATTHEW MAULDON

MAY 8, 2007
BLACKSBURG, VIRGINIA

KEYWORDS: ROCKSLIDE, DISTINCT ELEMENT METHOD, TRIGGERING, RAINFALL-INDUCED FAILURE, DEBRIS FLOW

DISTINCT ELEMENT SIMULATION OF THE FEBRUARY 17TH, 2006, LEYTE, PHILIPPINES, ROCKSLIDE

PANAGIOTA ASPROUDA

ABSTRACT

This study investigates the February 17th, 2006 massive rockslide that occurred in the island of Leyte, Philippines following heavy rainfall and four minor earthquakes. The rockslide is considered one of the largest and most catastrophic slides in the last few decades as it completely inundated the village of Guinsaugon, taking the lives of approximately 1,400 of the 1,800 residents of the village.

The distinct element simulation of the rockslide is performed using 3DEC (Three-Dimensional Distinct Element Code) in order to investigate the underlying triggering mechanism of the slide as well as the behavior of the debris flow. The 3DEC models were established based on field observations from the U.S. Reconnaissance team and material and joint properties based on in-situ and laboratory test results. The possible triggering mechanisms considered in the distinct element analyses were the rainfall-induced hydraulic pressurization of the fault forming part of the main scarp, as well as the seismic acceleration due to the minor earthquakes that occurred the morning of the slide.

The results of the analyses and simulations indicate that the rainfall-induced hydraulic pressurization of the fault was potentially the main trigger for the initiation of the slide. The minor earthquakes, which occurred before and around the time of the slide initiation, appeared to have very little effect on the triggering of the slide. The results of the distinct element numerical analysis of the triggering mechanism and the debris flow are comparable to witness accounts and field observations. The results presented in this study are expected to provide better understanding of rockslides such as the one that occurred in the Philippines on February 17, 2006. With further improvements in computational capabilities in the future, distinct element simulations can have the potential to reliably predict the initiation and behavior of slides, and help mitigate their impact.

ACKNOWLEDGEMENTS

The author wishes to acknowledge the substantial contribution of Dr. Marte S. Gutierrez, Professor at the Department of Civil and Environmental Engineering at Virginia Polytechnic Institute and State University, for his supervision and constructive guidance throughout the completion of this research project.

The author also would like to thank the members of the graduate committee, Professor J. Michael Duncan and Professor Matthew Mauldon, for their comments and suggestions and for reviewing this thesis.

The author wishes to express gratitude towards the faculty of the Geotechnical Engineering program of Virginia Tech who contributed to this project through their support and assistance. The author would also like to thank Dr. Sotirios Vardakos for his assistance with the use of the computer program 3DEC in the beginning stages of the project.

Partial funding for the research described in this thesis was provided by National Science Foundation under grant number 0630474. This support is gratefully acknowledged.

Finally, the author wishes to express her sincere gratitude and appreciation toward her parents Spilios and Sophia Asprouda for their continued encouragement and support, and for providing the vast opportunity for undergraduate and graduate studies at the Department of Civil and Environmental Engineering at Virginia Tech.

TABLE OF CONTENTS

LIST OF FIGURES

LIST OF TABLES

CHAPTER 1: INTRODUCTION

1.1 – BACKGROUND

On February 17th, 2006, at approximately ten in the morning, a massive rockslide occurred in Guinsaugon, Leyte in Philippines. Guinsaugon is a small village in the town of St. Bernard in Southern Leyte, located at the foot of Mt. Cabac. In the morning of the 17th of February, 2006, an overhanging block of Mt. Cabac was detached causing a massive rockslide, which very quickly covered almost the entire village of Guinsaugon (Fig. 1.1). Five days of continuous heavy rainfall between February 8th and February 12th had forced many of the residents of the village to evacuate the area fearful of a destructive landslide. However, the rainfall had decreased dramatically during the five days immediately preceding the slide so residents of Guinsaugon had returned to their normal daily activities.

Witnesses of the event stated that there were “explosion” and “cracking” sounds and only minutes later most of the village was covered in what seemed to be a mixture of wet soil and rock fragments up to 30 m thick in some areas. The local elementary school, which was in session at that time, was covered by debris, burying approximately 300 students and teachers. Tragically, relatives of the students and teachers reported that they were receiving text messages on their cell phones from those trapped in an air pocket under the debris, crying for help. The exchange of text messages stopped after four days since, unfortunately, the location of the school was not certain and the nature of the debris caused rescue operations to be very ineffective.

Overall, it was estimated that the debris, which mainly consisted of mud and boulders, had a total volume of 15-20 million m^3 (Stone, 2006). The area covered by debris was estimated to be approximately 300 hectares (Inter-Agency Committee, 2006) and extended approximately three kilometers from the head of the scarp on the East to the edge of the debris on the West. The nature of the debris made rescue operations almost impossible and the continuous rainfall over one week after the slide made the situation even worse. The soft and unstable debris did not allow heavy machinery to be brought to the site and thus excavations had to be performed by hand. Rescuers, who reached the disaster area almost immediately, were sinking in the mud while trying to

excavate out thousands of people who had been buried by the slide material. Not only were the rescue operations delayed due to the nature of the debris, but also rescuers were unsure of the exact position of their targets. It was later determined that the town had been moved by the force of the debris flow thus making the locating of potential survivors practically impossible.

The Governor of Leyte Province called-off the rescue operations on February 24th, 2006 at which point 122 bodies had been recovered and another 1328 people were reported missing and presumed dead. A total of 560 people survived the event, of which only about 20 were those rescued from the debris. A total of 350 houses were destroyed including elementary school buildings. The Guinsaugon rockslide is the first major debris avalanche of the 21st century, and is considered to be among the largest slides in terms of lives lost and the volume of debris involved.

Fig.1.1 - Scarp on Mt. Cabac and debris extent from the February 17th, 2006, Leyte, Philippines rockslide (USDOD)

1.2 - SCOPE OF WORK AND OBJECTIVES

Landslides have always raised great concerns in the field of geotechnical engineering and engineering geology. Their prediction, prevention and mitigation have challenged engineers and geologists for many years. Unfortunately, landslides can be unpredictable and often times cause great material damages and loss of life. The attempts of engineers and researchers to investigate and understand the underlying causes of landslides in general have been improved by the development of various methods of soil and rock slope stability analyses.

Specifically, methods of rock slope stability analysis other than the limit-equilibrium method have been developed over the past decades for analysis of rock slope failures in which the geological structural of the rock mass is responsible for the instability of the slope (Norrish and Wyllie, 1996). One such method, which has been widely used in analysis of rock slopes, particularly for complicated geological structures, is the Distinct-Element Method. The distinct-element method is now being widely used because of the development of computer programs for distinct-element analyses in two and three dimensions.

The purpose of this report is to examine the conditions under which the February 17th, 2006 Leyte, Philippines rockslide occurred, and to understand the triggering mechanisms of the slide by performing distinct element analysis. The Presidential Inter-Agency Committee report (Inter-Agency Committee, 2006), which was published shortly after the event, mentions two main events that occurred before the rockslide as possible reasons for the slide: heavy rainfall and minor earthquakes. The computer program 3DEC (Three-Dimensional Distinct Element Code) developed by Itasca (1998) is used to perform three-dimensional distinct-element analyses of the slide in order to examine the different possible triggering mechanisms and to determine which mechanism or combination of mechanisms is truly responsible for the massive and deadly Guinsaugon rockslide of February 17th, 2006.

A U.S. Reconnaissance Team, organized and led by Dr. Marte S. Gutierrez, visited the site of the slide in July 2006 and November 2006 to collect field data that would be used in analysis of the slide. The team consisted of students and faculty from

Virginia Tech, Iowa State University and University of Florida. The survey team joined with researchers and scientists from Japan, New Zealand and the Philippines in the field. The purpose of the onsite surveys was to perform geological investigations, obtain soil and rock samples, perform in-situ tests, carry out a DGPS survey and digital photogrammetry. The team also interviewed slide survivors to get a better understanding of the overall behavior of the slide and the debris flow (Gutierrez et al., 2006). Laboratory tests on soil and rock samples obtained in the field were performed and reported by Farmer (2006).

The scope of work of this study involves the use of the results obtained from the site survey and laboratory tests in creating a digital elevation and geological structure model of the slide area using the distinct element analysis computer program 3DEC. The three dimensional distinct element code is used to simulate the February 17th, 2006 Guinsaugon rockslide and study the triggering mechanism(s) of the slide as well as the subsequent debris flow. The two possible triggering mechanisms that will be considered in this study are: a) pressurization of a splay of the Philippine Fault Zone (PFZ), which forms part of the main scarp due to the continuous heavy rainfall in the area prior to the slide, and, b) the four minor earthquakes that occurred in the morning of February 17th, 2006. The effect of each event on the triggering and the behavior of the slide is analyzed using distinct element simulations and the results of this analysis are presented in this report.

The main objective of the distinct element simulations of the Guinsaugon rockslide is to obtain a reliable understanding of the triggering mechanisms responsible for the slide. More specifically, the analysis will try to investigate:

1. The mode of failure of the rock mass, i.e. whether the rock mass failed by overturning or toppling, or by sliding along the failure surfaces,
2. The effects of hydraulic pressurization of the main fault due to water infiltration, and the increased unit weight of the rock , and
3. The effects of the minor earthquakes that happened the morning of the slide, on the triggering of the slide and initiation of the debris flow.
4. The behavior of the debris flow once the slide was initiated.

1.3 - History of Landslide Activity in Southern Leyte

The Southern Leyte region is prone to landslides and flooding due to its natural and geological characteristics (Orense and Sapuay, 2006). Several large landslides and flooding incidences have occurred in the area, mainly due to the tropical climate and heavy rainfall. Geological and geomorphologic studies in the region indicate that the Southern Leyte region, specifically the area around Guinsaugon, has experienced several landslides of different magnitudes in the past, as landslides appear to have been part of the land forming processes in the region. Traces of steep escarpments can be identified on topographic maps and photographs of the area, and can be interpreted as products of past landslides. The presence of large pieces of loose rock debris on the slopes and foot of Mt Cabac supports this interpretation.

One of the most catastrophic events in the area occurred in 1991 when heavy rainfall due to a typhoon caused flooding of the two main rivers in Leyte, the Anilao and Malbasag Rivers. As a result of the flooding, 4,000 people lost their lives and 2,000 more were reported missing. The extreme flooding was attributed to excessive logging of the hills above Ormoc City. In December 2003, approximately three years prior to the February 17th, 2006, Guinsaugon rockslide, a series of landslides occurred in Leyte near the town of San Francisco. The landslide was attributed to heavy rains that caused the hills above the village of Pinut-An failed catastrophically. The resulting gush of water, mud and boulders flowed down the hill sweeping around 400 houses and killing 105 persons.

Due to the extensive rainfalls, several much smaller landslides have occurred close the site of the major landslide prior to February 17, 2006 (Fig. 1.2) The most damaging of these earlier landslides is the one that occurred on February 12, 2006 in the town of Sogod, located about 30 km from St. Bernard, which killed seven people.

Despite the fact that landslides are relatively common in the Southern Leyte area, the February 17th, 2006, Leyte, Philippines rockslide still caught the residents of Guinsaugon village by surprise. Unfortunately, the unpredictable nature of landslides in general has always been the reason for large material damages and the loss of many lives.

Fig. 1.2 - Locations of landslides in Southern Leyte, February12 to 16, 2006 (Inter-Agency Committee, 2006)

1.4 - OTHER MAJOR HISTORICAL ROCKSLIDES

The February 17th, 2006 rockslide occurred on the island of Leyte, Philippines and is considered one of the most catastrophic landslides in the last few decades. The Guinsaugon rockslide is the first major landslide in the 21st century and it is comparable to some of the major slides in recent history, in terms of size and loss of life. Table 1.1 from Stone (2006) summarizes some of the major slides that have occurred recently including the volume of the slide involved and the number of casualties. One of the major landslides in the 20th century includes the 1983 Thistle, Utah slide, which is considered to be the costliest landslide in U.S. history with an estimated amount of $400 million in total losses in 1983 dollars. The Thistle, Utah slide was a result of a wet El Niño winter of 1982-1983.

The largest landslide in the world in terms of volume of debris involved occurred only a couple of decades ago during the 1980 Mt. St. Helens volcano eruption in Washington state, USA. A moderate earthquake caused a huge landslide on the surface of Mt. St. Helens, which completely removed the side, the summit, and the inner core of the volcano, and triggered a series of massive explosions. The scarp that was created was 23 km long and generated 2.8 km^3 of debris that traveled for approximately 100 km away from the scarp (Fig. 1.3).

Another major landslide of magnitude similar to that of the 1980 Mt. St. Helens volcano eruption and landslide is the 1974 Mantaro River, Peru landslide. On April 25th, 1974 a massive landslide, with a volume of $1.6x10^9$ m^3, occurred in the valley of the Mantaro River in Peru. The earth movement caused vibrations equivalent to an earthquake of magnitude 4.5 and the material dammed the Mantaro River forming a lake (Lee and Duncan, 1975). The lake, which was as deep as 170m and approximately 31km long, overtopped the landslide-induced dam on June 1974 flooding the areas downstream. The slide itself killed 450 people while the flooding caused 1,000 people to evacuate their properties and a large number of material damages (Lee and Duncan, 1975).

Another major historical rockslide, similar in size to the Guinsaugon 2006 rockslide, was the Rossberg Landslide of 1806. It occurred in central Switzerland in

September 1806 near the small town of Goldau. It involved a large section of the Rossberg Massif that moved away from the mountain and almost completely covered the town of Goldau. Approximately 300 houses were destroyed and 457 people lost their lives due to the Rossberg rockslide. The volume of the detached rock was estimated to be in the order of ten to twenty million cubic meters. The debris not only covered the nearby town but also filled up part of the Lauerzer See causing a 20-meter high wave, resulting in more deaths in the lakeside villages (Norrish and Wyllie, 1996). After extended debate over the triggering mechanisms of the slide, scientists agreed that the rockslide was caused by excessive saturation of the rock due to melting snow and excessive rainfall in the area.

Table 1.1 - Summary of several recent major landslides (Stone, 2006)

Several Major Debris Avalanches

Year	Country	Triggering process	Volume of material*	Impact
1962	Peru (Ancash)	Unknown	13	4000 to 5000 killed
1970	Peru (Ancash)	Earthquake	30–50	18,000 killed
1980	U.S. (Washington)	Volcanic eruption	1600	World's largest historic landslide; 5 to 10 killed
1997	Montserrat	Lava dome collapse	64	Evacuation in 1996 prevented loss of life
2002	U.S. (Alaska)	Earthquake	10–70	Occurred in isolated national park
2006	Philippines (Leyte)	Rainfall/ earthquake?	15–20	122 killed; 1328 missing and presumed dead

* m^3, in millions.

Fig. 1.3 - May, 1980: Progression of landslide on Mt. St. Helens which triggered volcano eruption, Washington, USA (USGS, 2002)

CHAPTER 2: THE LEYTE ROCKSLIDE

2.1 - LOCATION

The Philippines comprise an archipelago of more than 7,000 islands, called the Philippine Archipelago. It is located between 116° 40' and 126° 34' E. longitude, and 4° 40' and 21° 10' N surrounded by the Philippine Sea on the east, the South China Sea on the west and the Celebes Sea on the south (Fig. 2.1). The capital of Philippines is the city of Manila located on the island of Luzon.

The February 17th, 2006 rockslide occurred on the island of Leyte, Philippines. Leyte island is located in the central part of the Philippine islands (Fig. 2.2). The massive rockslide occurred near a small village called Guinsaugon. Guinsaugon is a small village with approximate population of 1,860 in the town of St. Bernard (Fig. 2.3). The town of St. Bernard is located in Southern Leyte island, approximately 100 kilometers from Tacloban City, which is the capital of the island of Leyte (Fig. 2.2). Tacloban City is located approximately 340 kilometers from Manila (Fig. 2.2).

Fig. 2.3 shows an old picture of Mt. Cabac taken before the landslide of February 17, 2006. The town of Guinsaugon lies at the foot of this mountain range. As can be seen in the picture, the mountain has a very steep slope, and several massive rock overhangs can be observed on the face of the mountain.

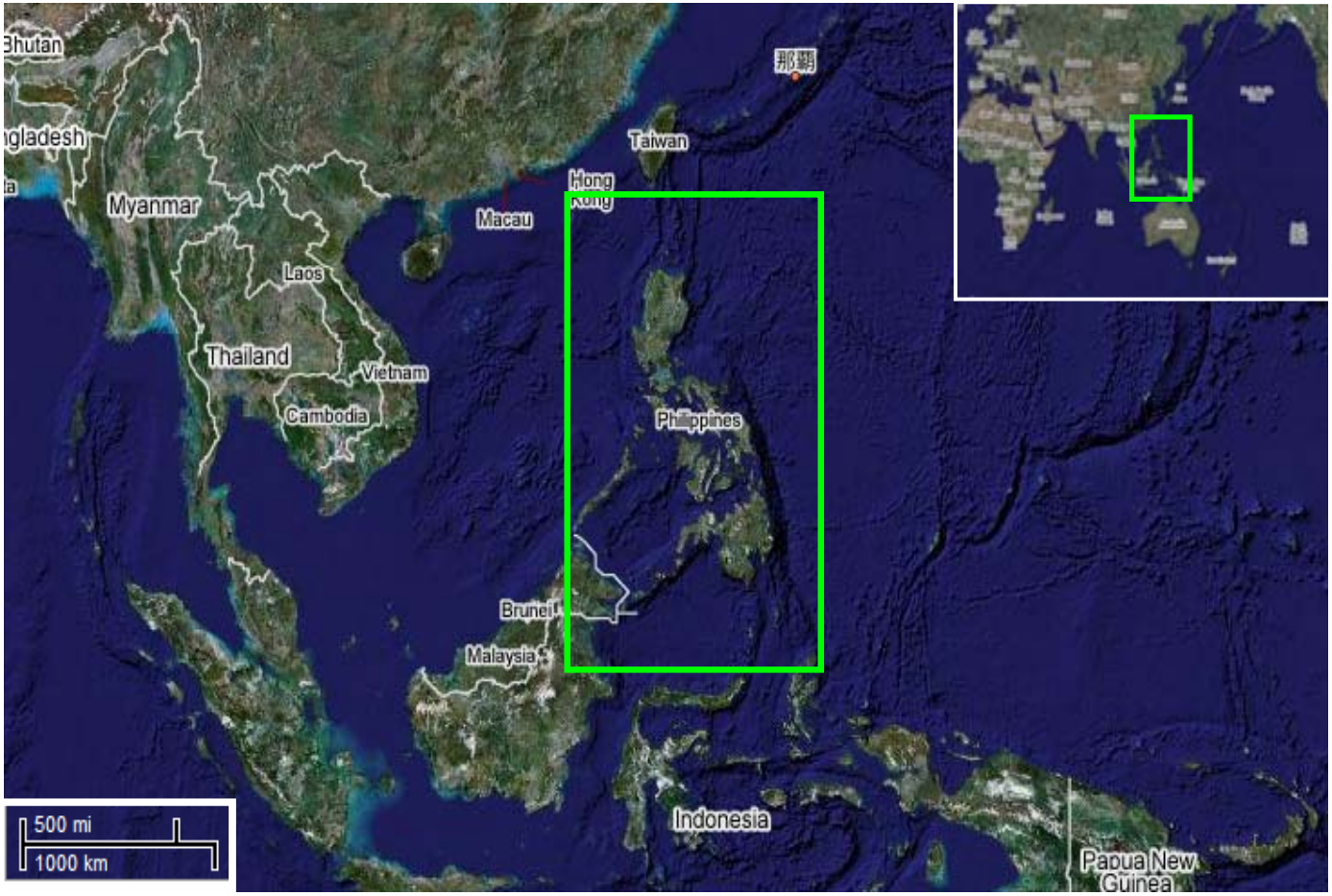

Fig. 2.1 - Satellite image of the Philippine Archipelago (Google Maps, 2007)

Fig. 2.2 - Map of the Philippines showing the island of Leyte and the village of Guinsaugon (Wikipedia, 2007)

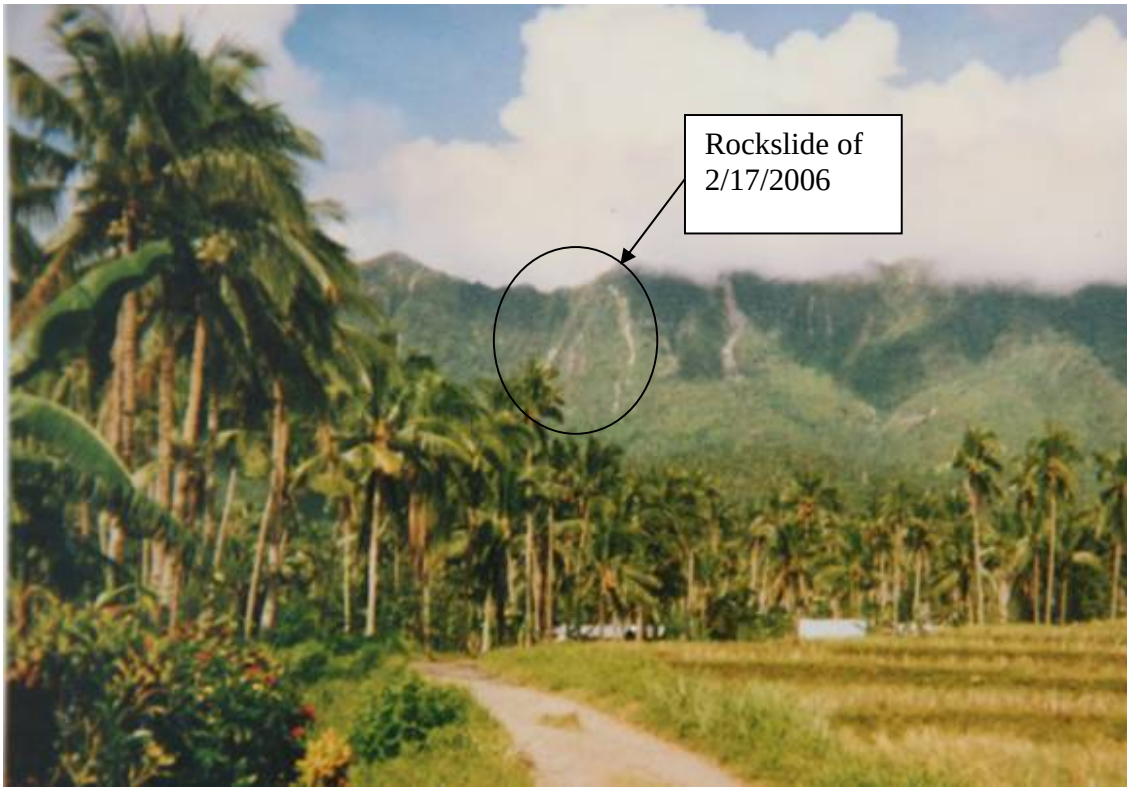

Fig. 2.3 - Picture of Mt. Cabac taken before the February 17, 2007 slide showing several large rock overhangs including the one that became part of the massive February 17, 2007 slide (Gutierrez, 2006)

2.2 - GEOLOGICAL SETTING

The Philippine Archipelago is located at the northwestern edge of the *Pacific Ring of Fire*, and therefore has a very active geologic setting. Its geologic activity is demonstrated by the many active volcanoes in the region, as well as by the frequent seismic events. The Philippines is located at the convergence point of three major tectonic elements: the Philippine Sea Plate, the Eurasian Plate and the Philippine Fault Zone (PFZ).

The Philippine Fault Zone is an active tectonic structure, which runs approximately parallel to the mentioned plate boundaries. It is approximately 1200 km long and runs through the entire Philippine Archipelago from North to South, and it also passes through the town of St. Bernard (Fig. 2.4). The section of the Philippine Fault Zone passing through Southern Leyte is one of the most active segments of the fault system, with an average lateral movement of approximately 2.5 cm per year (Barrier et al. 1991; Besana and Ando, 2005).

Southern Leyte, being a seismically active region, experiences very frequent shallow earthquakes of relatively small magnitude. According to the Inter-Agency Committee (2006), roughly 90 such small magnitude earthquakes have been recorded in the area in a six-year period between January 2000 and January 2006. The area has also experienced a few large magnitude earthquakes in 1907, 1948 and 1984 in the range of M6.4 to M6.9 (Orense and Sapuay, 2006). In contrast with the other sections of the PFZ, the Leyte area is creeping slowly rather than accumulating strain (Duquesnoy et al., 1994), which explains the frequent but shallow and small magnitude earthquakes. An example of the strain accumulating seismic behavior of the northern section of the Philippine Fault Zone is the recent and very catastrophic 1990 Luzon Earthquake (M_w=7.7), which caused the loss of 1,600 lives on and around Luzon island (Velasco et al., 1996).

One reason for the high activity of the Guinsaugon area along the PFZ, in relation to the constant and steady lateral movement of the fault system, is the presence of a series of minor faults, which criss-cross over the area of the town of St. Bernard. Conjugated Reidel-type faults, which are identified by surface lineaments as shown in

Figure 2.5, cross over the main fault in a general northwestern direction (Gutierrez et al., 2006). Additionally, other minor faults that run parallel to the main fault were also identified. Unfortunately, due to the dense vegetation in the area, some of the surface lineaments were not visible and therefore could not be easily identified such that possible fault-related landslide risks could be evaluated. Reconnaissance studies showed that one of the mentioned faults that run along the main PFZ direction was one of the major failure surfaces of the sliding mass responsible for the massive rockslide of February 17, 2006

The rock formations in the area of Southern Leyte are mainly volcanic in origin, fact that can be explained by the volcanic activity of the region in the recent geologic history. The underlying rocks are composed mainly of various layers of volcanic lava flows, including porphyritic andesites and basalts, pyroclastic flows, including tuff breccias, lapilli tuffs and ash tuffs. These volcanic materials are highly susceptible to chemical and physical alterations and thus are generally porous and prone to weathering and erosion (Inter Agency Committee, 2006). These characteristics of the rock materials in the area have strong influence on the behavior of the rockslide and the subsequent debris flow.

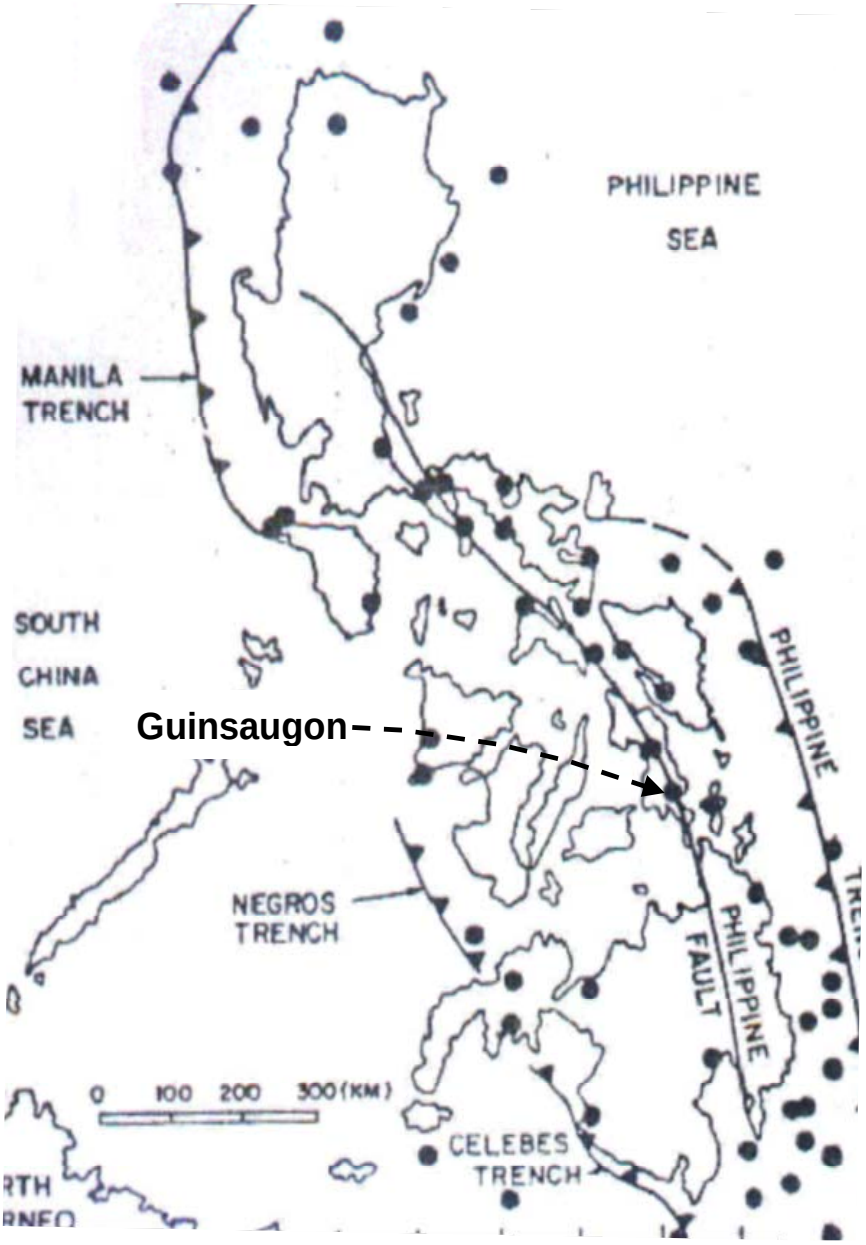

Fig. 2.4 - Map of the Philippine archipelago showing the Philippine Fault Zone (Inter-Agency Committee, 2006).

Fig. 2.5 - Lineaments of the fault system in Southern Leyte
(Gutierrez et al., 2006)

Mt. Cabac is an 800 m high mountain range with very steep slopes passing through Southern Leyte province (Figs. 2.2 and 2.6). Guinsaugon village is located at the foot of Mt. Cabac on the eastern side of the mountain range. The massive slide that occurred between 10:30 am and 10:45 am on February 17th 2006 involved failure of an overhanging rock formation on the eastern slope of Mt. Cabac, above the village of Guinsaugon. Rock overhangs are a general characteristic of the Mt. Cabac formation (Figs. 2.2 and 2.6) and small-scale failures of such blocks are common in the area. However, a large-scale failure of such an overhanging rock formation was not of great concern to the residents of Guinsaugon. They strongly believed that the two small hills at the foot of the mountain would protect the village by preventing potential slide materials from moving further down the slope and becoming a threat to the village and its population.

Fig. 2.6 - Scarp on Mt. Cabac and debris from the Leyte rockslide (USDOD, 2006)

The U.S. Reconnaissance Survey team, organized and led by Dr. Marte S. Gutierrez, visited the site on two occasions to gather field-related data and to get a better understanding of the extent, impact and causes of the slide. From the reconnaissance survey, it was determined that the main scarp created by the rock slide

is approximately 600 m high, 200 m deep and up to 600 m wide at its base. The presence of an overhanging rock formation at that specific section of the mountain was later verified after careful examination of old photographs and topographic maps of the area. An old picture of Mt. Cabac (Fig. 2.2) shows the location of the massive overhanging rock, which was eventually brought down by the rockslide.

The scarp consists of three major failure surfaces, forming a complicated sliding wedge. The main failure surface appeared to be very smooth and reflective (Fig. 2.7). It was initially assumed that the slickensided surface was created during the event of the rockslide, and this assumption was supported by the presence of vertical streaks along the failure surface. After extensive investigation of the main failure surface, it was determined that the initially observed vertical streaks were a result of fine materials sliding along the failure surface rather than due to the slide itself (Gutierrez et al., 2006). Careful examination of the main failure surface and its morphology demonstrated that the main failure is a strike slip fault and that the surface is actually smoother along the horizontal direction and undulated along the vertical direction (Fig. 2.7). This observation lead to the identification of the main failure surface as part of an active fault system, in this case part of the Philippine Fault Zone. The lateral movement along the fault is identified as the cause for the undulations in the vertical direction as well as the smoothness of the surface. The ability of the surface to reflect light was attributed to the fact that rock contained quartzite minerals and thus was very hard as proven by Schmidt hammer rebound tests (Gutierrez et al., 2006).

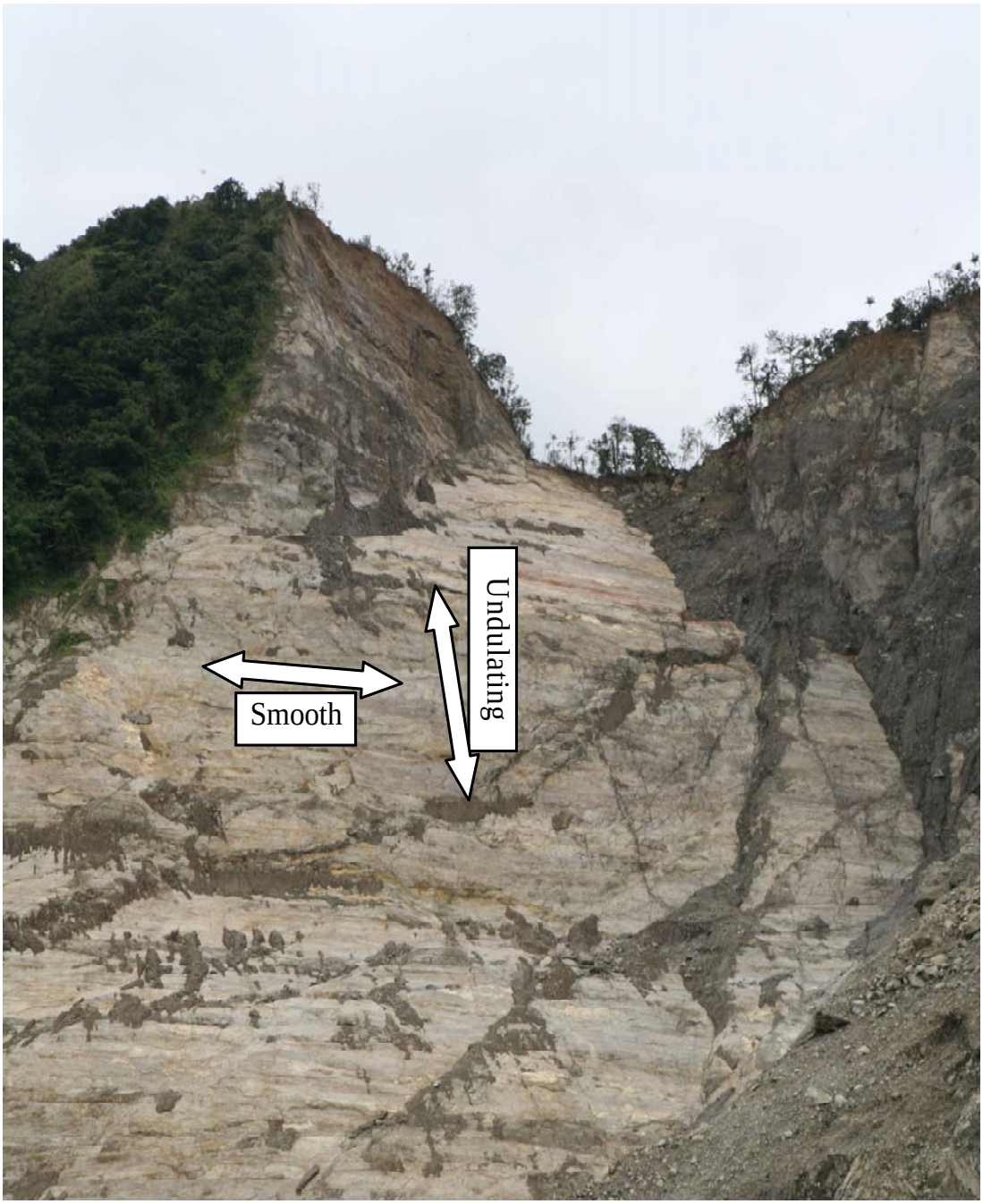

Fig. 2.7 - Photograph of the surface of the fault forming part of the scarp. (Gutierrez et al., 2006)

Once the main failure surface was identified as an active fault part and splay of the PFZ, the assumption that the slide was initiated along the fault was made. Thus, the failure mode responsible for the slide was to be determined. The two possible failure modes in this case were: (a) overturning or toppling, and (b) sliding failures. After investigation of the geological characteristics of the slide, as well as careful consideration of witness accounts of the event, it was concluded that sliding was the most probable mode of failure of the overhanging rock mass. Observation of the geometry and geomorphology of the scarp demonstrated that the rock mass, once triggered, slid along the existing fault and failed by shear on the vertical surface on the north side of the scarp (Fig. 2.8).

Once movement was initiated, another two sliding surfaces were created, forming a valley at the foot of the main scarp, as the rock mass and debris material slid toward the east, cutting through the two small hills located above the village of Guinsaugon. The U.S. Reconnaissance team performed a LIDAR survey of the area to determine the geometry of the scarp to as much accuracy as possible. However, the large amounts of debris material deposited on the scarp surfaces made the survey more difficult and as a result, not all the failure surfaces could be easily identified. The volume of the slide material has been estimated to be approximately 15-20 million m^3.

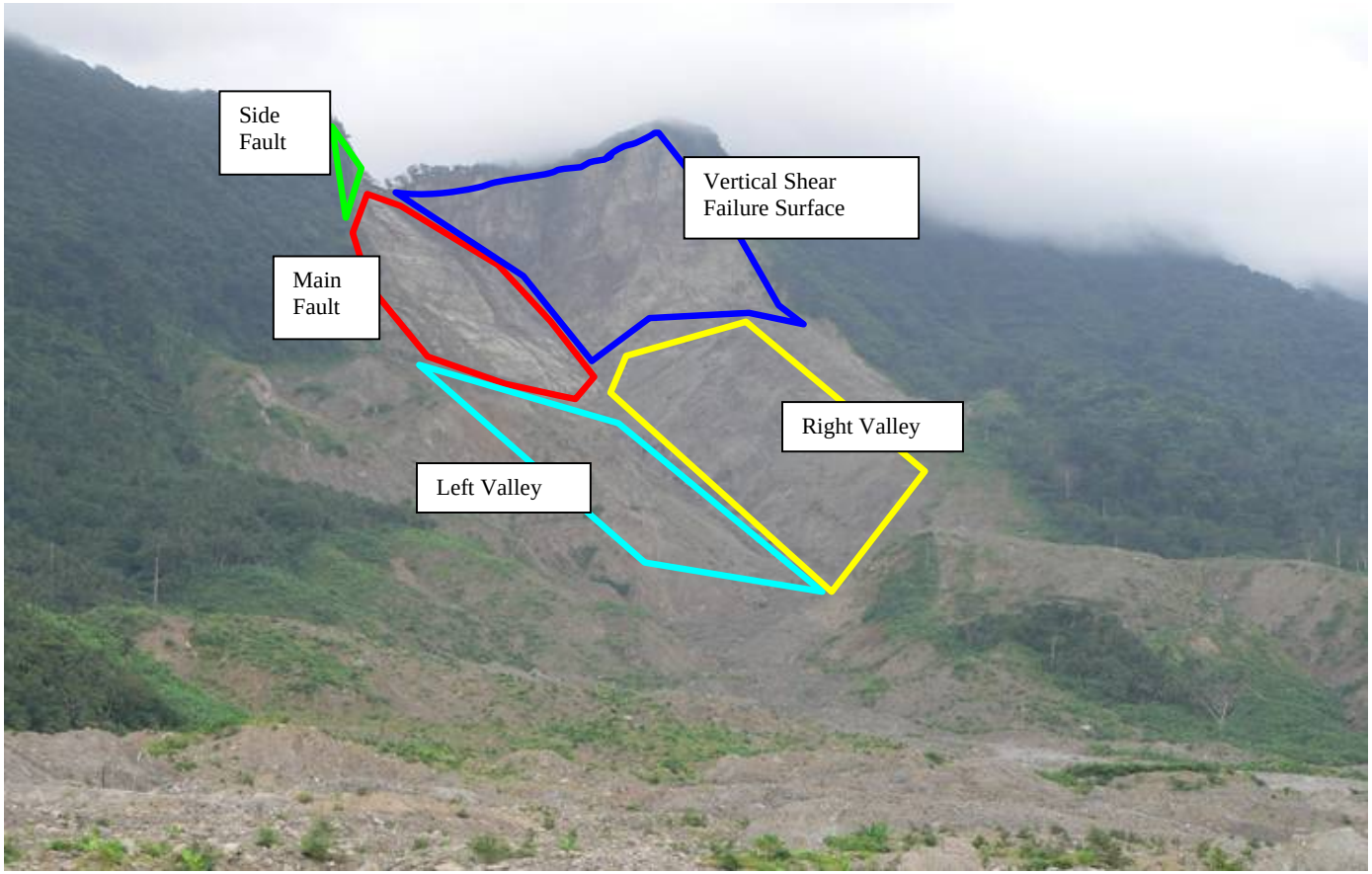

Fig. 2.8 - Escarpment and interpreted failure planes

2.3 - PRECURSOR EVENTS

There has been extended discussion regarding the underlying causes of the Guinsaugon rockslide, and in all cases, the two major events that are being considered as possible triggering mechanisms of the slide are the extensive rainfall and the small earthquakes prior to the slide.

2.3.1 - RAINFALL

Rainfall is the most important climatic element in the Philippines. Rainfall distribution varies greatly throughout the country, depending on the direction of the moisture-bearing winds and the location of the mountain ranges (DOST - PAGASA, 2004). The area of Southern Leyte has always especially been prone to heavy rainfall compared to other areas of the Philippines, a condition explained by the two different climate types present in the area (Inter-Agency Committee, 2006). According to the Climate Map of the Philippines (DOST - PAGASA, 2004), four different climate types have been identified throughout the country (Fig. 2.9). The western side of Leyte Island is characterized by Type IV climate, meaning that rainfall is more or less evenly distributed throughout the year. On the other hand, the southeastern side of Leyte Island is characterized by Type II climate. Type II climate is described as a climate with no dry season and a very pronounced rainfall from November to January. The town of St. Bernard and the surrounding area is characterized by Type II climate condition (Inter-Agency Committee, 2006).

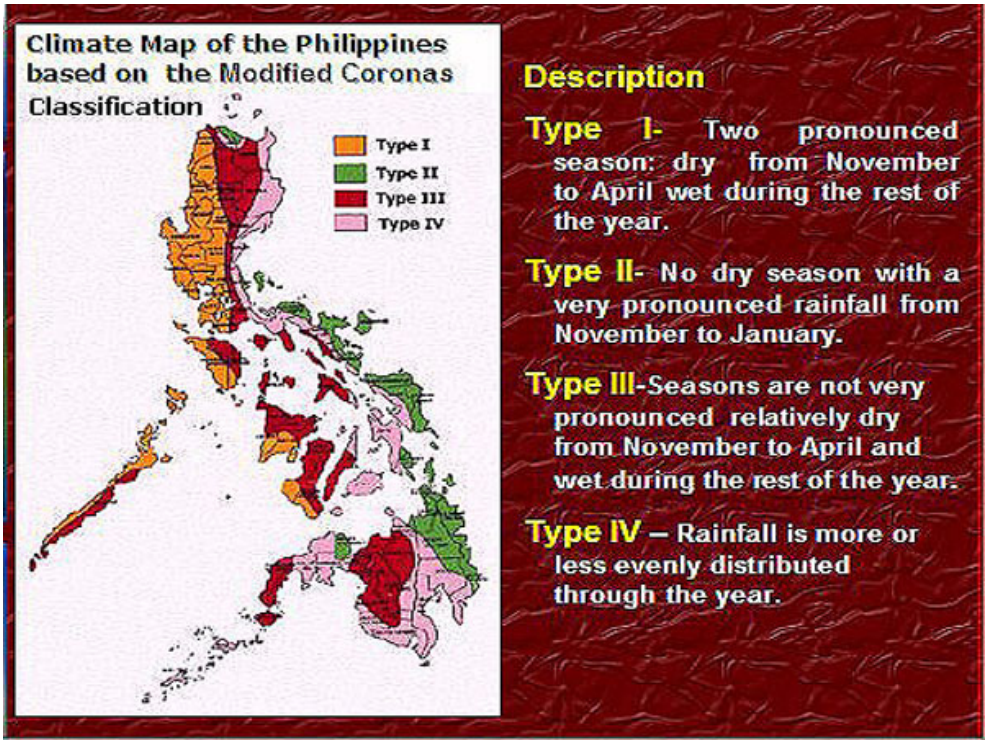

Fig. 2.9 - Climate Map of the Philippines based on the Modified Coronas Classification (DOST - PAGASA, 2004).

The nearest rainfall recording station from the site of the slide, located approximately 7 km from Guinsaugon, in Otikon, Libagnon, recorded approximately 800 mm of rainfall from February 1st until February 17th, 2006 (Fig. 2.10). Records by the Philippine Atmospheric, Geophysical & Astronomical Services Administration (DOST - PAGASA, 2004) indicate that the average monthly rainfall in southern Leyte for the month of February is approximately 290 mm. Thus, it can be seen that the rainfall during the first 17 days of February is approximately three times more than the average monthly rainfall during a normal rainy season in the area (Inter-Agency Committee, 2006). Additionally, the total rainfall during the five-day period of February 8-12, 2006, was approximately twice the average amount of rainfall for the entire month of February in the area.

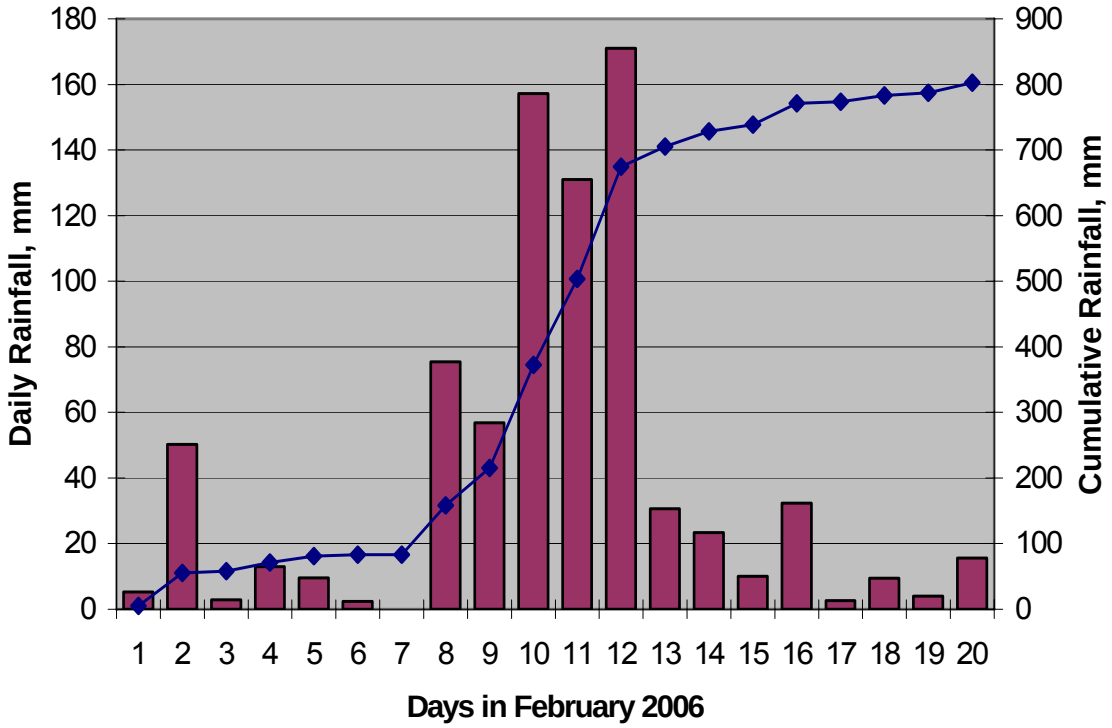

Fig. 2.10: Recorded rainfall in Southern Leyte, February 1-20, 2006 (Inter-Agency Committee, 2006).

The excessive amount of rain during the week prior to the Guinsaugon slide is also recorded and presented in the form of isohyethal contours for the given period of time (Fig. 2.11). The isohyethal analysis clearly shows that the time period of February 7-16 received an excessive amount of rain, approximately 600-700 mm, for that region and time of year, as opposed to a monthly average of 290 mm for February.

The excessive rainfall in the area is attributed to the weather phenomenon in the Pacific Ocean known as La Niña. La Niña is the weather phenomenon characterized by unusually cold ocean temperatures in the Equatorial Pacific, compared to El Niño, which is characterized by unusually warm ocean temperatures in the Equatorial Pacific (NOAA, 2002).

Additionally, according to the Inter-Agency Committee, the recorded rainfall data were taken at a coastal area and it is believed that the actual precipitation at the top of

Mt. Cabac, i.e. at the top of the scarp, would actually be higher than the recorded values due to the orographic effect on rainfall. The orographic effect refers to the tendency of moisture to move from coastal areas upward the steep slope of mountains on the windward side. The reverse air current above the mountain traps the moisture causing the nearly constant presence of rain clouds above steep mountain slopes, otherwise called an inversion zone.

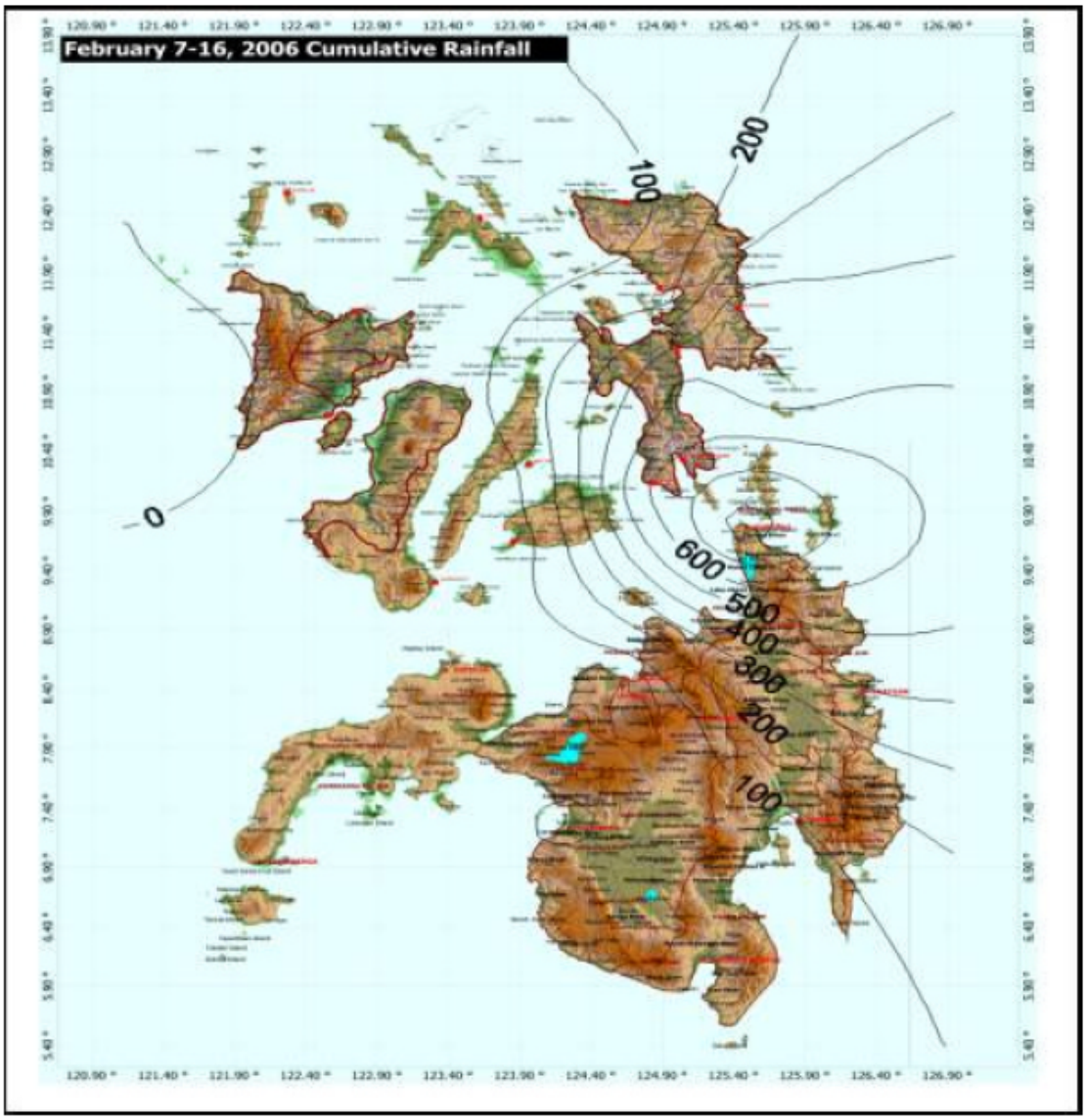

Fig. 2.11 - Isohyethal analysis from February 7-16, 2006. The contour lines indicate locations that received approximately equal amounts of rainfall (DOST - PAGASA, 2004).

Data collected by the NASA's Tropical Rainfall Measuring Mission (TRMM) Satellite proves that the top of Mt. Cabac, in southern Leyte near the town of St. Bernard, is continuously covered by rain clouds as shown in Figure 2.12 (NASA, 2005).

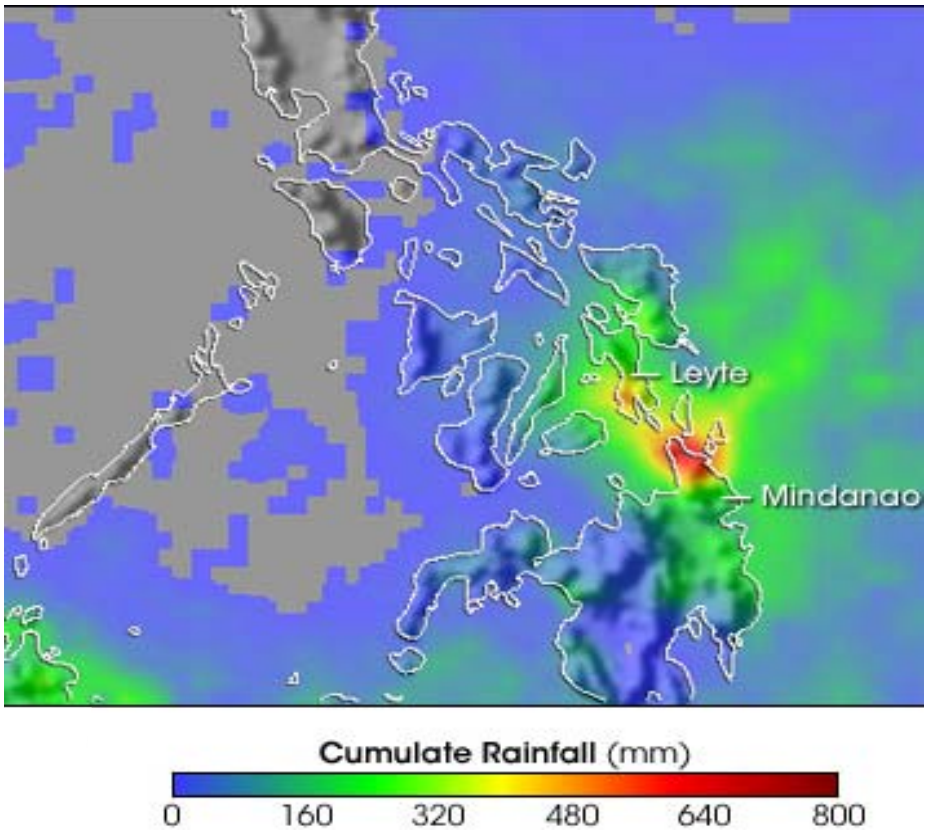

Figure 2.12 - Cumulative rainfall in southern Philippines, for February 4-17, 2006 (NASA, 2005).

The effect of the increased precipitation in the area on the triggering of the slide is the possibility of increasing the pore water pressure in the faults and fractures of the already weathered rock formation. In the case of the fault forming part of the scarp, as identified during the reconnaissance survey, increased pore water pressure would cause reduction of the effective normal stress and thus reduced shear resistance of the fault. This in turn would cause the fault to be activated, and the rock mass under consideration to fail by sliding along the pressurized fault surface. Water springs observed at the foot of Mt. Cabac prior to February 17, 2006 indicate that the rock mass on the face of Mt. Cabac is highly fractured, and that the faults and fractures in the Guinsaugon area are potentially hydraulically interconnected, thus creating passageways for water to flow (Gutierrez et al., 2006). In addition to activation of the fault system, which forms part of

the scarp, the presence of water would increase the unit weight of the overhanging rock, making it heavier and more prone to failure by sliding. Finally, the presence of water in the rock fractures can potentially reduce the shear strength of the faults and fractures as water is known to reduce the frictional resistance of most mineral surfaces (e.g., Lama and Vutukuri, 1978).

The excessive precipitation in the area throughout the month of February 2006 caused numerous flooding incidences and minor slides in the area near Guinsaugon. San Francisco town, north of St. Bernard, was evacuated due to flooding. Pinut-An, San Ricardo, a town along a riverbank was also evacuated. Several highways and roads were closed to traffic due to excessive settlement of the roadway. Several minor landslides also had been occurring over a small period of time prior to the Guinsaugon slide. One of the most serious such landslides occurred in Bgy. Kahupian in Sogod town on February 12th, killing seven people (Inter-Agency Committee, 2006).

Since heavy rainfall and minor landslide events are relatively common in the area, residents took precautionary measures and many evacuated the area for the five-day period between February 8-12, when precipitation was at its peak. The weakened rains following February 12th encouraged the residents of the area to return to their villages. Life was starting to continue as normal, as people thought the danger of a potential slide had disappeared. Unfortunately, the effect the heavy precipitation was seen on February 17th, about four days after the waning of the heavy rains. On the morning of February 17, the overhanging rock was detached from Mt. Cabac, and slid down the mountain in the form of a debris flow, which eventually covered almost the entire village of Guinsaugon and about 1,800 of its residents.

In conclusion, the excessive amount of rainfall appears to play a major role in the triggering of the rockslide and its effect will be considered and further analyzed in the distinct element modeling of the Guinsaugon rockslide.

2.3.2 - EARTHQUAKES

Another possible triggering mechanism for the Guinsaugon rockslide are the minor earthquakes that occurred the morning of February 17th, 2006, with an epicenter near Guinsaugon village. As mentioned previously, the town of St. Bernard is located along one of the most active regions of the Philippine Fault Zone, which is subject to creeping movement without large strain accumulations. The PFZ activity results in frequent and relatively shallow (<10 km depth) earthquakes in the area.

On February 17th, 2006, four minor earthquakes occurred with an epicenter in the vicinity of St. Bernard town. These earthquakes were recorded by the Philippine Institute of Volcanology and Seismology (PHIVOLCS) and were reported in terms of surface wave magnitude, Ms, or body wave magnitude, Mb, or both. The first earthquake occurred at 6:22 am and its magnitude was recorded by PHIVOLCS as Ms=3.3 and Mb=3.2. Its epicenter was estimated to be approximately 10 km northwest of the village of Guinsaugon (Fig. 2.13) which is believed to be too far for it to have a direct effect on the triggering of the slide.

Another three earthquakes occurred almost simultaneously at approximately 10:36 am at different locations but all within 20 km of the location of the slide. The weakest of the earthquakes had a recorded surface wave magnitude of Ms=2.6 and occurred 8 km southwest of Sogod in Southern Leyte, or otherwise 23 km west of Guinsaugon. The other two earthquakes that occurred at 10:36 am were located closer to the scarp and were of larger magnitude. One had a body wave magnitude of Mb=4.5 while the other had a body wave magnitude of Mb=4.3. The epicenter of the latter was located along the PFZ (Fig. 2.13).

According to PHIVOLCS, the maximum peak ground accelerations recorded from the four mentioned earthquakes ranged from 67 to 100 gal, which is equivalent to 0.067g and 0.1g peak ground accelerations. The fact that the earthquakes were shallow and relatively weak raises doubts as to whether or not the earthquakes had some effect on the triggering of the slide. Furthermore, given that the exact time of slide initiation is unknown, one possibility is that the shallow earthquakes recorded at 10:36 am by the PHIVOLCS recording stations originated from the hydraulic pressurization or activation

of the fault splay forming the main slide surface or of nearby faults (Gutierrez et al., 2006). The numerical analysis, through the use of 3DEC, will attempt to explain the effect of the earthquakes preceding the event to the actual fault activation and triggering of the slide, if any.

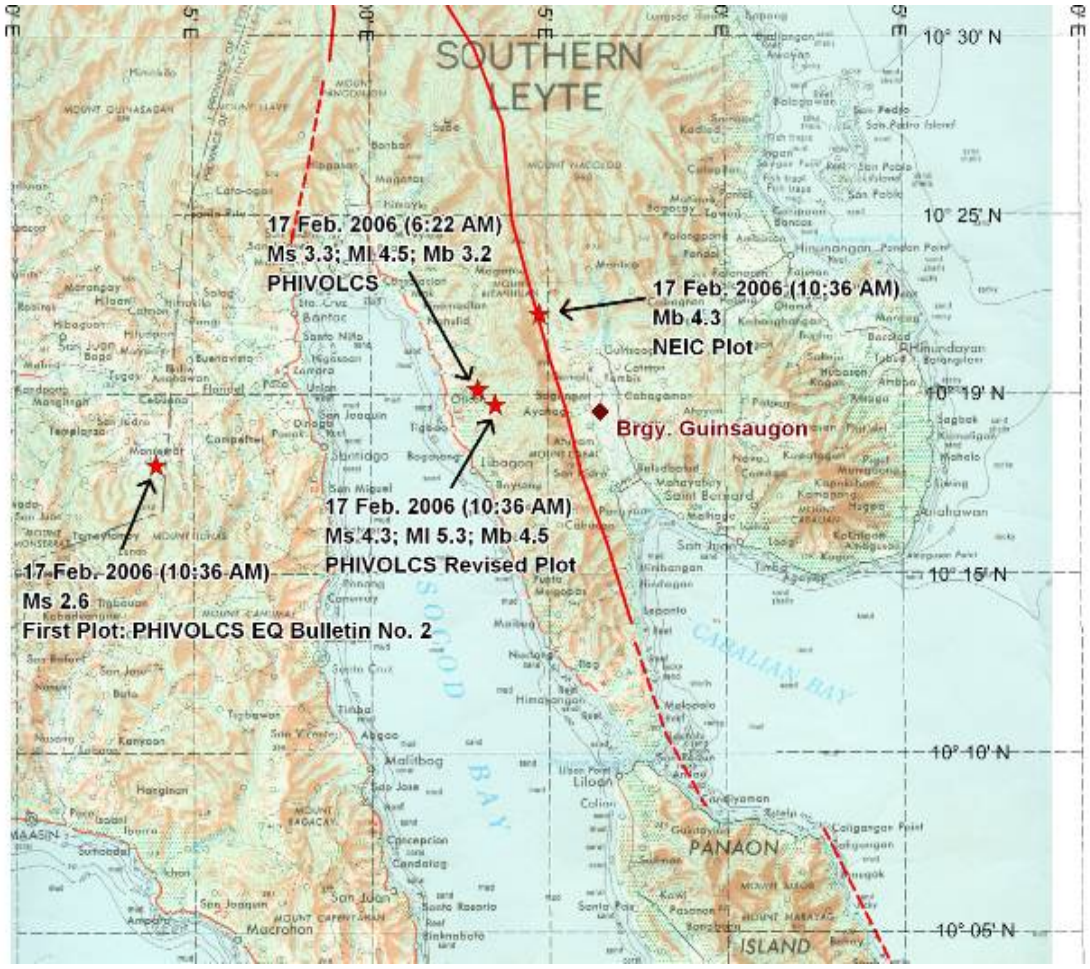

Fig. 2.13 - Recorded earthquakes on February 17, 2006 in Southern Leyte (Inter-Agency Committee, 2006).

2.4 - Characteristics and Distribution of Debris Materials

As previously mentioned, the high seismicity of the area and the large number of faults traversing through the Southern Leyte province have greatly affected the quality of the rock mass in the area. The rock mass in the vicinity of the Philippine Fault Zone are highly fragmented and thus weak and more prone to weathering and erosion. The many fractures in the rock provide passageways for ground water to flow freely within the fractured rock, increasing erosion and weakening of the underlying rock formations. The highly weathered rocks have changed to residual clay, resulting in a thick clayey surface soil formation (Orense and Sapuay, 2006).

The U.S. reconnaissance team surveyed the site and concluded that the debris material consisted of mainly volcanic rocks from the Leyte central highland volcanics, sedimentary rocks of the Calian formation, conglomerates, and breccias generated by the movement along the PFZ (Gutierrez et al., 2006). The nearby 800-m high volcano, Mt. Cabalian, is relatively young and is the source of the volcanic rocks present in the debris material.

The debris material, as witnessed during the site investigation by the U.S. Reconnaissance Team, was described as non-uniform by Gutierrez et al. (2006). Among the debris material are large rock fragments, ranging in size from small rocks to boulders of as much as 3.0 m in diameter (Fig. 2.14). Additionally, among the large rock fragments, several mounds of soil were observed, also ranging from 0.5 m to 3 m in height. These unusual soil mounds were conical in shape and seemed to be formed by large boulders covered by fine soil material, forming a conical shape (Fig. 2.15). Another explanation regarding these soil mounds is that large blocks of conglomerate materials shattered into a soil mound on impact with the ground. The hypothesis proposed by Gutierrez et al. (2006) is that these conglomerate materials were ejected from the slide and disintegrated upon contact with the ground, or the large conglomerate blocks rolled to their final position and later on disintegrated due to rainfall. The fact that these mounds consisted of only disintegrated materials was later verified on a second field survey. Three months later after the first survey, these mounds have been washed by flowing water and can no longer be found.

Fig. 2.14 - Large boulder found among the debris materials (Gutierrez, 2006)

Fig. 2.15 - Mounds of debris materials possibly created from impact of deposited conglomerate with the ground (Gutierrez, 2006)

The overhanging rock of Mt. Cabac that failed by sliding subsequently disintegrated into a debris flow. The U.S. Reconnaissance team performed a DGPS survey to verify the extent of the debris material as it was initially estimated based on a composite of satellite mapping (UNOSAT, 2006) and a LIDAR survey (DPRI, 2006). It was determined that the debris traveled as much as 2.5 to 3.5 km from the base of the scarp to the east and spread in the north-south direction by up to 1.5 km (Fig. 2.16). The debris material thickness as deposited on top of Guinsaugon village varied greatly, with an average of about 5 m in most areas but as much as 30 m thick near the base of the slope. The information regarding the extent and thickness of the debris was used to obtain an initial estimate of the volume of material involved in this massive rockslide, which was approximately 15 to 20 million cubic meters of material (Orense and Sapuay, 2006). The velocity of the slide was estimated to be about 100 to 140 km/h, which was sufficient to create a force, which possibly displaced structures in the village of Guinsaugon by as much as 600 meters. All 350 houses and structures in the village were covered and only few remains could be seen at the edge of the debris.

The event under consideration can easily be described as a rockslide, since it involved failure of a rock mass, which due to extensive fragmentation, weathering and erosion, disintegrated into a debris flow soon after initiation of the slide. The highly fragmented rock material gained substantial acceleration and moved down the slope in a mud-like fashion, cutting through the two hills above Guinsaugon village, which people believed were large enough to protect the village from a potential slide event. The fluid-like manner by which the debris flowed downhill was the reason why the slide was later characterized as a rockslide–debris avalanche by Lagmay et al. (2006).

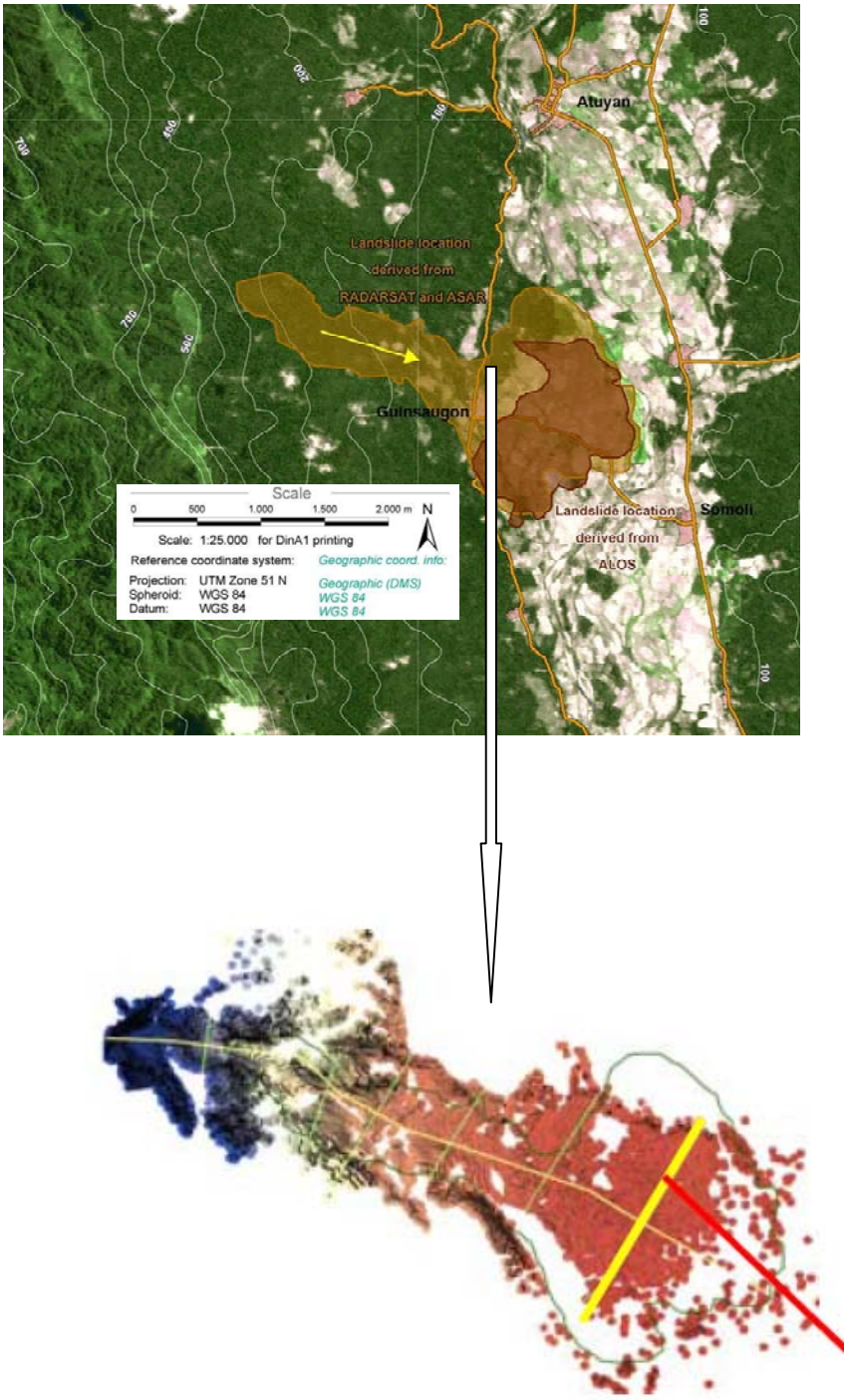

Fig. 2.16 - Extent of the combined scarp and debris area from Satellite imaging (top) (UNOSAT, 2006), and LIDAR survey (bottom) (DPRI, 2006).

2.5 - WITNESS ACCOUNTS OF THE SLIDE

According to the Inter-Agency Committee (2006) report, people reported hearing "cracking" and "explosive" sounds coming from the mountain as well as experiencing ground vibrations on the morning of February 17th, 2006. The cracking and explosive sounds were most probably a result of rock and soil material being detached from the mountain and beginning to move downhill. On the other hand, some people reported that there were absolutely no warning signs of the slide, which could provide a clue to some about the upcoming disaster (Gutierrez et al., 2006). Despite the different opinions on the existence of warning signs prior to the slide, all residents of the area were caught unaware of the disaster which was to fall upon them.

The U. S. Reconnaissance Team while visiting the site in June 2006, had the opportunity to interview a few of the witnesses and survivors of the slide. The purpose of witness accounts was to get a better understanding of the behavior of the slide. Mr. Virgilio Monghit was one of the people who witnessed the slide and survived, and provided very useful information on the event as it was developing. According to Mr. Monghit, he witnessed this terrifying event from 20 m away from the southern side of the scarp, where he was taking care of his banana and coconut cultivations. He said that he felt "ground shaking from an earthquake" only a few minutes prior to the slide, possibly due to an earthquake or due to the triggering of the slide itself. Then, a loud noise similar to that of a "jet engine" was heard as the overhanging block detached from the mountain. He actually mentioned that it seemed to be a sliding failure mode, rather than a toppling or overturning failure mode (Gutierrez et al., 2006).

Once the mass started to move down the slope, it cut through the two small hills above the village, forming a "valley" through which the debris material flowed. Mr. Monghit also mentioned that the rock mass moved in a "wave-like fashion" once movement was initiated, and prior to disintegrating into smaller fragments of rock and conglomerate materials and flowing even further. Apparently, a large dust cloud was formed above the area, indicating that the material was possibly relatively dry. Furthermore, Mr. Monghit as well as other witnesses mentioned seeing boulders "flying" and "hopping" above the ground. He also mentioned that he was "thrown to the ground"

possibly by the energy released, which also caused the ground to heave and pushed the witness a few inches from the ground.

When the dust settled, Mr. Virgillio Monghit saw the entire village of Guinsaugon covered by soil and rock material and realized that he lost his wife and six children some of which were perhaps were attending the local elementary school in the area. Slide survivors reported receiving text messages from students and teachers buried in the school for four days in a row crying for help. Unfortunately, rescue operations were unsuccessful since rescuers realized that the school might have moved and hand digging, the only means of excavation due to the soft and unstable debris, was very slow and inefficient way of finding the school. Tragically, the text messages stopped after four days (Gutierrez et al., 2006).

CHAPTER 3: THE DISTINCT ELEMENT METHOD

3.1 - GENERAL

The analysis of rock slope stability is a two-part procedure. Determination of the geological structure of the rock mass under consideration is a key factor in proceeding with the analysis. The first step of the procedure is determining if the discontinuities in the rock mass can result in instability of the rock slope under investigation, and is referred to as kinematic analysis (Norrish and Wyllie, 1996). If such a failure mode is possible, the second part of the procedure is a limit-equilibrium stability analysis in determining the factor of safety of the rock slope under consideration.

However, the need for stability analysis of slopes, where a kinematically possible failure mode is not present, lead to the development of other methods of analysis, such as the Distinct-Element Method. Unlike other methods of analysis of rock slopes, the distinct element method does not require a prescribed failure surface in order to reach a solution. The method uses an iterative procedure to model failure of slopes as it progresses, by calculating the contact forces between individual stable and unstable blocks (Norrish and Wyllie, 1996).

The development and formulation of the distinct element method has progressed over a period of 25 years, beginning with an initial representation by Cundall (1971) and followed by Cundall (1987), Cundall (1988), and Lorig et al. (1991). Lorig et al. (1991) describes the three main aspects of the distinct element method that differentiate it from other numerical analysis methods.

- The rock mass is composed of individual blocks, which can experience rotation forces and displacements relative to each other, in addition to the normal and shear components.
- Changes in each individual block's geometrical configuration cause generation of interaction forces between the blocks.
- The solution scheme is explicit in time.

A distinct element analysis can be very useful when slope displacement predictions are needed, since it provides the sequential positions and velocities of each

block (Fig. 3.1). The calculation procedure utilized by the distinct element method solves the equations of motion in terms of block acceleration and contact forces for each individual block in the model. Block-to-block interaction at contact points is modeled by contact strength and deformation laws. The method can also incorporate reinforcing elements, which is useful in analyzing foundation loading on rock, as well as perform dynamic analysis using earthquake records and other dynamic load histories. Static problems can be analyzed by applying artificial material damping to achieve steady-state solution by gradually dissipating the transient components of motion. The development of computer programs that implement the distinct element method in two and three dimensions has greatly improved the usability of this analysis method (Norrish and Wyllie, 1996).

Distinct element modeling is being increasingly applied to the analysis and modeling of landslide cases, in particular through the use of the two-dimensional DEM code UDEC (Universal Distinct Element Code) by Itasca Consulting Group Inc. UDEC is being extensively used by many researchers in analysis of different types of slope failures. However, three-dimensional distinct element analyses are only being used in few cases since the simulations are difficult. So far the only commercially available code for 3D DEM is 3DEC, also by Itasca Consulting Group Inc.

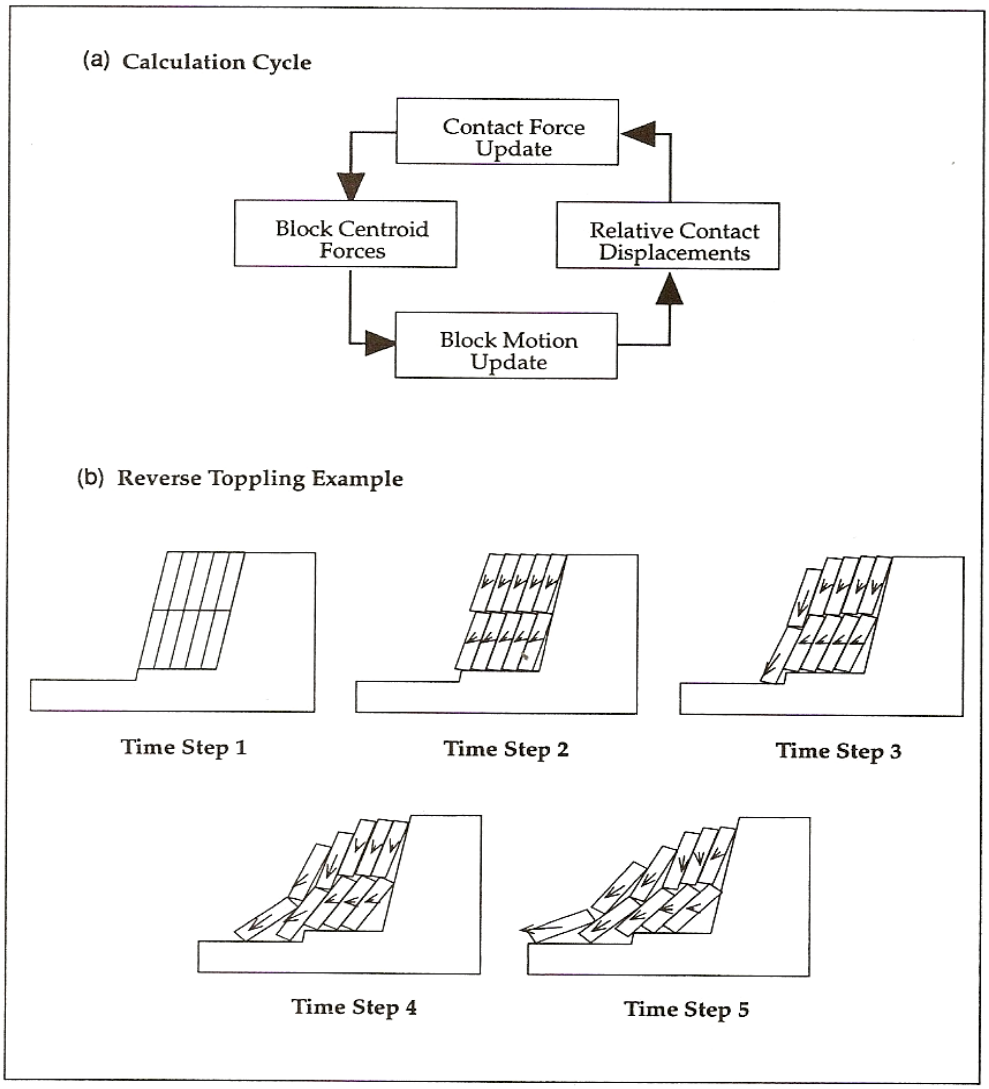

Fig. 3.1 - Distinct element modeling (Lorig et al., 1991)

3.2 – 3-D DISTINCT ELEMENT CODE (3DEC)

3.2.1 - OVERVIEW

The distinct element computer code employed in analyzing the Guinsaugon rockslide is 3DEC Version 2.00 by Itasca Consulting Group Inc. (1998). 3DEC is a three-dimensional numerical program based on the distinct element method for discontinuum modeling. Itasca Consulting Group Inc. (1998) bases the development of 3DEC on the extensively tested numerical formulation used by the two-dimensional numerical program UDEC (Itasca, 1996).

The distinct element code 3DEC represents a discontinuous media, such as a jointed rock mass, as an assemblage of discrete blocks and simulates their response when subjected to static or dynamic loading. The discontinuities, such as joints, cracks, faults and fractures in a rock mass, are treated as boundary conditions between the blocks. The code allows large displacements and rotation of the discrete blocks, which can be either rigid or deformable. Deformable blocks are further divided by a mesh of finite difference elements, each of which responds according to a prescribed linear or non-linear stress-strain law. Linear or non-linear force-displacement relations also govern the relative motion of the discontinuities in both the normal and shear directions. Several material behavior models are built in 3DEC for both the intact blocks and discontinuities (Itasca, 1998).

The distinguishing features of 3DEC according to Itasca (1998) are the following:

- The rock mass is modeled as a 3-D assemblage of rigid or deformable blocks.
- Discontinuities are regarded as distinct boundary interactions between these blocks; joint behavior is prescribed for these interactions
- Continuous and discontinuous joint patterns can be generated on a statistical basis. A joint structure can be built into the model directly from the geologic mapping.
- 3DEC employs an explicit-in-time solution algorithm that accommodates both large displacement and rotation and permits time domain calculations.

- The graphics facility permits interactive manipulation of 3-D objects. The user can instantly view the 3-D model, which greatly facilitates the generation of 3-D models and interpretation of results.

3.2.2 - COMPARISON WITH OTHER METHODS

In comparing 3DEC to other analytical methods, it is important to state the differences between the distinct element method and other numerical methods such as finite element, finite difference, boundary element and discrete element methods.

Computer programs implementing numerical methods, such as the finite element method, the boundary element method and the Lagrangian finite difference method, have interface elements that enable them to model discontinuous material to only some extent. According to Itasca (1998), their formulation is restricted in the following ways:

- The logic may break down when many intersecting interfaces are used,
- There may not be an automatic scheme for recognizing new contacts, and
- The formulation may be limited to small displacements and/or rotation.

Itasca (1998) states that the name “discrete element method” applies to a computer program when it encompasses the following:

- Allows finite displacements and rotations of discrete bodies, including complete detachment, and
- Recognizes new contacts automatically as the calculation progresses.

Cundall and Strack (1979) introduced the term “distinct element method” as the particular discrete element scheme that uses deformable contacts and an explicit time-domain solution of the original equations of motion. According to Itasca (1998), there area four types of computer programs that follow the proposed definition of a discrete element method as defined above.

1. Distinct Element Programs: Such programs use explicit time-domain to solve the equations of motion directly. Individual blocks may be rigid or

deformable, while discontinuities are deformable. A distinct element program that falls under this category is 3DEC (Itasca, 1998).

2. Modal Methods: This method is similar to the distinct element method for rigid bodies, but in the case of deformable bodies modal superposition is used.
3. Discontinuous Deformation Analysis: This method considers all contacts to be rigid but bodies may be rigid or deformable. The condition of no-interpenetration is achieved by an iteration scheme. The body deformability comes from superposition of strain modes.
4. Momentum-Exchange Methods: This method considers both contacts and bodies to be rigid. Momentum is exchanged between two contacting bodies during and instantaneous collision. Frictional sliding can be represented.

3.3 - USE OF 3DEC IN THE ANALYSIS OF THE GUINSAUGON ROCKSLIDE

The main purpose of 3DEC is for analysis of rock engineering projects, including analysis of the progressive failure of rock slopes to analysis of rock joints, fractures and bedding planes and their influence on underground excavations and rock foundations (Itasca, 1998). It is primarily used to study the effect of discontinuities of rock on the modes of failure of rock slopes. 3DEC allows manual and automatic joint generation to better represent the joints, fractures, cracks and bedding planes of a rock mass.

In case of the February 17th, 2006, Leyte, Philippines rockslide, the overhanging rock mass and the involved faults and fractures were modeled in 3DEC. The discontinuous rock mass was discretized into individual blocks of intact materials that are allowed to interact with each other along the discontinuities between the blocks. The rock mass discontinuities modeled in the Guinsaugon rockslide simulation were the faults present in the area, the rock joints and fractures identified during the U.S. Reconnaissance Team site survey, as well as the bedding planes.

The discontinuities were modeled as spring and dashpot contact elements to better describe the stiffness and damping properties of the faults and fractures. All contacts have linear normal and shear stiffness components, while elastoplastic contacts can have, in addition, frictional, cohesive, tensile and dilation properties prescribed to them. The joint characteristics and material properties used in modeling the Guinsaugon rockslide in 3DEC will be analyzed in more depth in the following sections.

As previously mentioned, intact blocks can be rigid, elastically or elastoplastically deformable. 3DEC allows for five different material models for deformable blocks which are built in the code itself, ranging from the “null” block material, representing holes, to the shear yielding model, representing strain-hardening/softening behavior and non-linear, irreversible shear failure (Itasca, 1998). The specific model used in the Guinsaugon rockslide 3DEC model will be further analyzed in the following sections.

CHAPTER 4: DIGITAL ELEVATION MODEL IN 3DEC

4.1 - GENERAL

The first step in creating the 3DEC model that will be analyzed is to develop a digital elevation model of the area prior to the slide. First, an existing topographic map of the area was obtained. The computer program Tracer v. 1.61 (Karolewski, 2002) was used to digitize the existing topographic map for it to be modeled in 3DEC. In order to get a more clear representation of the area, the data collected from the digitizing process was entered and plotted using the computer program Matlab 7.0, R14 (The Mathworks Inc., 2005).

The coordinate system was set at a defined point on the topographic map, used consistently throughout the model preparation to ensure that the correct scale was used at all times. Since the position of the origin of the X-, Y-, and Z-axis was set arbitrarily, the axes serve only to explain the dimensions of the model, rather than its actual position in the field. However, the elevation, measured in the Z-axis, is the actual field elevation measured from mean annual sea level (MASL), ranging from 0 to 800 meters in this case. It must also be specified that in the coordinate system used by 3DEC the axes running along the height of the model specifying elevation is the Y-axis rather than the Z-axis used in Cartesian coordinate system. In order to avoid confusion from this point forward, the dimensions will be specified in terms of the 3DEC coordinate system. According to the 3DEC coordinate system, the X-axis runs along the East-West direction in the field (positive towards the East), the Z-axis runs along the North-South direction (positive towards the North), and finally the Y-axis specifies Elevation. Capital letters X, Z, and Y will be used from this point to refer to the axes used by 3DEC. Fig. 4.1 graphically represents the 3DEC coordinate system in relation to the orientation of the site for clarification.

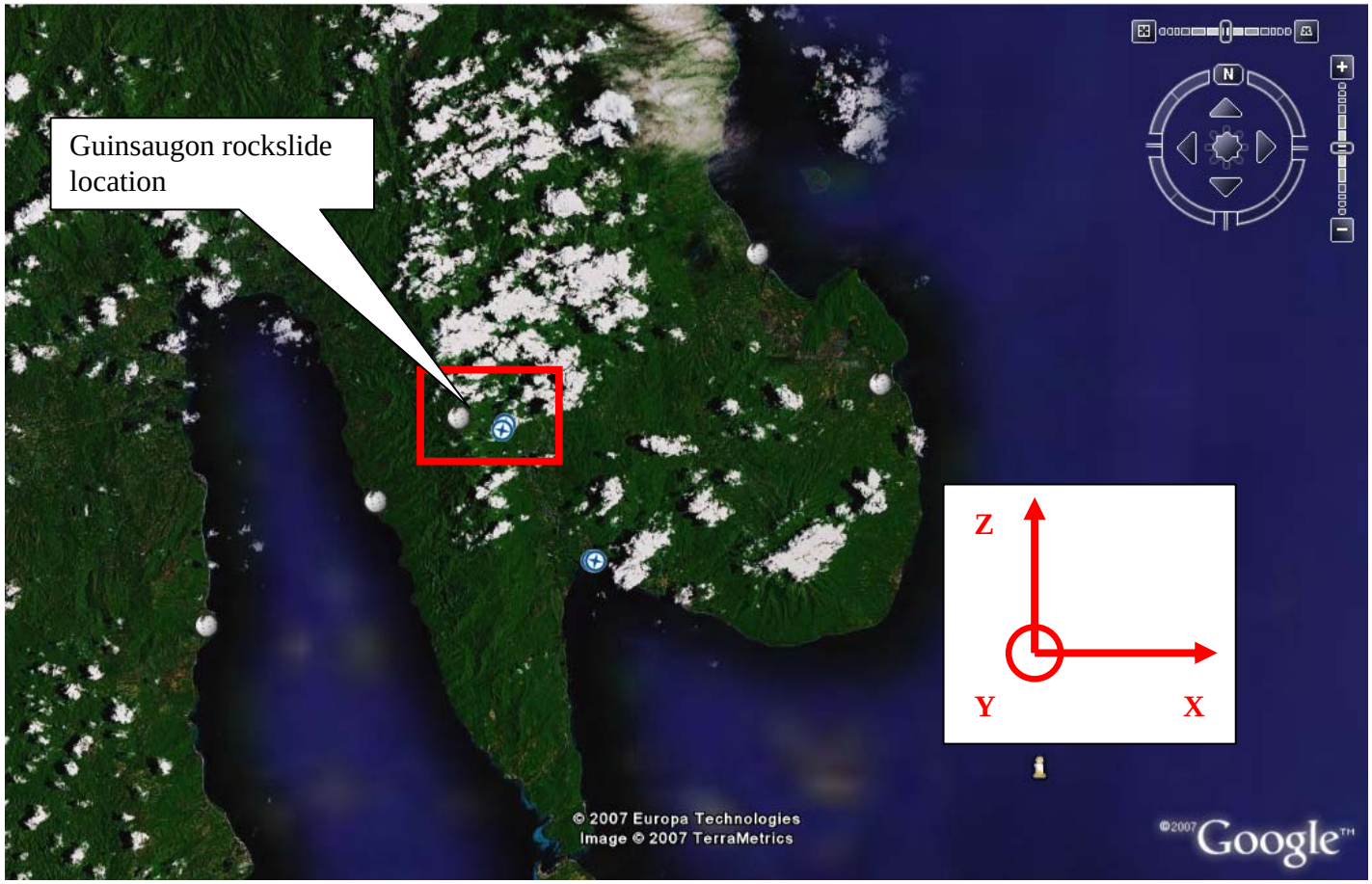

Fig. 4.1 - Site Location and graphic representation of 3DEC coordinate system used in developing digital elevation model of the Guinsaugon slide (Google Earth, 2007)

The area around the sliding block that was chosen to be included in the digital elevation model is 2,800 m in the East-West direction (X- axis) and 2,200 m in the North-South direction (Z- axis). The model ranges in elevation from 50 m to 800 m, which corresponds to the actual elevation of the rock slope involved in the Guinsaugon slide. A graphical representation of the digital elevation model of the area prior to the slide is shown in Figs. 4.2a and 4.2b generated in Matlab 7.0. The corresponding contours of the pre-slide situation on the eastern slope of Mt. Cabac, above Guinsaugon village, are shown in Fig. 4.3. It must be noted that the accuracy of the available pre-slide topographic map, which was used to generate the pre-slide digital elevation model, was limited. Thus, the pre-slide model, and consequently the post-slide model are not accurate to the extent that it would be desirable.

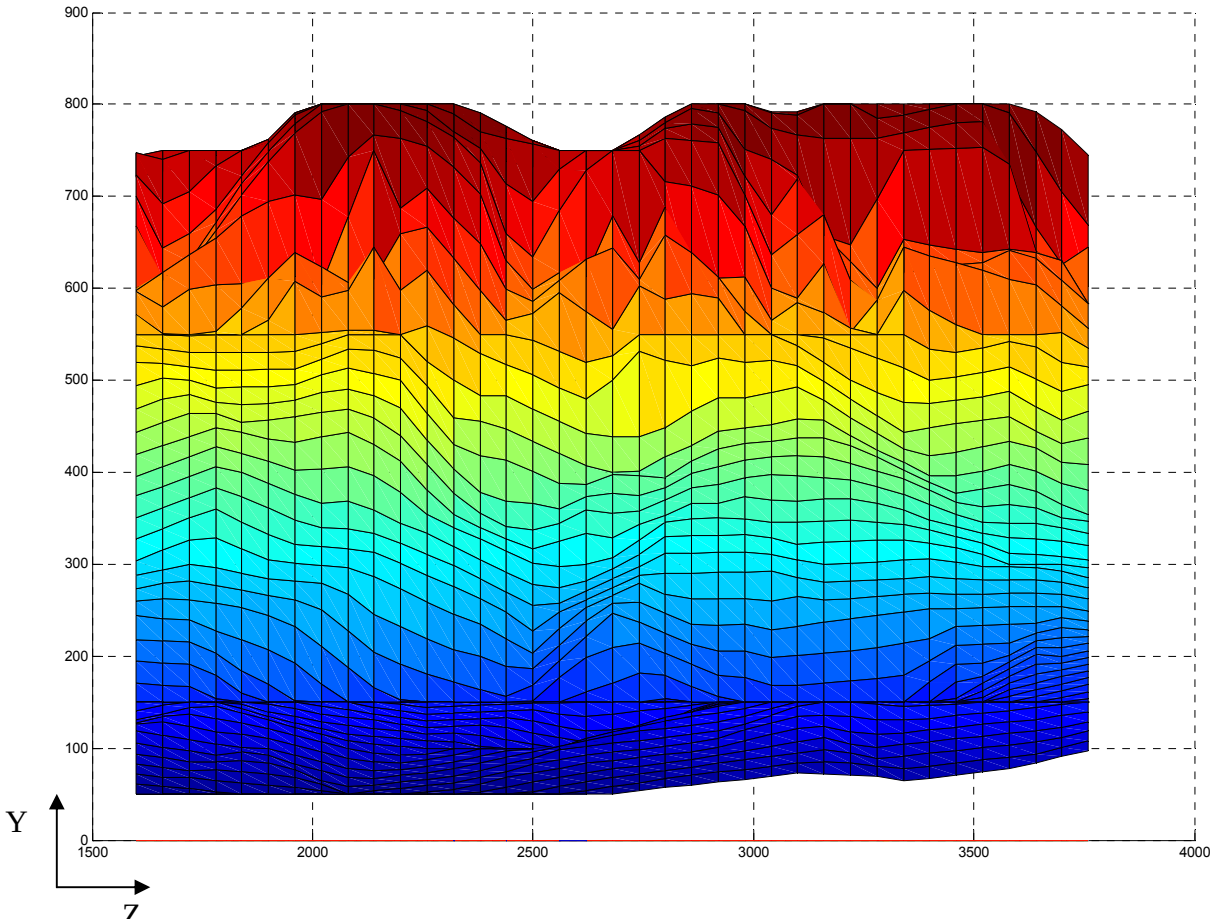

Fig. 4.2a - Graphical representation of the eastern slope of Mt. Cabac involved in the Guinsaugon slide, prior to February 17th, 2006.

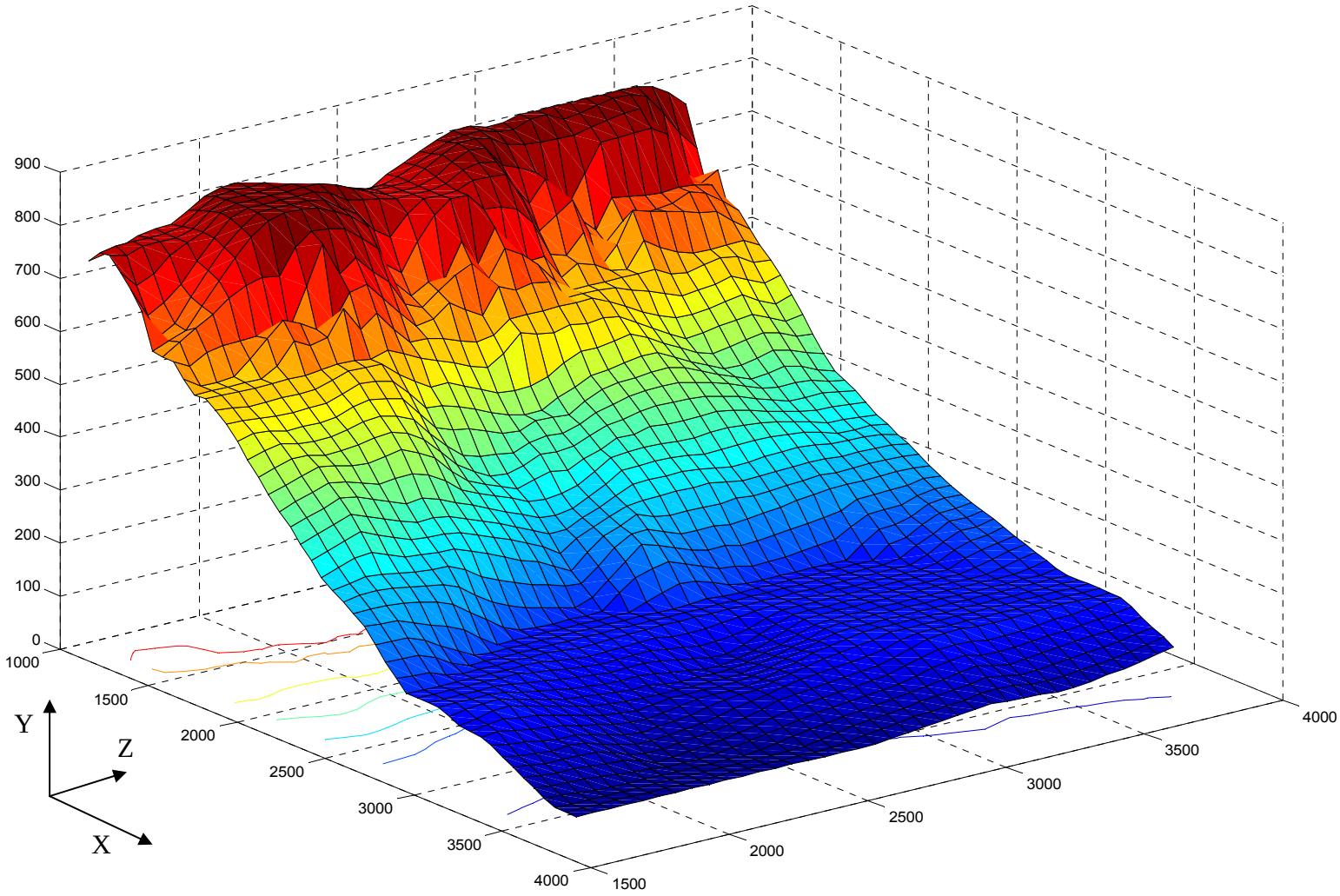

Fig. 4.2b - Graphical representation of the eastern slope of Mt. Cabac involved in the Guinsaugon slide, prior to February 17th, 2006.

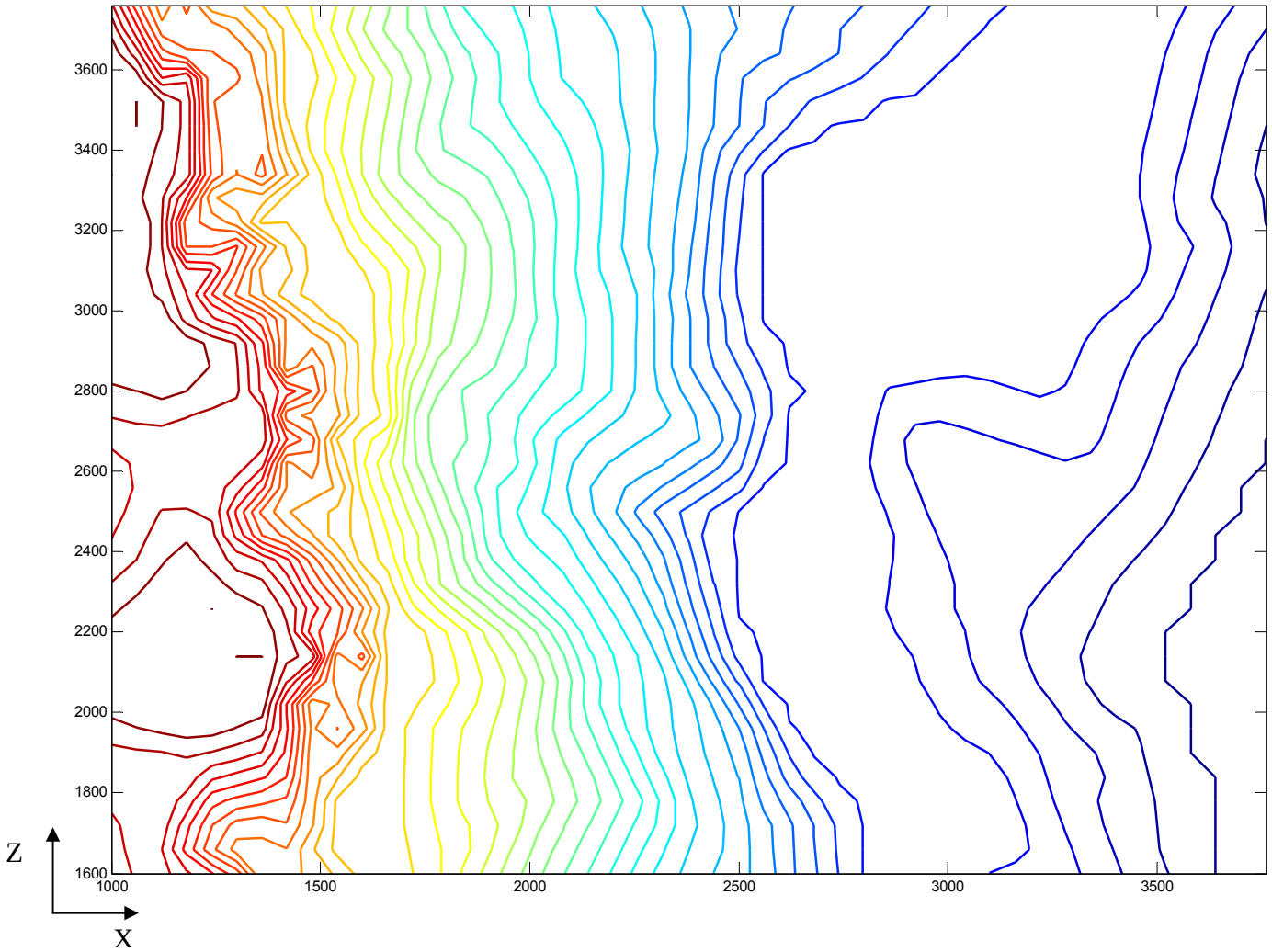

Fig. 4.3 - Elevation contours prior to the February 17th, 2006 slide. Elevation points used to produce these contours were also used to create the 3DEC elevation model.

4.2 - 3DEC MODEL GENERATION

Once the surface elevation model was generated in Matlab 7.0 based on the digitized topographic map, a digital elevation model was created in 3DEC. The digital elevation model was created on a 100 m by 100 m grid in 3DEC and consists of rectangular blocks of different heights glued together, forming a three-dimensional model of the area around Guinsaugon village and the scarp. As previously mentioned, the model covers an area of 2.8 km in the North-South direction by 2.2 km in the East-West direction as shown in Fig. 4.4. Some details of the topography have not been depicted as accurately as desired due to the large 100 m by 100 m grid used. However, the use of a smaller grid would greatly increase the computation time and thus would require more computational resources that were not available at this time.

Once the digital elevation model was established in 3DEC, the next step involved the introduction of the discontinuities representing the failure surfaces forming the scarp (Fig. 4.5). The main failure surfaces were identified during the site survey by the U.S. Reconnaissance Team, as previously mentioned, and are graphically portrayed in Fig. 4.6. The identified failure surfaces are:

a. Main Fault (part of the PFZ)
b. Vertical shear failure surface on the north side of the scarp
c. Side fault on the southwest side of the scarp
d. Sliding surface forming the left side of the valley created
e. Sliding surface forming the right side of the valley created

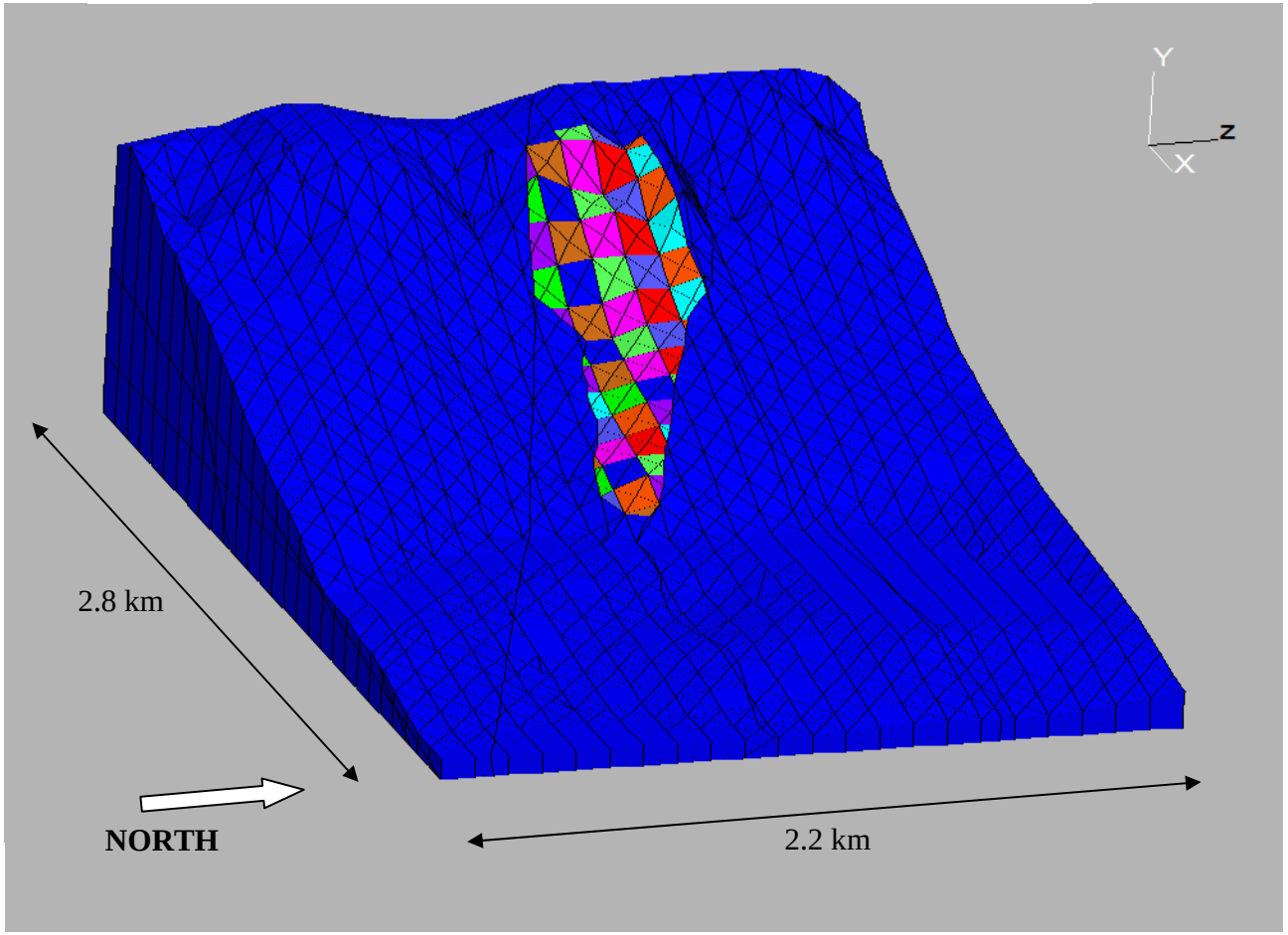

Fig. 4.4 - Digital Elevation Model of the slide area in 3DEC on a 100 m by 100 m grid.

The three first mentioned failure surfaces, i.e. the main fault, the vertical shear failure surface, and the side fault, were exposed on the surface and their location could be easily identified on the post-slide topographic map. Using the post-slide contour map and performing the digitization process mentioned in a previous section, which was also used to create the digital elevation model, the location of the exposed section of the three mentioned failure surfaces was identified and added to the 3DEC model.

Once the three steep failure surfaces were identified, the challenge was to identify the location of the two shallow dipping failure surfaces forming the valley at the foot of the scarp. Since these two surfaces were relatively shallow, their exact location could not be easily identified by visual inspection of the surface contour map. Therefore, an initial model of the scarp was created by estimating their location and orientation to the best of knowledge.

The U.S. Reconnaissance Team measured the orientation, i.e. dip and dip direction, of the main fault, the vertical shear failure surface, and the side fault during the site survey. Measurements of the rock surfaces were done following conventional in-situ measurement methods by use of compass and inclinometer. Additionally, a LIDAR (LIght Detection And Ranging) surveys was performed during the site visit. LIDAR is an optical remote sensing technology that uses laser pulses to measure distance, speed, rotation and other properties of a remote target. The two sets of data were later compared to ensure maximum possible accuracy. Unfortunately, the exact orientation of the two valley surfaces could not be accurately identified. The general dip direction of the surface was measured during the site survey, but the dip of the surfaces was not measured since the entire valley was covered by debris material. Thus, since the exact location of the bottom of the valley could not be identified during the site survey, the first 3DEC model included only an estimate of the orientation of the two valley surfaces.

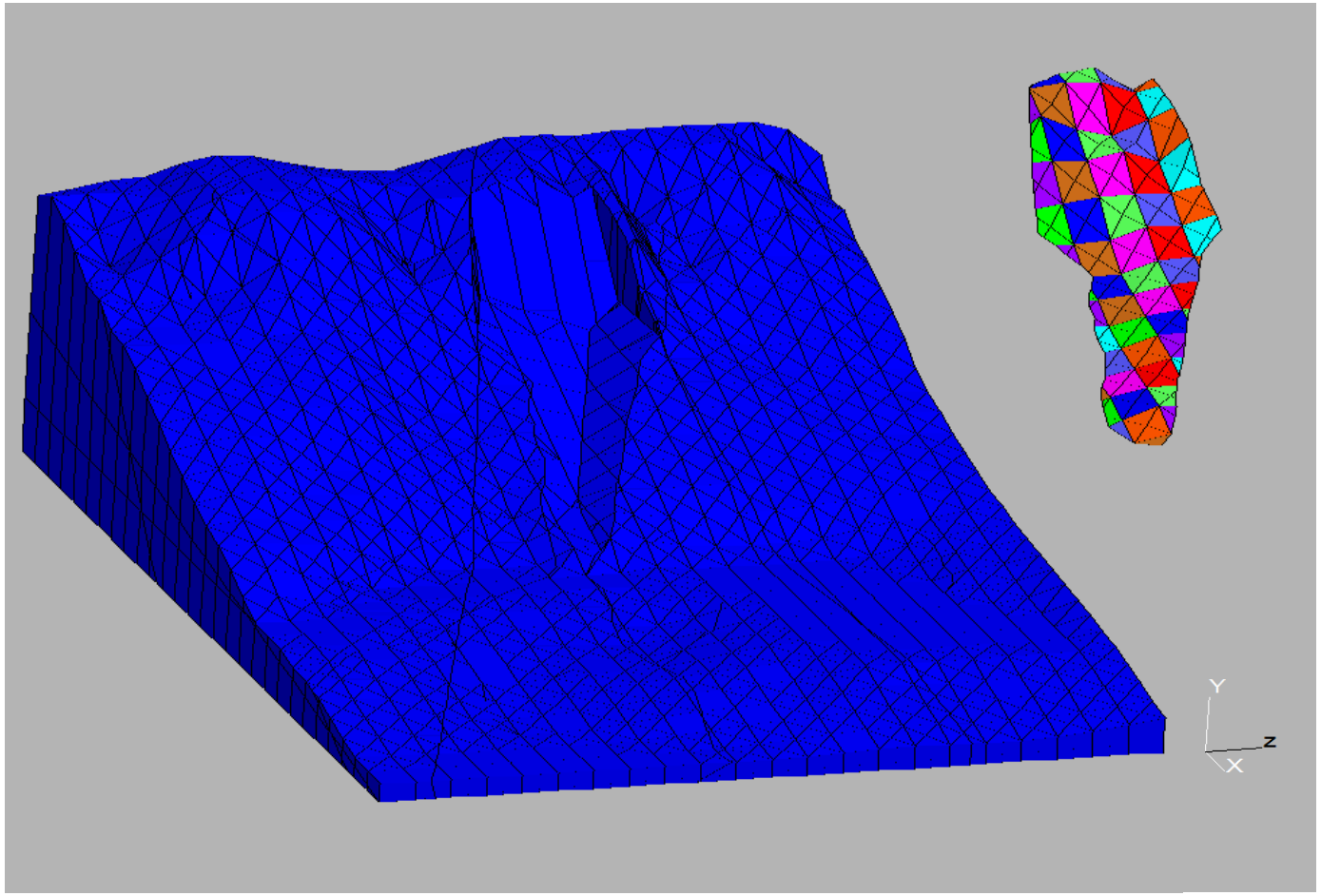

Fig. 4.5 - Digital Elevation Model in 3DEC showing detached block and exposed failure surface.

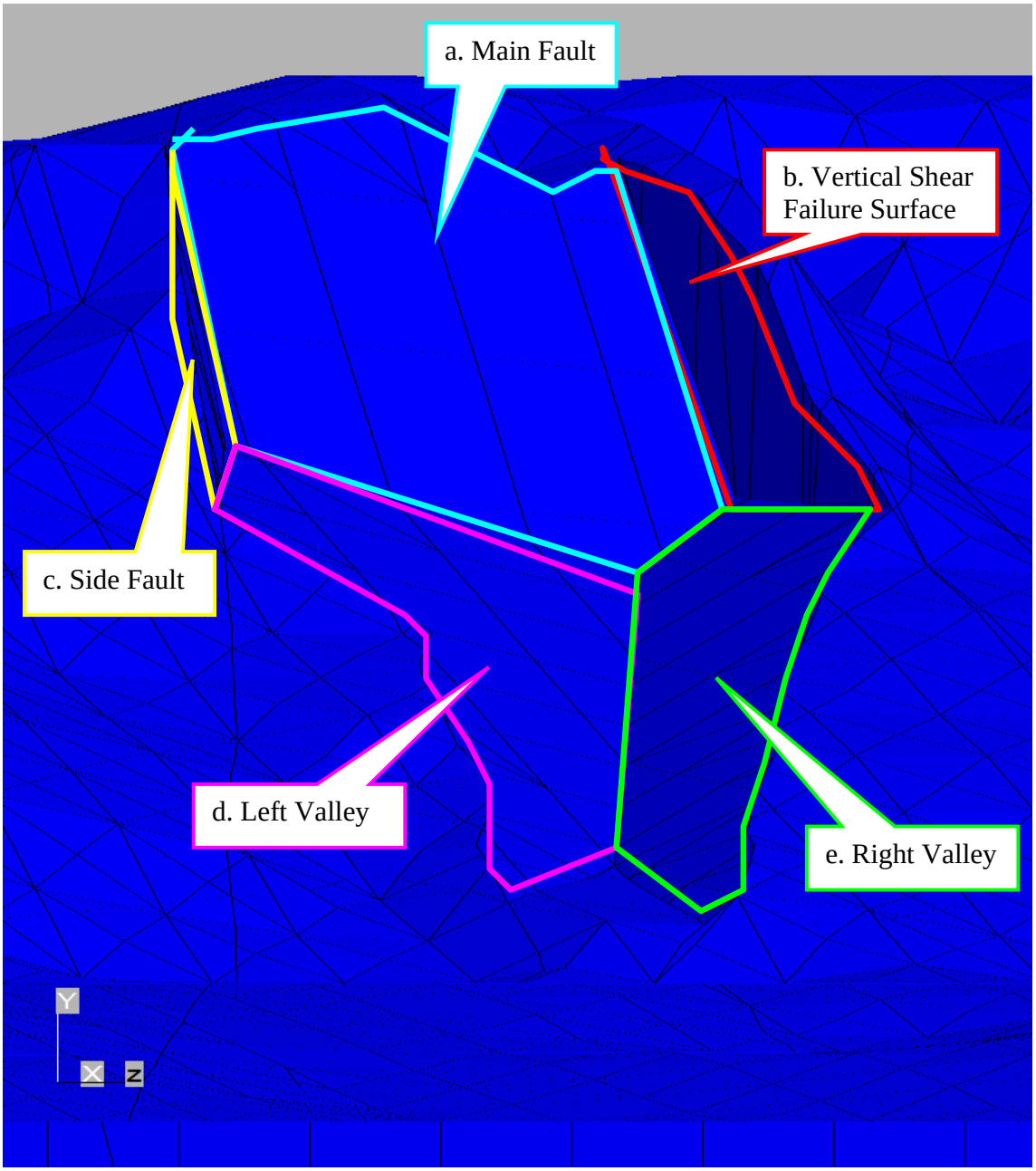

Fig. 4.6 - Scarp and five identified failure surfaces.

Ensuring the accuracy of the geometry of the model and the scarp is the most important step prior to performing the distinct element analysis. Taking into account that the only available topographic map representing the area contours prior to the slide, from which the digital elevation model was created, had limited accuracy, it is reasonable to assume that the final model would not be highly accurate. The large grid used in the 3DEC model, due to computational limitations, also controls the overall accuracy. However, the accuracy of the model as a whole can be improved by achieving a correct representation of the scarp and its dimensions.

Fortunately, more accurate and high-resolution satellite topographic maps of the Guinsaugon area became available after the slide, depicting the contours near and at the scarp (Fig. 4.7). Actual and digitized copies of these maps served as the main tool in ensuring the accuracy of the scarp generated in the 3DEC model (Figs. 4.7 and 4.8). As previously mentioned, the location and orientation of some of the failure surfaces was initially estimated and thus the resulting scarp had to be verified by comparing the resulting contours to the existing and available contour maps of the area. This procedure was critical especially in identifying the depth of the scarp and the point of intersection of the failure surfaces.

The trial-and-error method was used in achieving the final 3DEC model. After the location or orientation of one of the failure surfaces was changed, the resulting model was compared to a scaled copy of the topographic map of the area that included an outline of the extent of the slide (Fig. 4.7). After achieving a relatively accurate match of the outline of the exposed surfaces in the model to the outline on the topographic map, the next step was to match the contours of the 3DEC model, when the block is removed (Fig. 4.8), with the contours of the post-slide topographic map by trial and error.

The procedure of matching the post-slide contours of the model to the high-resolution topographic map includes several steps. First, the sliding block in the 3DEC model was ‘deleted’ and the grid points of the now exposed surfaces were logged, using the necessary 3DEC command. Then, the logged surface points were used in Matlab 7.0 to create a surface and contour plot, similar to the one created initially for the pre-slide model (Figs 4.10a, 4.10b, and 4.11). The contour plot generated through Matlab was then plotted to the required scale and compared to both the actual and digitized

copies of the topographic map of the area. In fact, the actual copy of the contour map proved to be more useful since it did not include the additional inaccuracy that the digitized copy included. Thus, the actual contour map was printed on a transparency, to the correct scale, and visually compared to the Matlab contour plot of the 3DEC model with the sliding block removed.

In addition to the contour comparison of the post-slide topographic map to the Matlab generated contours of the 3DEC block-removed model, the 3DEC model was also visually compared to an actual picture of the scarp taken during the reconnaissance team's visit to the site (Fig. 4.12). Although this is not considered an accurate comparison and cannot be reliable on its own, it still believed as an important step in achieving a model that is as close to real as possible. Appendix A includes several photographs of the scarp and debris material, obtained by the U.S. Reconnaissance Team during their site visit.

After several trials, the position of each of the failure surfaces as well as their orientation was finalized. The contours obtained from the 3DEC model with the removed block matched perfectly with the contours on the post-slide topographic map. Figs. 4.7 and 4.11 present the actual elevation contours of the area and the Matlab generated contours of the final 3DEC model respectively. Further analysis can now be performed on the finalized 3DEC model (Fig. 4.13 through 4.15d). The dip and dip direction of each of the introduced failure surfaces are as follows:

- Main Fault: Dip = 48^o Dip Direction = 85^o
- Vertical Shear Failure Surface: Dip = 88^o Dip Direction = 175^o
- Side Fault: Dip = 75^o Dip Direction = 25^o
- Left Valley: Dip = 25^o Dip Direction = 57^o
- Right Valley: Dip = 29^o Dip Direction = 172^o

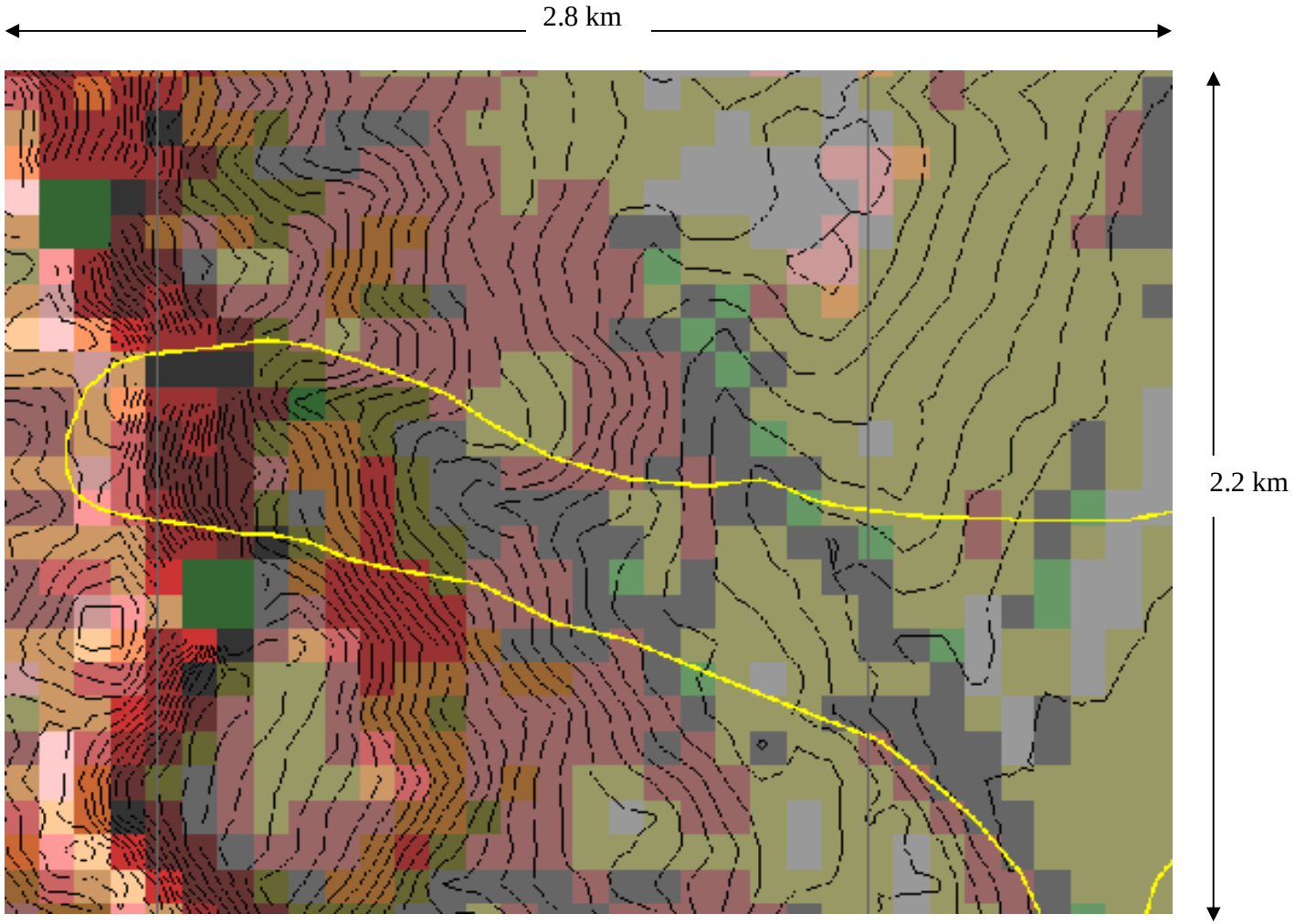

Fig. 4.7 - Post-Slide topographic map of the area including surveyed outline of the extent of the Guinsaugon slide.

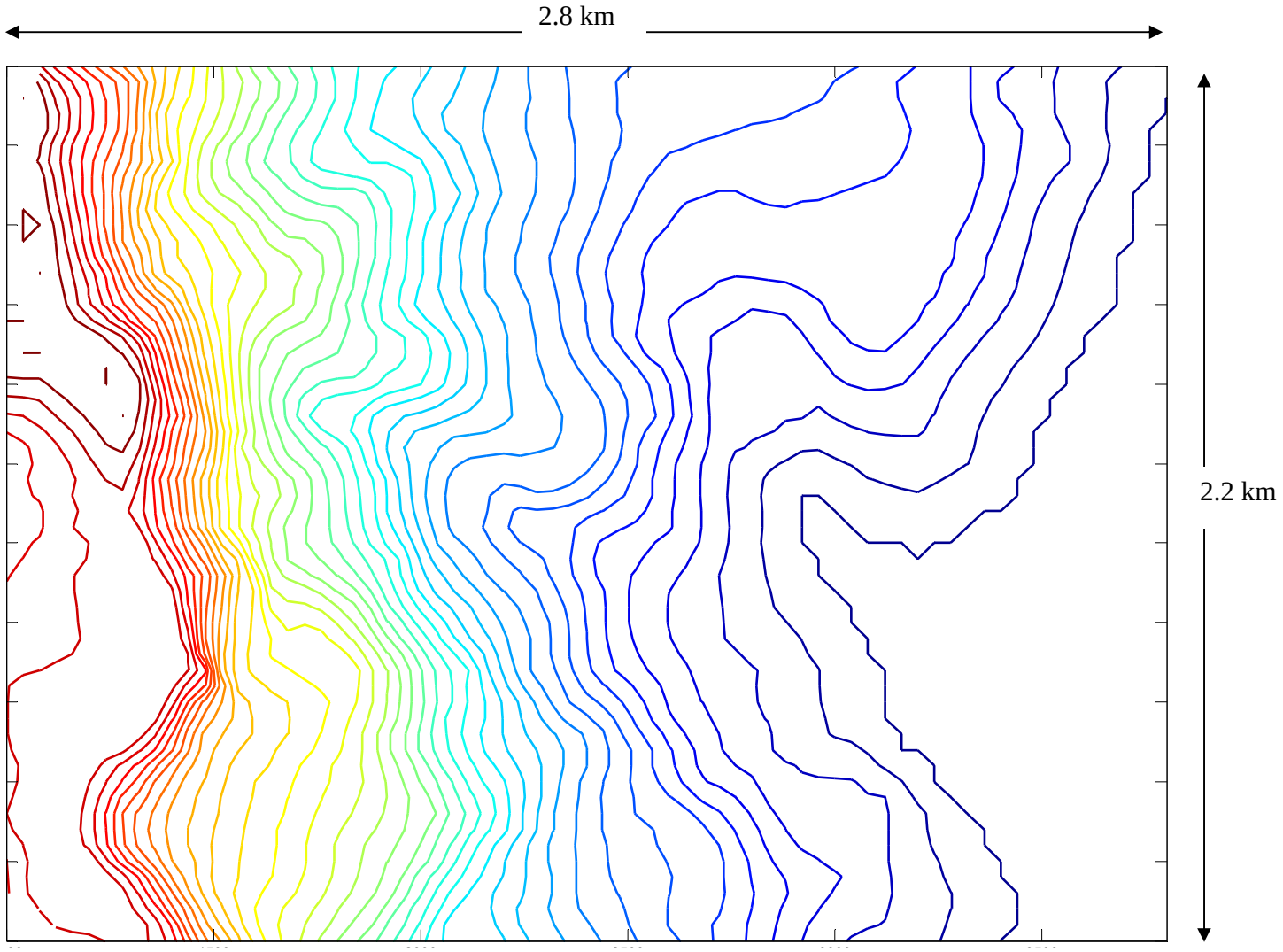

Fig. 4.8 - Matlab generated contours based on digitization of the original contour map of the area. This digitized version of the topographic map is considered less accurate due to additional human error from digitization process.

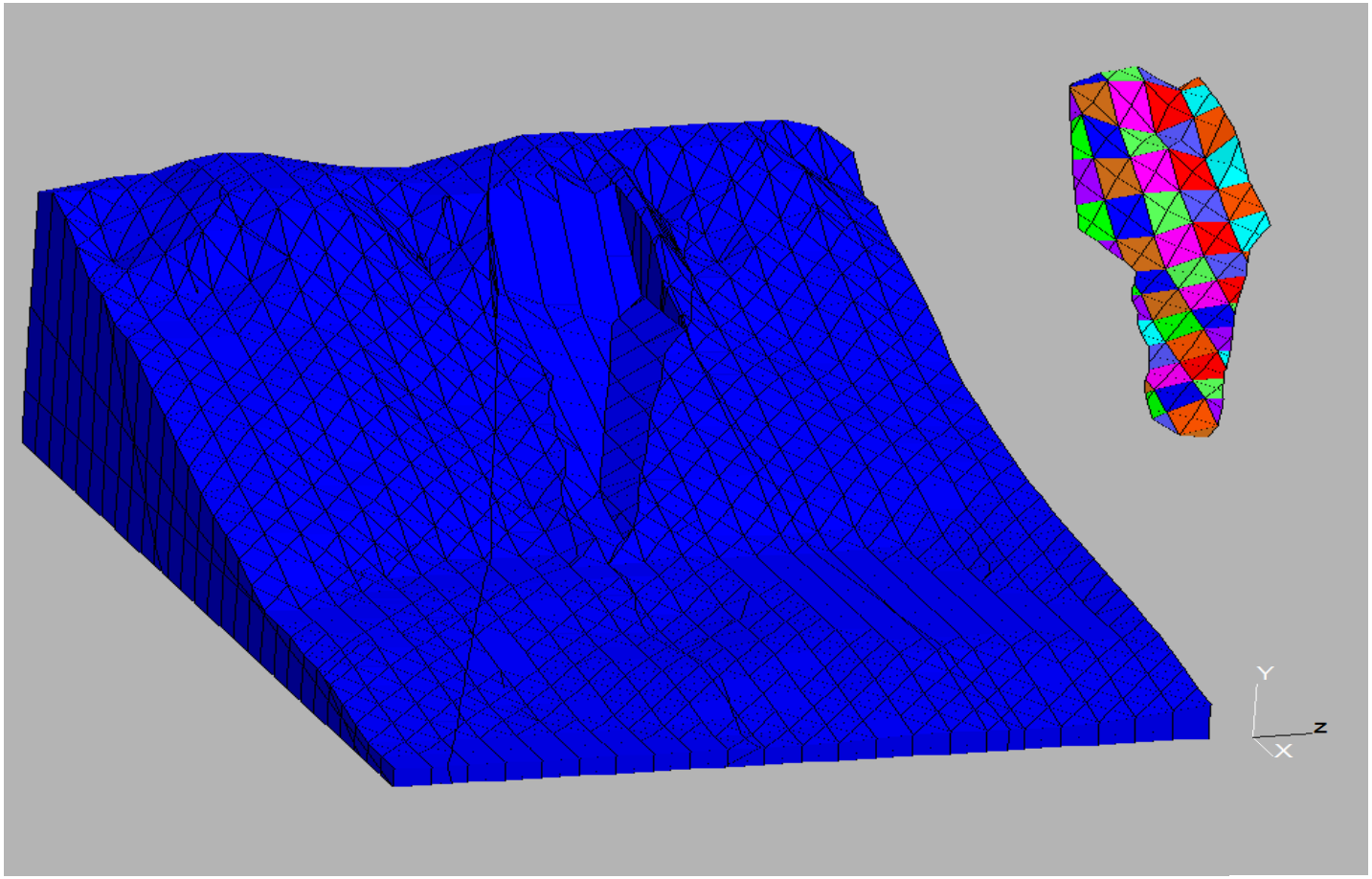

Fig. 4.9 - Final 3DEC model trial. Scarp and removed block are shown.

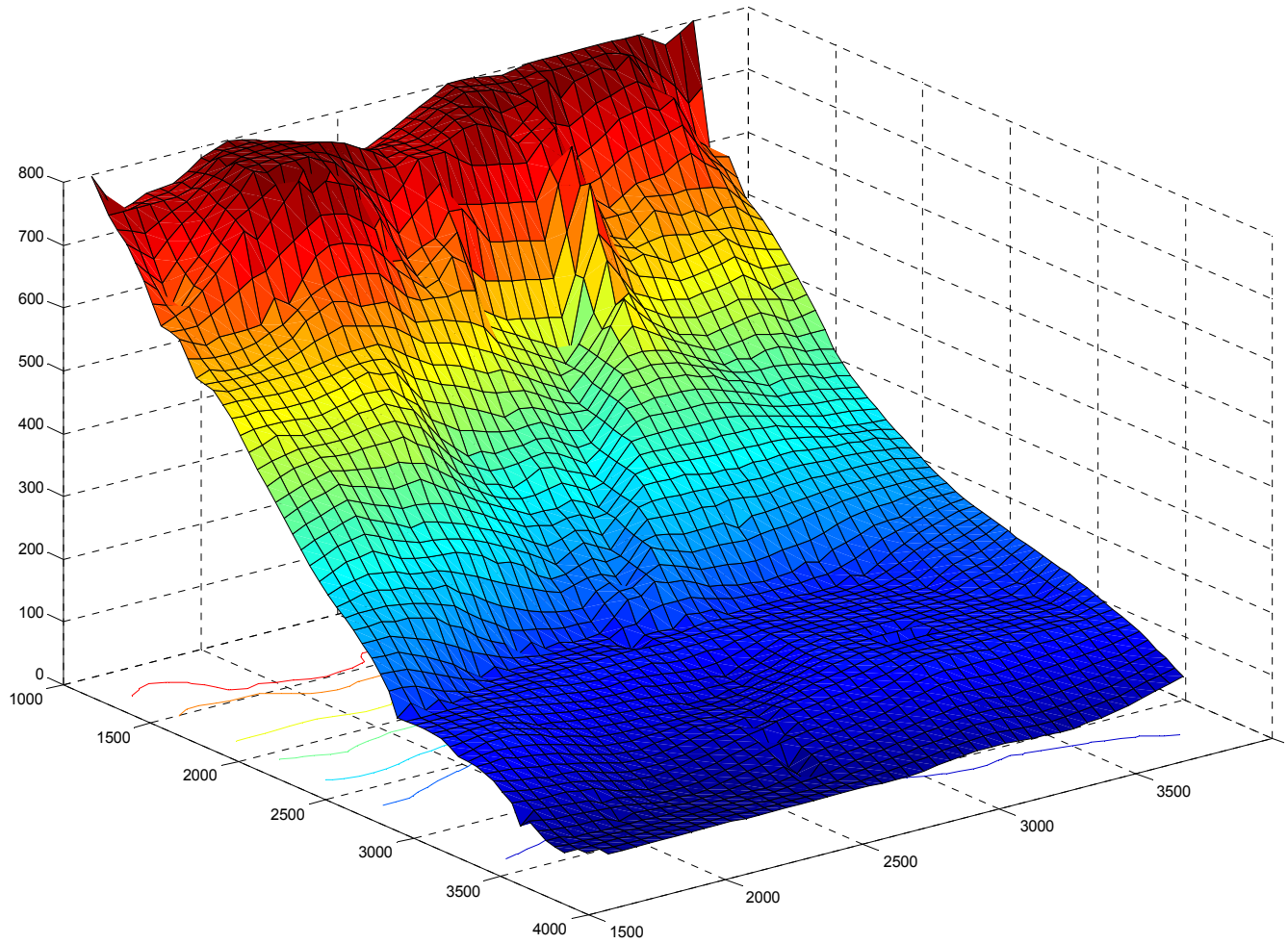

Fig. 4.10a - Matlab post-slide surface plot of the final 3DEC model, underlain by contours, to be compared to the actual post-slide contours on the topographic map.

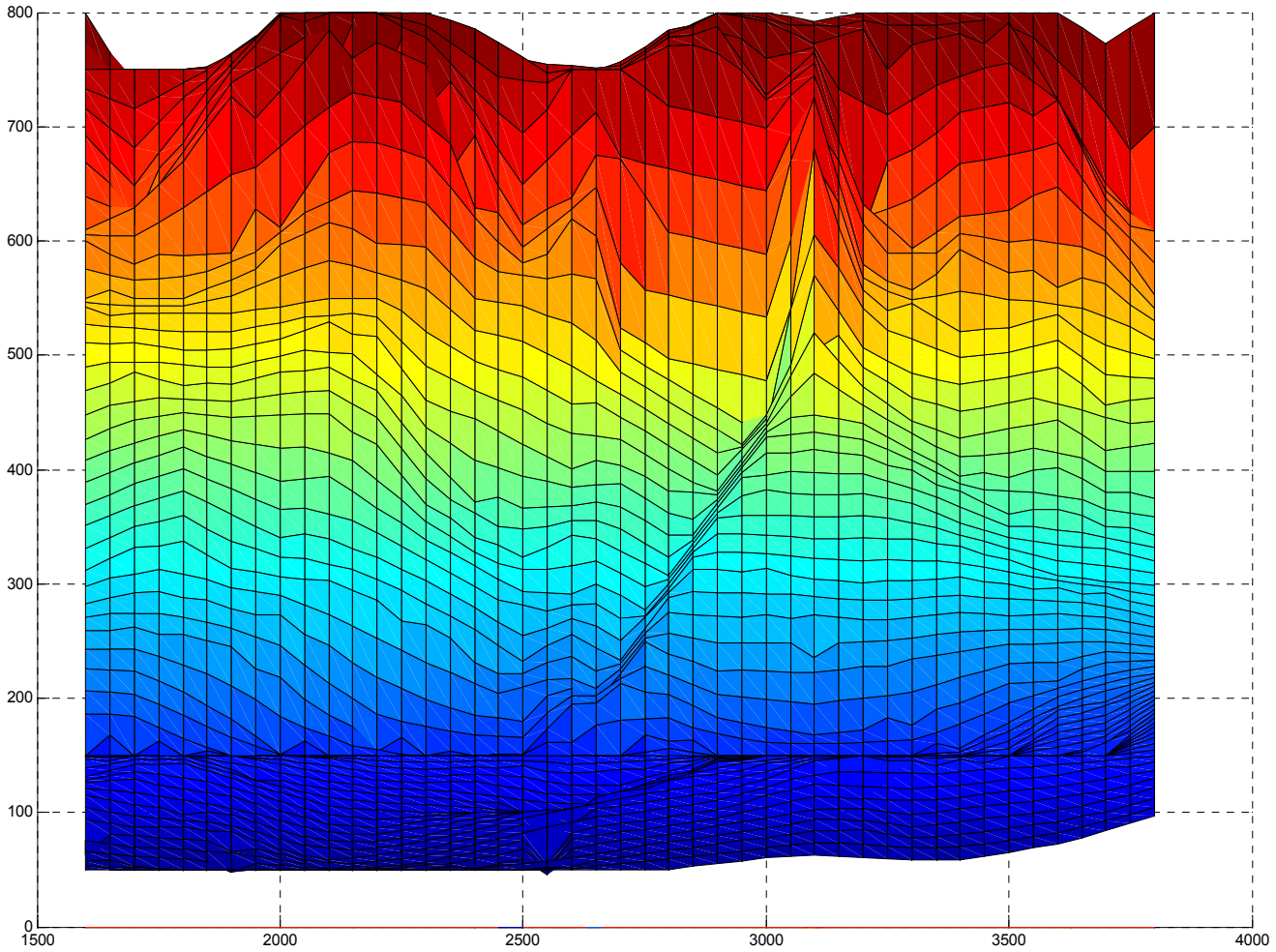

Fig. 4.10b - Matlab post –slide surface plot of the final 3DEC model. View from East to West.

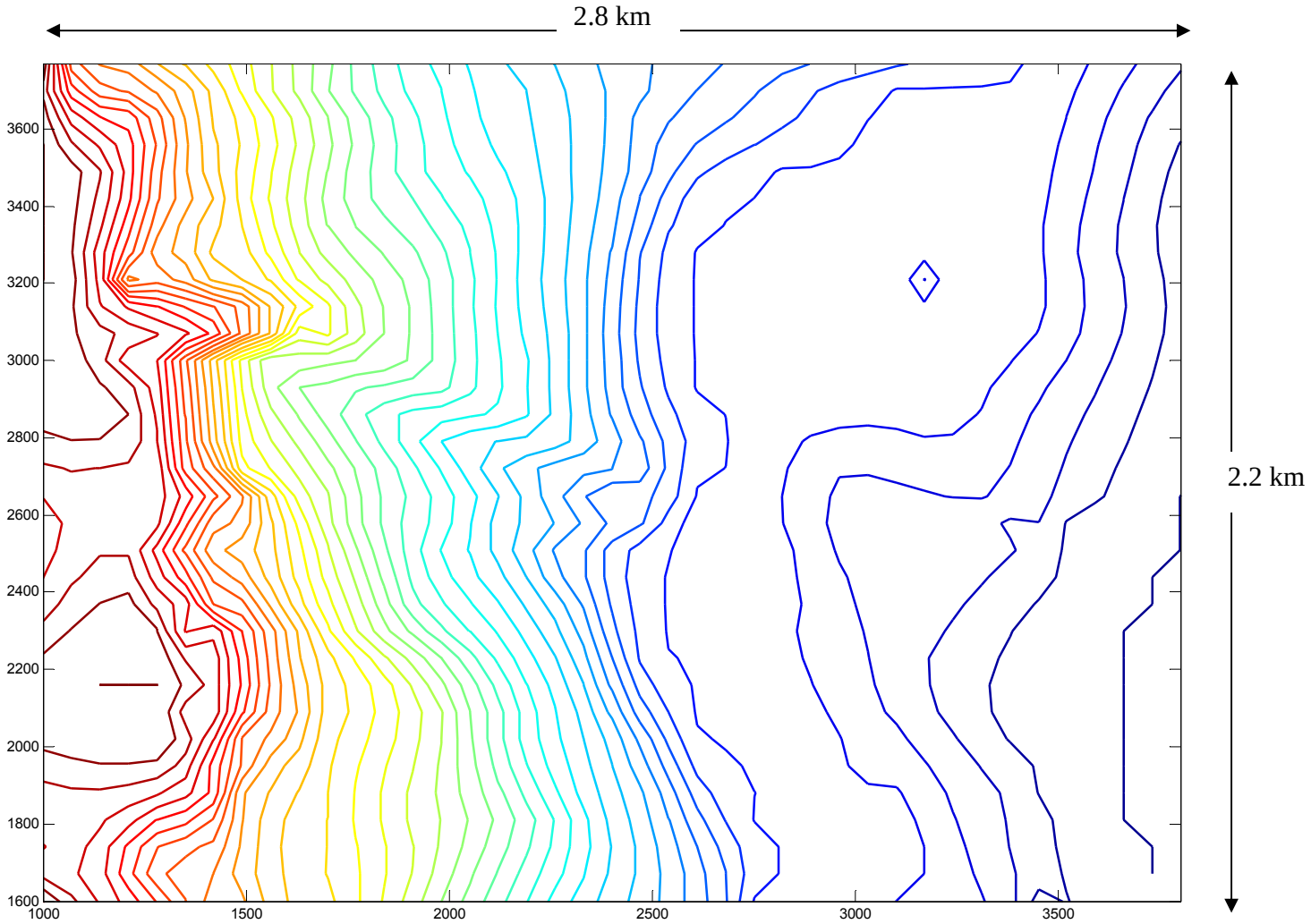

Fig. 4.11 - Matlab post-slide contour plot based on the final 3DEC model. These contours are to be compared to the actual post-slide contours on the topographic map of the area.

Fig. 4.12 - North-west view of the scarp (Gutierrez, 2006)

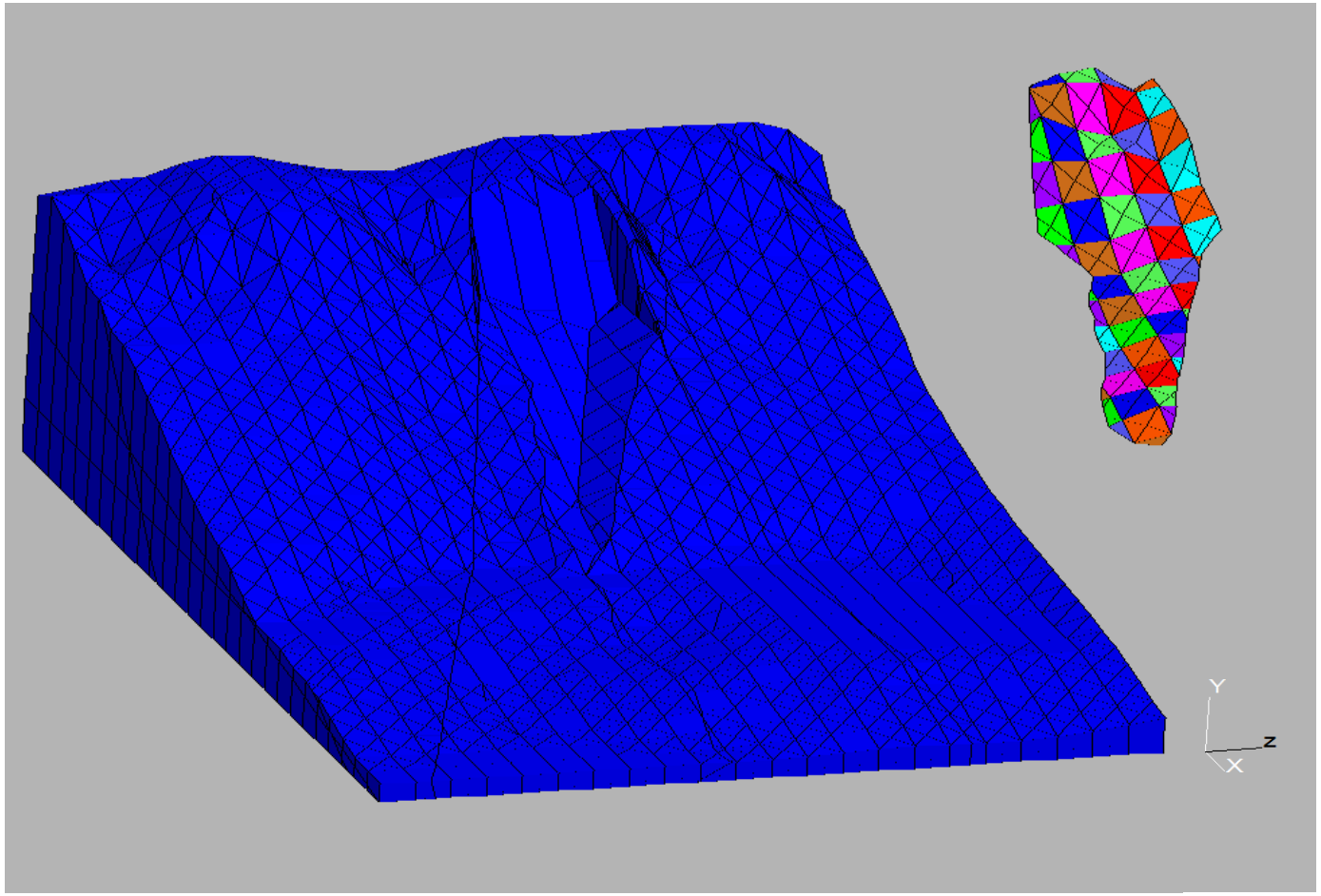

Figure 4.13 - Final selected 3DEC model to be used in numerical analysis, after careful comparison of the two sets of contours.

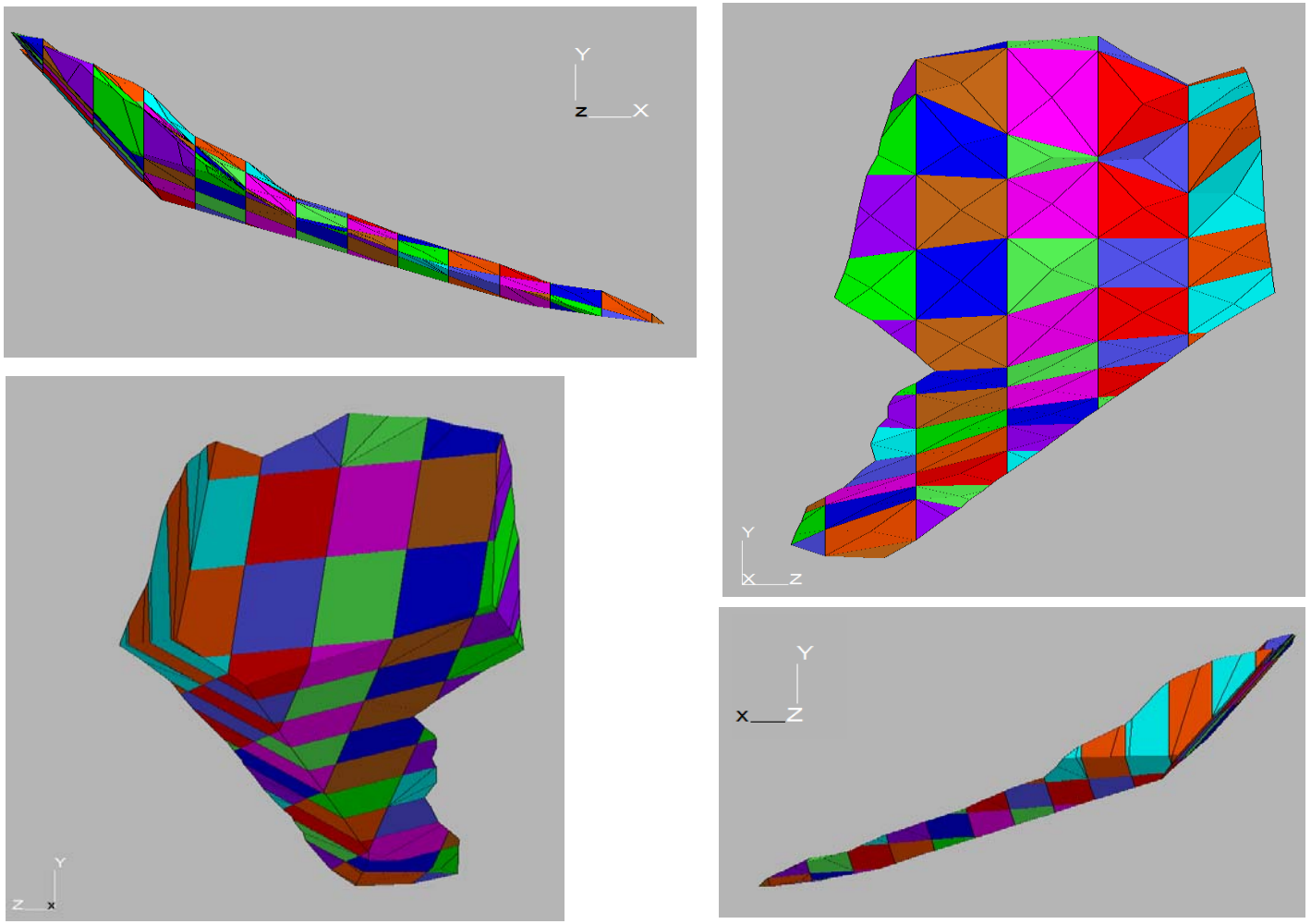

Fig. 4.14 - Various views of the overhanging rock mass modeled as a rigid and intact block

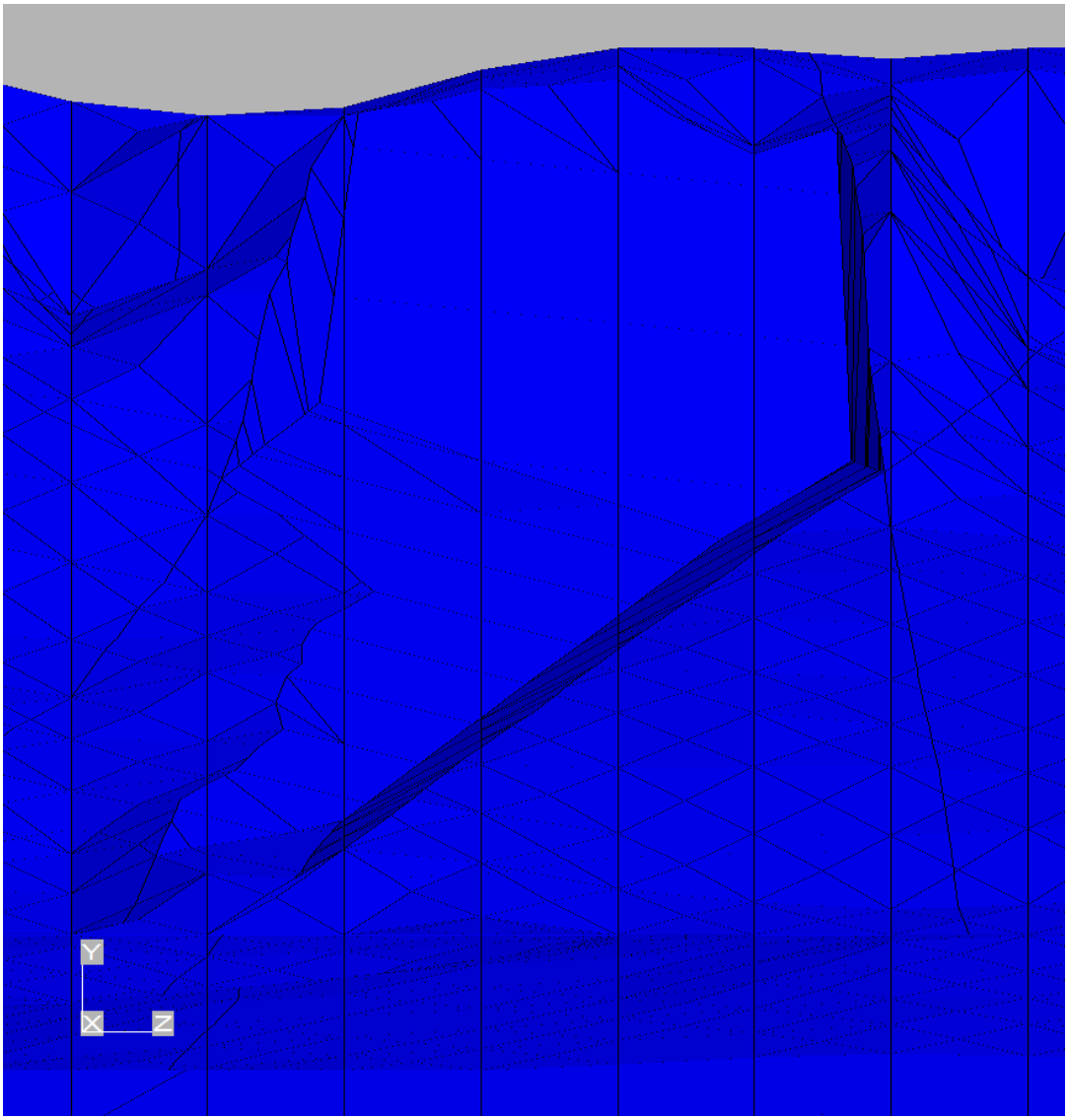

Fig. 4.15a - Scarp created by removal of the sliding block, showing all five failure surfaces involved.

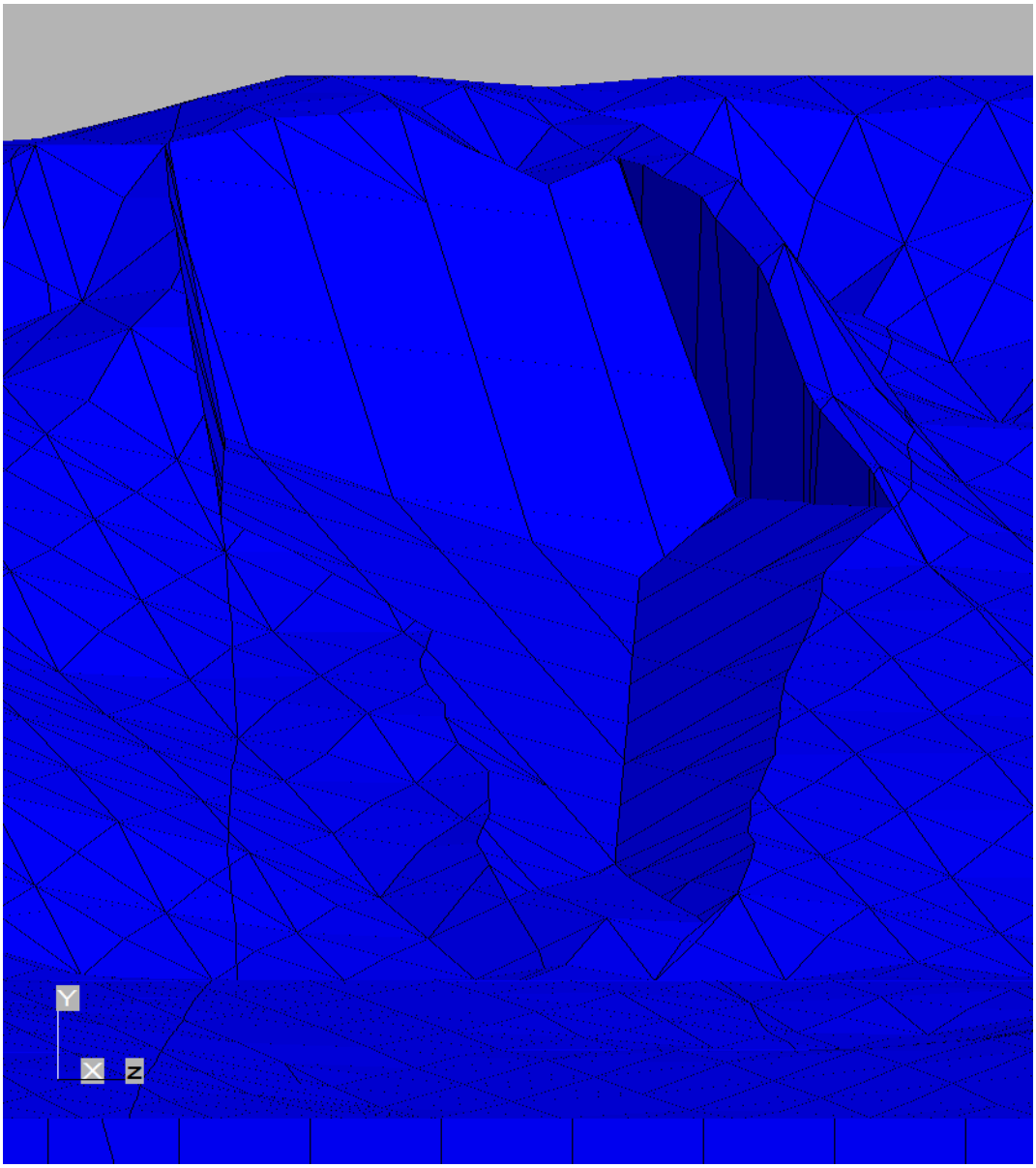

Figure 4.15b - Scarp created by removal of the sliding block, showing all five failure surfaces involved.

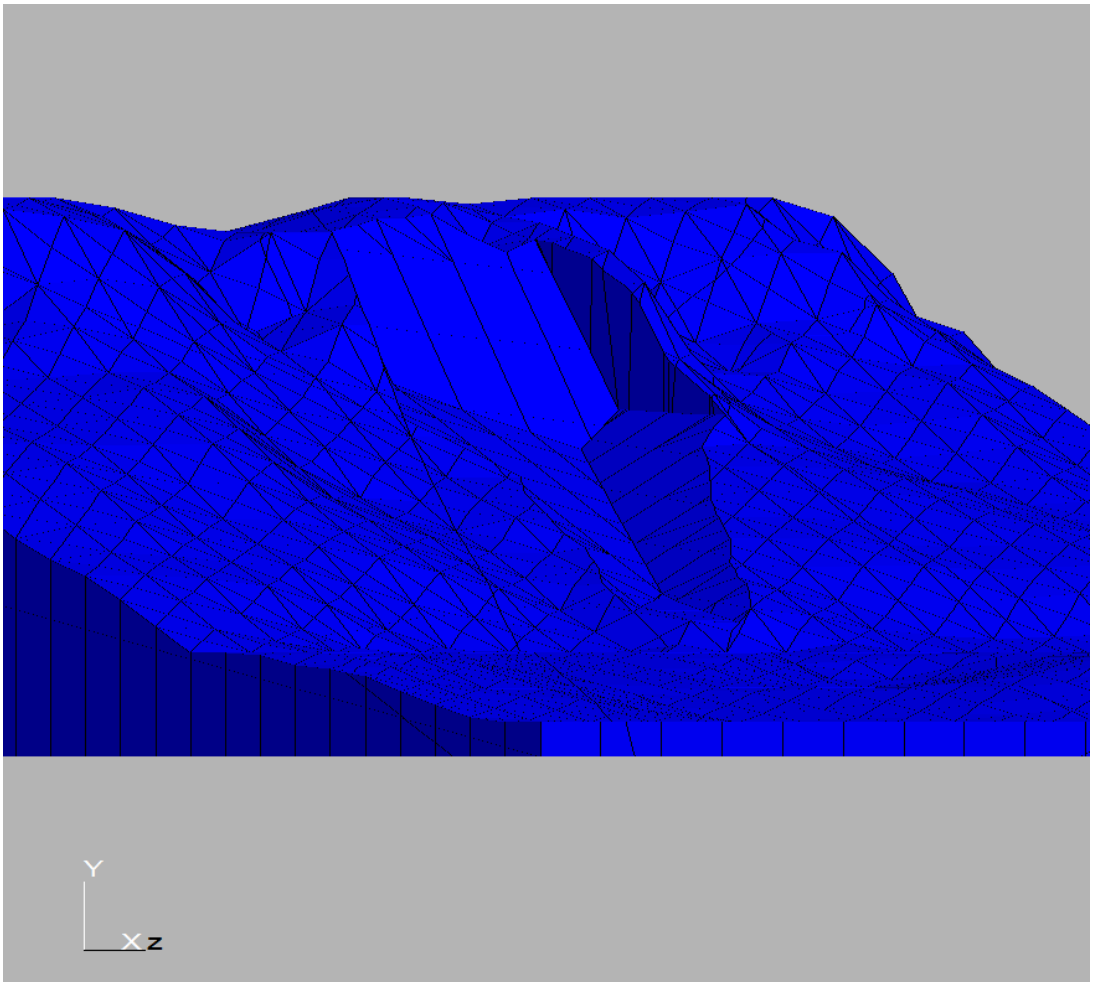

Figure 4.15c - Scarp created by removal of the sliding block, showing all five failure surfaces involved.

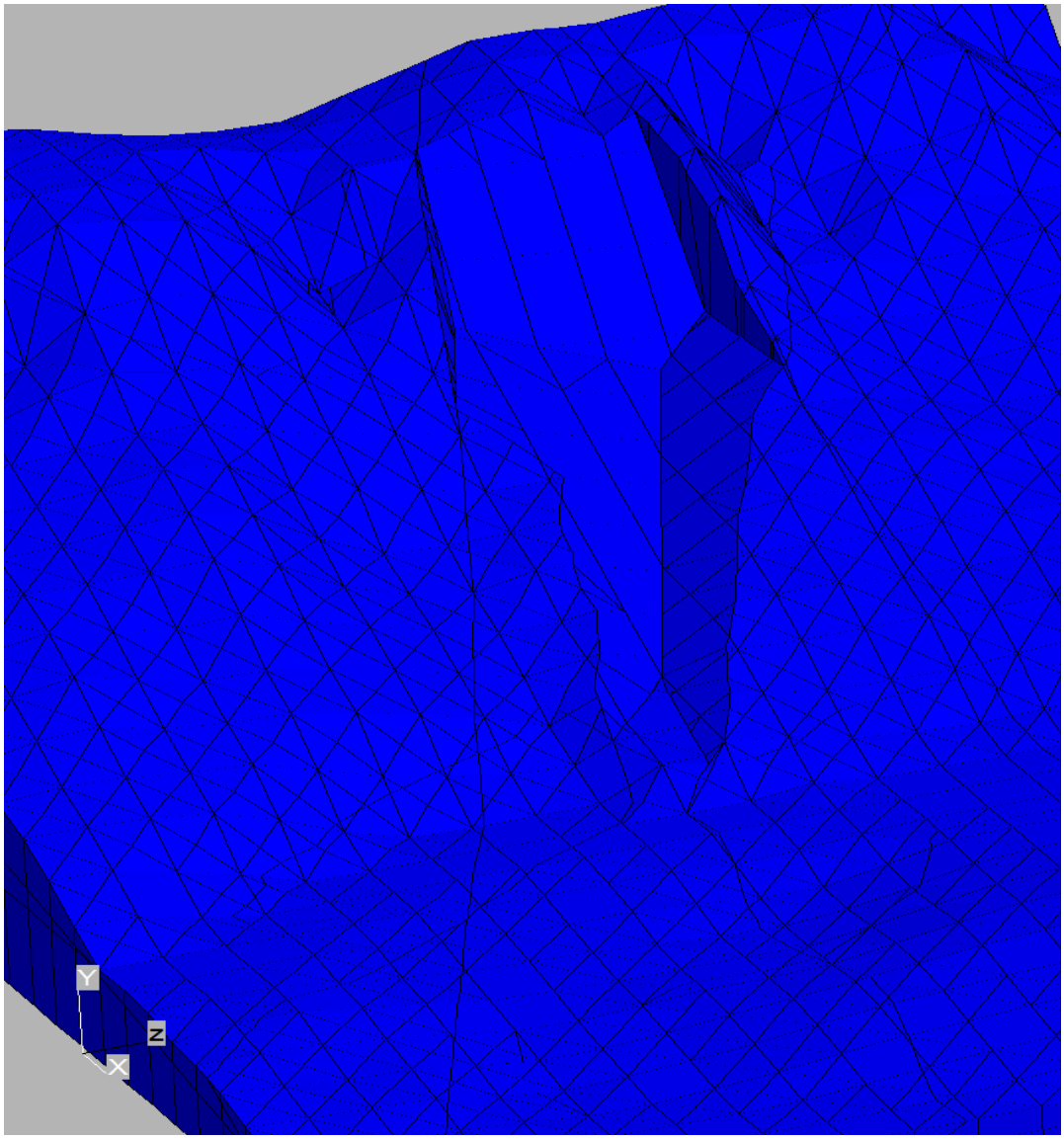

Figure 4.15d - Scarp created by removal of the sliding block, showing all five failure surfaces involved.

CHAPTER 5: STRENGTH PROPERTIES OF THE SLIDE SURFACES

5.1 - GENERAL

In order to proceed with the numerical analysis of the slide, material properties need to be assigned to the materials and failure surfaces forming the scarp. The main failure surfaces that were identified during the site survey by the U.S. Reconnaissance Team are graphically portrayed in Figure 5.1. The identified failure surfaces are:

a. Main Fault (part of the PFZ)
b. Vertical shear failure surface on the north side of the scarp
c. Side fault on the southwest side of the scarp
d. Sliding surface forming the left side of the valley created
e. Sliding surface forming the right side of the valley created

The failure surfaces were given normal and shear stiffness, and shear strength properties such as friction angle, cohesion, tensile strength and dilation angle. The joint properties used in the analysis were obtained from a combination of in-situ tests, laboratory tests, as well as published empirical correlations. In-situ testing was performed during the U.S. reconnaissance team's visit to the rockslide site on November 2006. Rock and soil samples were also obtained in the field and transferred to the Virginia Tech Geotechnical Engineering laboratories in Blacksburg, Virginia, for additional testing.

In-situ tests included fracture surface roughness profilometry and Schmidt hammer tests performed on exposed failure surfaces in the field. Laboratory tests were performed on rock and soil samples obtained from the field to gain a better understanding of the properties of the materials involved in the slide (Farmer, 2006). Laboratory tests performed on rock samples included unconfined compressive strength of intact rock core specimens, splitting tensile strength of intact rock core specimens (Brazilian tests), point load strength index of rock, and porosity tests. Laboratory tests performed on soil samples included sieve and hydrometer analysis, specific gravity of soils, and Atterberg limits. The selected modeling parameters for each of the failure surfaces are described in detail in the following sections.

The intact blocks used in the distinct element analysis were modeled as rigid blocks and the only parameter required is the unit weight of block materials. The dry unit weight of the materials involved in the slide was obtained from laboratory tests and was found to be approximately equal to 19.6 kN/m^3. Specific gravity and porosity were also obtained from laboratory tests, which resulted in G_s=2.64 and n=23.8%. The individual blocks forming the overhanging rock, i.e. the sliding block, were considered wet and thus an estimated moist unit weight of 20.5 kN/m^3 was used, corresponding to a water content w of about 5%. This is an estimated amount water infiltration into the rock following 21 days or about 75 cm of rainfall before the slide occurred. Witnesses of the slide mentioned seeing a dust cloud right after the failure, which indicates that the rocks in the area were not fully saturated at the time of the slide.

5.2 - MAIN FAULT

In the numerical analysis of the 3DEC model of the Guinsaugon slide, the Barton-Bandis model was used to represent the joint behavior. The shear strength properties of the main fault failure surface were determined by the Barton-Bandis failure criterion written in a non-linear form of the Mohr-Coulomb failure criterion.

According to the Barton-Bandis model (Barton and Bandis, 1983), the shear strength of the fault is governed by the equation:

$$\tau = \sigma'_n \tan\left[JRC_n \log\left(\frac{JCS_n}{\sigma'_n} \right) + \phi_r \right] \qquad \text{Equation 5.1}$$

where,

τ = shear stress along the fracture

JRC_n = joint roughness coefficient for the actual fault length

JCS_n = joint compressive strength for the actual fault length

σ'_n = effective normal stress across the fault

ϕ_r = residual friction angle

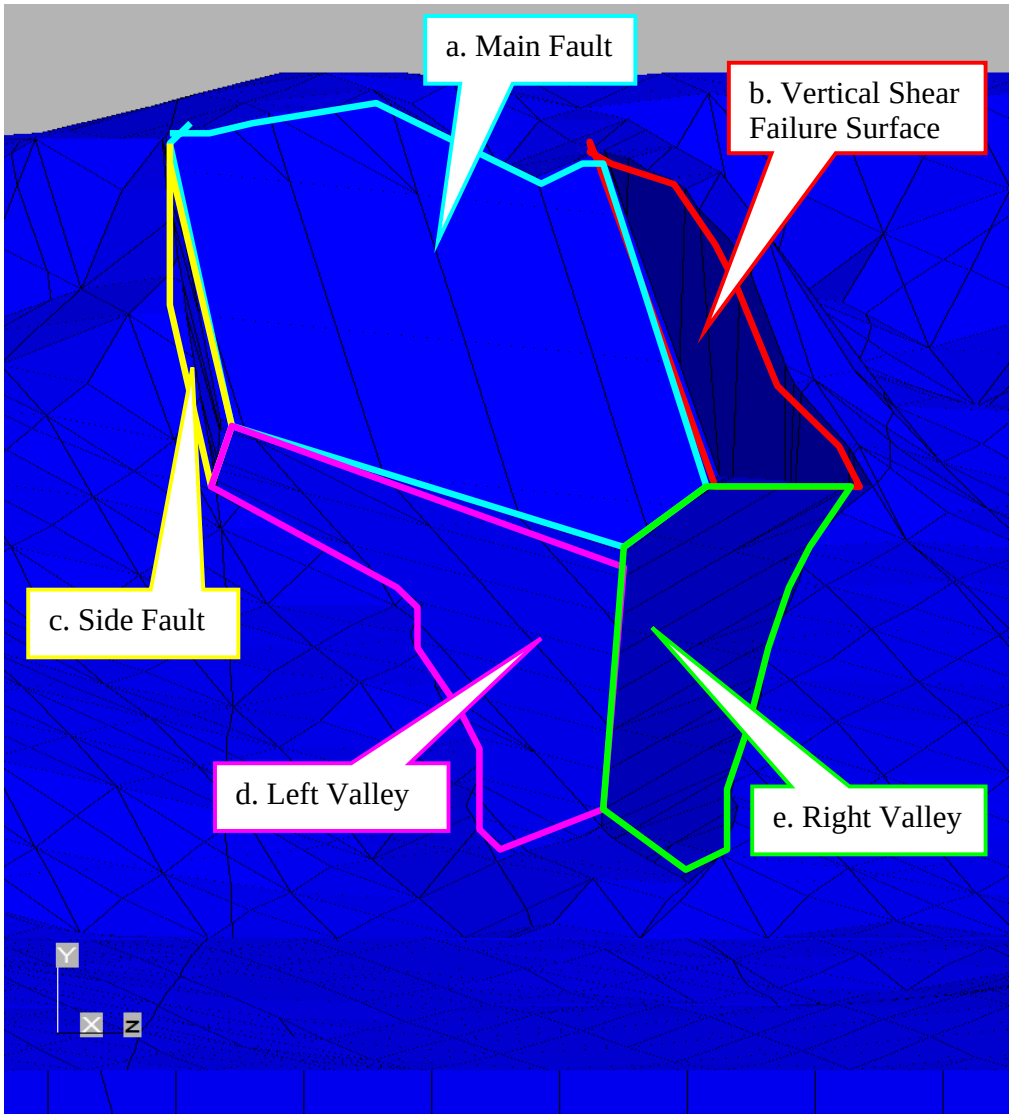

Fig. 5.1 - Scarp and five identified failure surfaces.

The material properties required in the Barton-Bandis model are:

- L_n, L_o = Fracture length (in m)
- E_o = Initial fracture aperture (in m),
- JRC_n, JRC_o = Joint Roughness Coefficient
- JCS_n, JCS_o = Joint Compressive Strength (in MPa)
- ϕ_r = Fracture residual friction angle (in ^{o})

The subscripts *o* and *n* refer to the laboratory or sampling length of the fracture (typically 0.1m) and the in-situ fracture length, respectively.

The Joint Compressive Strength (JCS) was determined using data from the previously mentioned Schmidt hammer tests performed on the exposed failure surface in the field. The Schmidt hammer reading, *r*, and the unit weight, *γ*, are used in determining JCS_o, the joint compressive strength of the laboratory sample, according to Equation 5.2 as shown below:

$$\log(JCS_o) = 0.00088 * r * \gamma + 1.01 \qquad \text{Equation 5.2}$$

where
r = Schmidt hammer reading
γ = unit weight (in kN/m^3)

In case of the main fault, the following average values were obtained: *r* = 42 and γ = 16 kN/m^3. Hence, Equation 5.2 gives a value of JCS_o of 40 MPa.

The Joint Roughness Coefficient (JRC) was determined using fracture surface roughness profilometry data obtained in the field. An example of a 20 cm roughness profile obtained from the surface of the exposed main fault is shown in Figure 5.2. Figure 5.3 graphically describes the relationship between the amplitude of asperities in mm, the length of the profile in m, and the corresponding Joint Roughness Coefficient, JRC_o. This diagram was originally developed by Barton and Choubey (1977) to get a fast and rough estimate of the roughness of fracture surfaces. From this figure, an average value of JRC_o=16 is obtained.

Fig. 5.2 - Typical 20 cm fracture profile of the main the fault.

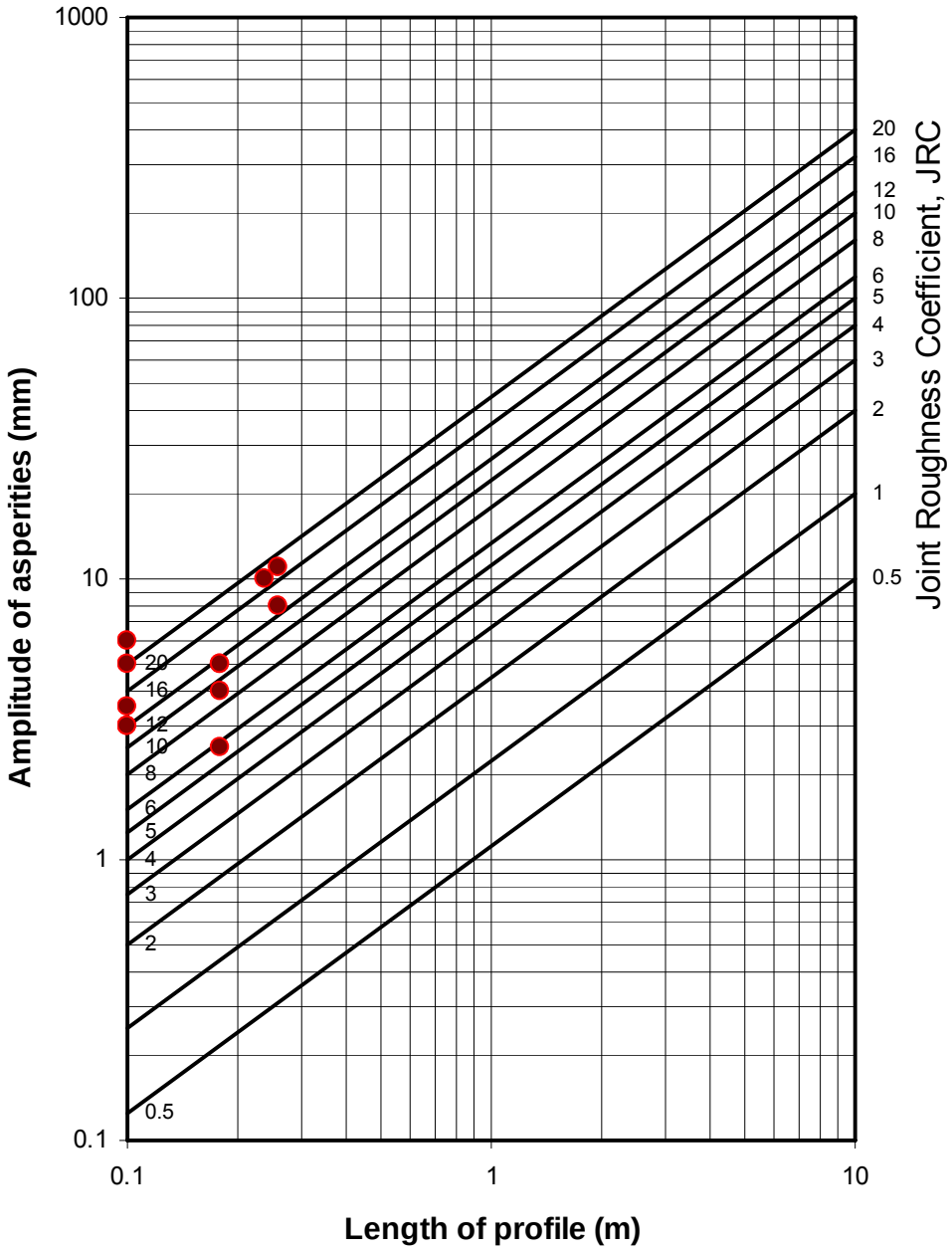

Fig. 5.3 - Determination of the Joint Roughness Coefficient (JRC_o) of the main the fault from profilometry (Barton and Choubey, 1977).

FRACTURE SCALING LAWS

The Joint Roughness Coefficient, JRCn, and the Joint Compressive Strength, JCSn, representative of the actual fault length, Ln, are determined by applying the Barton-Bandis Fracture Scaling Laws (Barton and Bandis, 1982). The scaling laws relate the joint roughness coefficient and the joint compressive strength corresponding to the actual in-situ fracture length to the fracture measured in the laboratory or the sampling scale in the field by the following equations:

$$\mathrm{JRC_n} = \mathrm{JRC_o}\left(\frac{L_n}{L_o}\right)^{-0.02 \cdot JRC_o} \qquad \text{Equation 5.3}$$

$$\mathrm{JCS_n} = \mathrm{JCS_o}\left(\frac{L_n}{L_o}\right)^{-0.03 \cdot JRC_o} \qquad \text{Equation 5.4}$$

For the main fault, L_o = 0.25 m, L_n = 300 m (estimated maximum length of the fault), JRC_o = 16 (from profilometry data), and JCS_o = 40 MPa (from Equation 5.2). Applying Equations (5.3) and (5.5) yields JRC_n=1.65 and JCS_n=1.3 MPa

The Barton-Bandis failure criterion in Equation 5.1 can also be expressed in the linearised form equivalent to the Mohr-Coulomb criterion as follows:

$$\tau = \sigma'_n \tan \phi_p \qquad \text{Equation 5.5}$$

where ϕ_p = equivalent peak friction angle, which can be expressed as follows:

$$\phi_p = \mathrm{JRC_n} \log\left(\frac{\mathrm{JCS_n}}{\sigma'_n}\right) + \phi_r \qquad \text{Equation 5.6}$$

The peak friction angle, ϕ_p, can never be smaller than the residual friction angle, ϕ_r, and thus in the case of $JCS_n < \sigma'_n$ the peak friction angle will be considered equal to the residual friction angle, ϕ_r.

As can be seen from Equation (5.6), the peak friction angle ϕ_p is dependent on the effective normal stress across the fault. Thus, to calculate the peak friction angle of the failure surface, which is a required input value in the Mohr-Coulomb model in 3DEC, a representative effective normal stress must be selected for the surface. The effective normal stress is calculated from the total stress and the fault pressure according to Terzaghi's effective stress law:

$$\sigma'_n = \sigma_n - u \qquad \text{Equation 5.7}$$

where,

σ'_n = effective normal stress at the centroid of the exposed surface

σ_n = total normal stress at the centroid of the exposed surface

u = pore pressure at the centroid of the exposed surface

The representative effective normal stress on the exposed surface selected is that applied at the centroid of the exposed surface. By simple calculations, the centroid of the exposed section of the fault was calculated to be approximately 170 m below the highest point of the exposed surface. Using a moist unit weight of 20.5 kN/m^3 for the overhanging rock material, the total vertical stress at the centroid, σ_n, is estimated to be about 3.5 MPa. Assuming that the fault is fully pressurized under hydrostatic condition, the fault pressure *u* is estimated to be about 1.67 MPa resulting in an effective fracture plane vertical stress σ'_n of about 1.9 MPa. Note that the value of 1.9 MPa corresponds to the vertical stress rather than the normal stress at the centroid of the exposed surface but the small difference in magnitude will have no effect on the result as proven later on.

The residual friction angle ϕ_r is also needed in determining the value for the peak friction angle ϕ_p of the main failure surface. The residual friction angle is related to the friction coefficient μ_r of the mineral comprising the surface of the fault:

$$\phi_r = \tan^{-1}(\mu_r)$$ Equation 5.8

where μ_r = friction coefficient. Published value by Lama and Vutukuri (1978) of the friction coefficient from common rock minerals were used in determining the residual friction angle. Lama and Vutukuri (1978) provide average values of friction coefficients μ_r for different rock minerals. From the reconnaissance survey, the main fault surface estimated was to have quartz as the fault in-fill material, and the fracture surface was mineralized with quartz. From Lama and Vutukuri (1978), the quartz-on-quartz average friction coefficient under moist conditions is μ_r = 0.455 giving $\phi_r = 25^\circ$.

Substituting the values of JRC_n=1.65, JCS_n=1.3 MPa, σ'_n =1.9 MPa, and $\phi_r = 25^\circ$ in Equation 5.6 gives a peak friction angle of $\phi_p = 25^\circ$ which is identical to the residual friction angle. This result indicates that the fault is at residual friction condition. Two reasons validate this result: 1) the large areal extent of the fault results in a lower frictional resistance following the Barton-Bandis fracture scaling laws, 2) the large effective normal stress in comparison to the scaled value of the Joint Compressive Strength means that the fault is not able to mobilize the roughness component $JRC_n \log\left(JCS_n / \sigma'_n\right)$ of the fault of the frictional resistance. The fact that $JCS_n < \sigma'_n$ indicates that the fracture asperities are expected to fail during shearing of the fault. However, to determine the effect of the peak friction angle on the stability of the slope, an analysis with a peak friction value of $\phi_p = 39°$ was also performed. This value corresponds to the peak frictional angle that would have been obtained if the scaling effects on JRC and JCS were neglected.

The main fault was given a zero dilation based on the conclusion that it is very close to residual condition. The shear and normal stiffnesses, JKS and JKN, of the fault were given arbitrary values of 1 GPa. These values were at the high end of the normal and shear stiffnesses expected for faults. However, the values of JKS and JKN are expected to have no significant influence in the results of the modeling as the emphasis of the modeling is large fault displacements (corresponding to the triggering of the slide and the residual deformation of the fault) and the displacement are expected to be much higher that the elastic deformations of the fault.

5.3 - VERTICAL SHEAR FAILURE SURFACE

Properties of the vertical shear failure surface on the north side of the scarp were determined by using the results from the rock and soil laboratory results performed on samples obtained from the site, as well as from empirical correlations. The vertical fault is expected to have failed either by shearing or tensile fracturing of the sandstone which constitutes the main rock type transgressed by the vertical failure surface.

The friction angle used in the analysis was obtained by use of the widely used empirical correlation by Weingarten and Perkins (1995), which relates the friction angle of a rock surface to the porosity of the rock. Porosity tests performed on a core specimen of the pyroclastic rock taken at the site resulted in an average porosity value of 23.8% (Farmer, 2006). According to Weingarten and Perkins (1995) the friction angle of a rock surface is given by:

$$\phi = 57.8 - 105\left(\frac{n}{100}\right) \qquad \text{Equation 5.9}$$

This equation gives ϕ=33° for n=23.8% for the sandstone.

The cohesion value of the vertical shear failure surface was obtained by using unconfined compressive strength test results. The average unconfined compressive strength obtained by testing rock core specimens of the sandstone was approximately 25 MPa (Farmer, 2006). Using a Mohr-Coulomb failure criterion, the unconfined compressive strength *UCS*, can be related to cohesion *c* and friction angle ϕ by the following relationship:

$$UCS = \frac{2c\cos\phi}{1-\sin\phi} \qquad \text{Equation 5.10}$$

Solving Equation 5.10 in terms of cohesion *c* gives:

$$c = \frac{UCS(1-\sin\phi)}{2\cos\phi}$$ Equation 5.11

Substituting *UCS* = 25 MPa and ϕ= 33^o gives *c* = 6.7 MPa for the sandstone.

The average tensile strength σ_t of the vertical shear failure surface was estimated through the results of splitting tensile strength (Brazilian) tests (Farmer, 2006). The results give an estimated tensile strength of the vertical shear surface of σ_t =3 MPa. The normal and shear stiffness of the vertical failure surface are also given values of 1 GPa as in the case of the main fault surface. Dilation is zero for the vertical shear failure surface.

5.4 - OTHER FAILURE SURFACES

The remaining failure surfaces, including the side fault on the top south corner of the scarp, as well as the two failure surfaces forming the valley at the foot of the main scarp, were modeled using the same parameters. These surfaces had zero tensile strength, cohesion and dilation values. The normal and shear stiffness coefficients, JKN and JKS, were considered to be 1 GPa as in the main fault and the vertical shear failure surface.

The peak friction angle ϕ_p for these three surfaces, which consisted mainly of volcanic soils, were based on a report by Tamaoki (2006). According to this report, the peak friction angle was measured from direct shear tests of the volcanic soils and was estimated to be 39° (Fig. 5.3). The direct shear tests were conducted under drained conditions and by shearing the soil under constant shear stress while reducing the effective normal stress until failure is reached. After failure is reached, shearing continued at constant volume condition until residual condition is achieved. Since the "valleys" as well as the side 'fault' on the south top corner of the fault appear to be mainly soil surfaces, a peak friction angle of 39^o seems reasonable and thus it was chosen for the analysis.

Tamaoki (2006) also provides estimates of the residual friction angle of failure surfaces, which is approximately equal to 2°. This estimate was considered excessively low and very conservative, and hence it was decided to use typical residual friction values for soils of volcanic origin. According to Rigo et al. (2006) a typical residual friction angle value for soils of volcanic origin is 30^o (Fig. 5.4). Therefore, since the value reported in Tamaoki (2006) seems unreasonable in comparison with typical values in volcanic soils, the average value from Rigo et al. (2006) of 30^o was chosen for the analysis.

5.5 - SUMMARY OF MATERIAL PROPERTIES USED

Table 5.1 summarizes the materials properties used for the 3DEC modeling of the Guinsaugon slide for the different failure surfaces. In some instance, some of the parameters listed in the table are varied so that parametric analyses can be performed on the sensitivity of the results to the input parameters.

Table 5.1 – Material parameters used for the failure surfaces in the Guinsaugon slide.

Parameter	Main fault	Vertical	Side fault and valleys
Peak friction angle, ϕ_p	25^o, 39^o	33^o	39^o
Residual friction angle, ϕ_r	25^o	33^o	30^o
Dilation angle, ψ	0^o	0^o	0^o
Cohesion, c	0	6.7 MPa	0
Tensile strength, σ_t	0	3 MPa	0

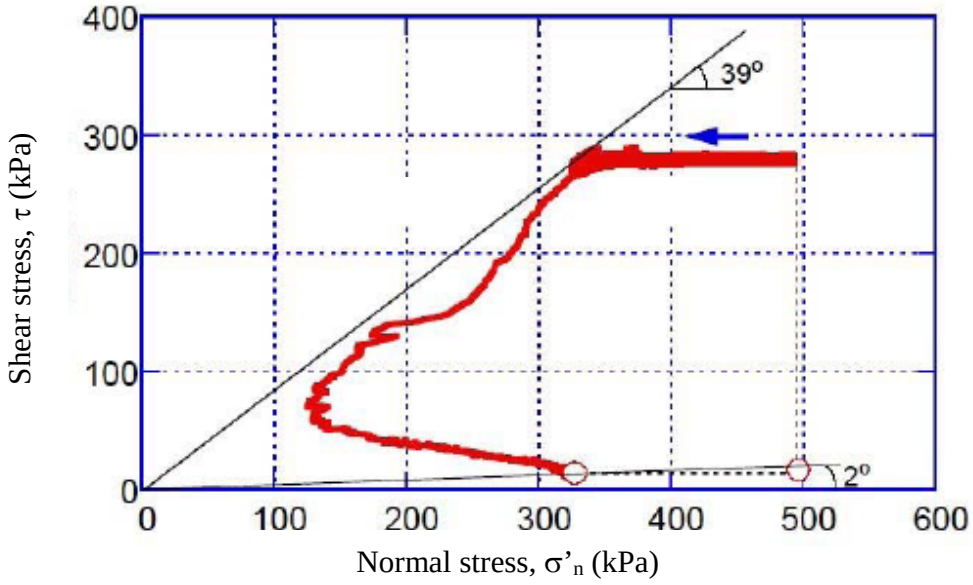

Fig. 5.4 - Results of a direct shear test on volcanic soils from the Guinsaugon slide (Tamaoki, 2006).

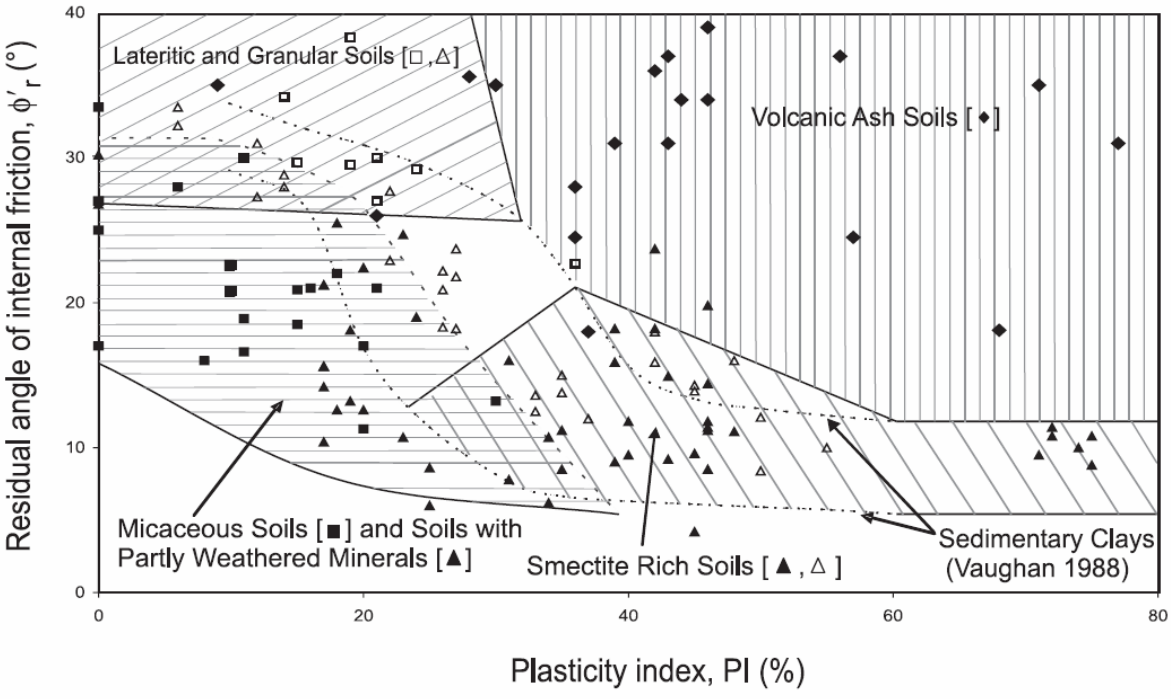

Fig. 5.5 - Residual friction angles for tropical soils (Rigo et al., 2006)

CHAPTER 6: NUMERICAL ANALYSIS OF POSSIBLE TRIGGERING MECHANISM

6.1 - GENERAL

One of the main objectives of the distinct element modeling is to investigate the underlying triggering mechanism responsible for the rockslide as well as the type of slope failure. The two possible events that were considered to have affected the triggering of the Guinsaugon rockslide are the continuous heavy rainfall as well as the small earthquakes that occurred in the morning of February 17th, 2006 near the town of St. Bernard, in Leyte, Philippines. The heavy rainfall will be simulated by hydraulically pressurization of the main fault, while the earthquake forces will be simulated by applying an equivalent horizontal acceleration in the direction of the fault.

The first step in determining the effect of each of the two precursor events to the triggering of the slide, and ultimately the actual triggering mechanism responsible for the massive rockslide is to assume that the overhanging rock is a rigid and intact block that does not contain discontinuities. Also, the sliding block is considered to be moist due to the heavy rain, and thus has an increased unit weight. The analysis will also begin by assuming that the triggering was caused mainly by the hydraulic pressurization of the main fault and the increased unit weight. The effect of the earthquake on the pressurized model will also be studied. All analysis was performed using the digital elevation model and discontinuities of the final 3DEC model described in Chapter 4 of this report. The results of the triggering mechanism distinct element analysis are presented in this chapter.

The analysis itself has been separated in a number of sections in order to better organize the results and conclusions and to make the process used in the analysis simpler and hence more understandable. In order to better organize the procedure that was followed during the numerical analysis an event diagram has been created (Fig. 6.1). The event diagram graphically presents the sequence followed in the analysis and explains the different scenarios and possibilities considered throughout the process of determining the triggering mechanism of the massive Guinsaugon rockslide. The description of the numerical analysis will follow the sequence presented in the event diagram or event tree.

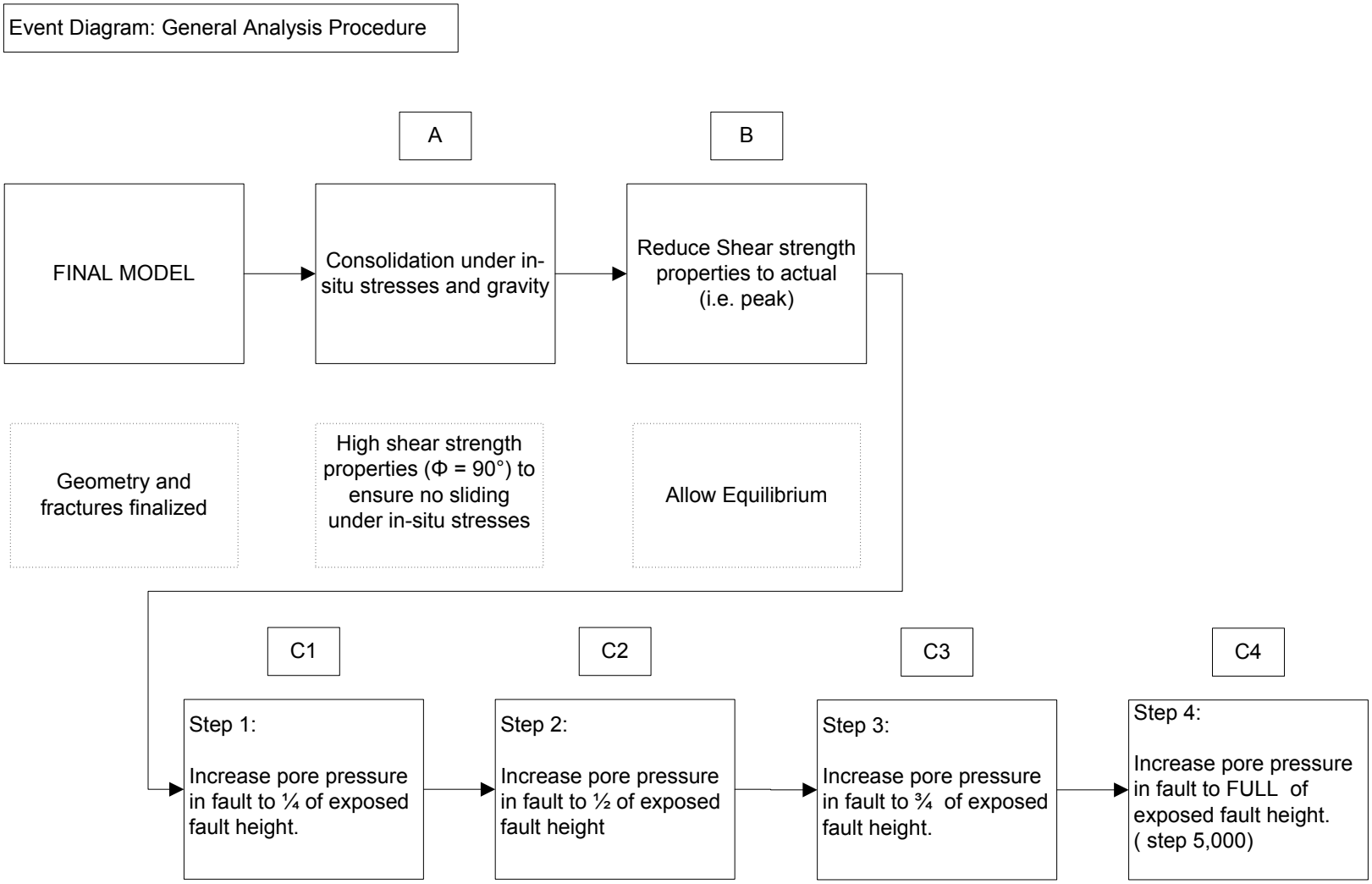

Fig. 6.1: Event Diagram representing general analysis approach

Due to the fact that 3DEC is a dynamic code, the model must reach an initial force-equilibrium state prior to any changes of the material or joint properties can be performed. Equilibrium can be reached by allowing 3DEC to achieve sufficient calculation cycles. The system is in equilibrium when the net unbalanced nodal force vector at each centroid of rigid block is zero or when the transient velocities have become close to zero. Although the actual nodal force vector, or 'unbalanced' force, will never reach zero, the system can be considered stable when the unbalanced force is small compared to the total forces applied to the system. The user is responsible for deciding when the system has reached equilibrium, and this can easily be determined by monitoring the unbalanced force. This can be done either on-screen while the program is cycling or by monitoring history plot of the unbalanced force or any other variable that is expected to stabilize, such as velocity or displacement at a certain point on the grid (Itasca, 1998).

The displacement vector history plots are a good indication of the stability and general behavior of the system. In this case, the displacement vectors at a certain point on the sliding block will be monitored and its history plotted throughout the analysis. The monitored point is shown in Fig. 6.2. History plots will include plots of the displacement vector at the specified point both in the X (East-West) and Y (Elevation) direction.

As a dynamic code, 3DEC is very sensitive such that sudden changes of the applied forces, loads or boundary displacements, which may 'shock' the model, causing extreme and unrealistic behavior of the response, or non-convergence of the analysis. For this reason, each step in the analysis subjects the model to only small changes or increments of the total applied forces or material properties to minimize 'shocking' and achieve more realistic and representative results.

Model parameters were altered only after sufficient calculation cycles were performed and the system reached equilibrium. The sequence followed during the analysis of the triggering mechanism of the slide is described in detail in the following sections. The event tree in Figure 6.1 provides an outline of the analysis procedure that was followed. The following sections may refer to Figure 6.1 extensively for clarification purposes.

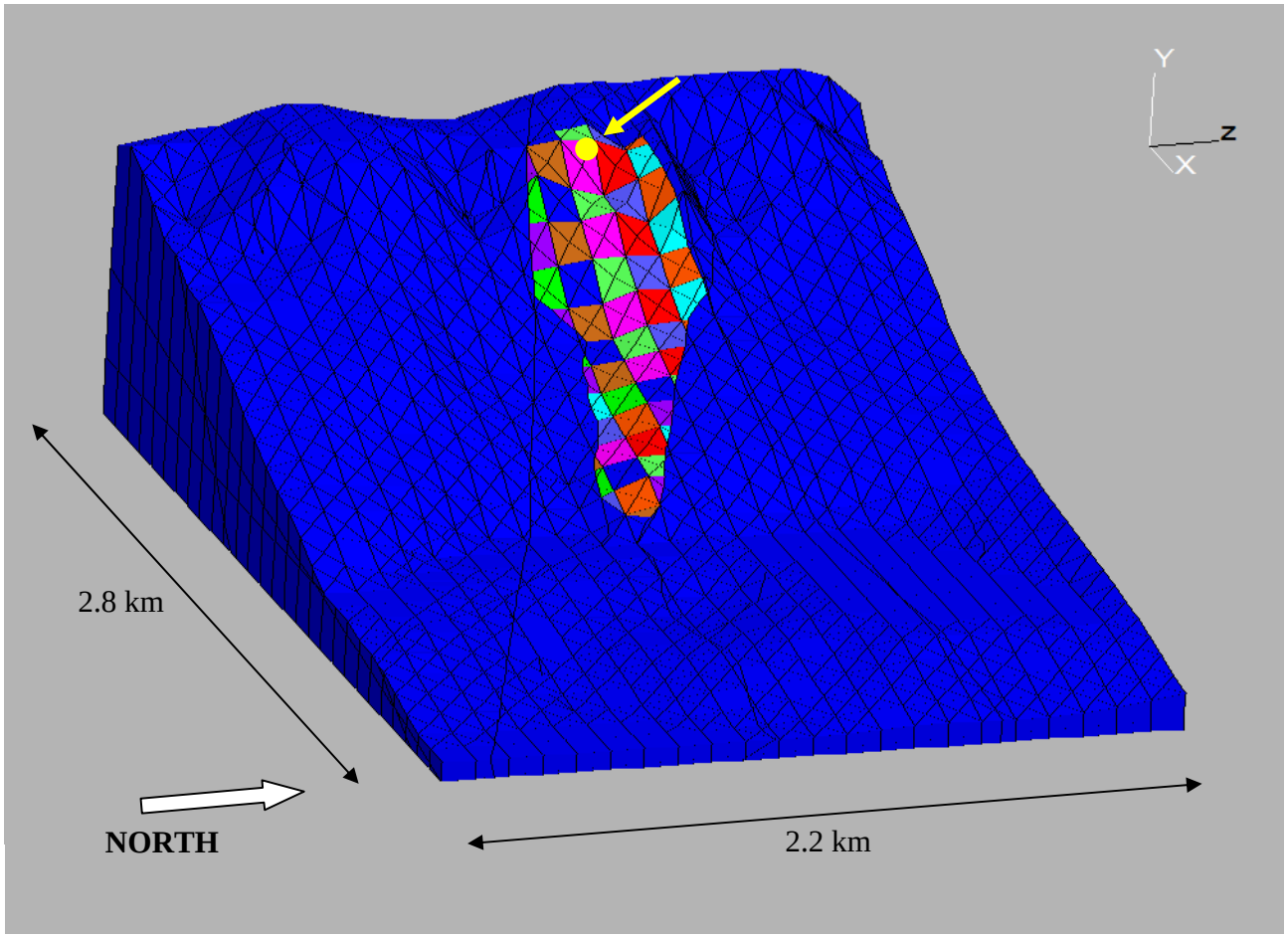

Figure 6.2: Digital Elevation Model of the slide area in 3DEC on a 100 m by 100 m grid showing monitored point on sliding block

6.2 – Initial Equilibrium

6.2.1 – Boundary Conditions

The 3DEC model cannot be used in analysis unless boundary conditions have been specified. Applying boundary conditions can be achieved in two different ways. First, boundary conditions can be applied through the use of the *boundary* command in 3DEC, which is used to specify force, stress and velocity (displacement) boundary conditions. Force and stress boundary conditions can be specified for both rigid and deformable blocks, while velocity boundary conditions can only be specified for deformable blocks. The conditions specified as boundary conditions are fixed and do not change during calculation steps.

Another method of applying boundary constraints to the model is the method that was used in this analysis. Instead of applying boundary conditions to the model by using the built-in 3DEC commands, the necessary boundaries were created by the addition of rectangular blocks surrounding the model (Fig. 6.3). In the model setup step of the analysis, four rectangular 'walls' were created on the north, south, east and bottom sides of the model as shown in Fig. 6.3. These rectangular rigid blocks are always present during the calculation procedure but are hidden for visualization purposes. These models were not considered during the creation of the discontinuities in the model and thus are completely intact. The presence of these rectangular blocks prevent the elevation model from moving in space during the calculation process and act as the explicitly specified boundary conditions would.

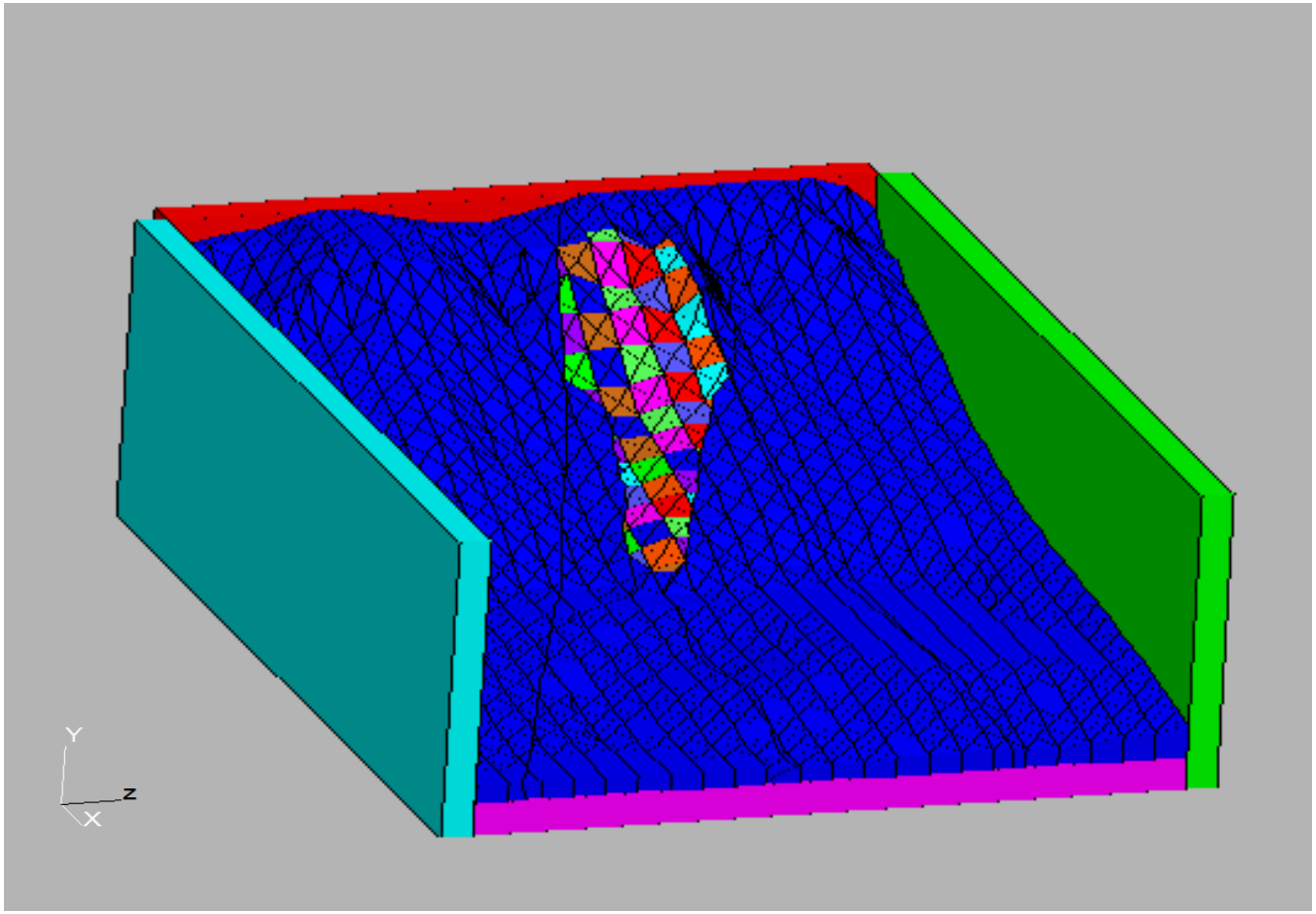

Fig. 6.3: Final 3DEC model showing boundary restraints.

6.2.2 - CONSOLIDATION UNDER IN-SITU STRESSES (STAGE A)

The first step in performing the distinct element analysis is to ensure that the system is in equilibrium under the initial in situ stresses. Given that the individual blocks in the model are assumed rigid, initial stress conditions could not be specified for stresses in the actual blocks. However, initial stress conditions were specified for all normal and shear stresses along joints between the rigid blocks. The model was subjected to in-situ horizontal and vertical stresses by using the *insitu* 3DEC command. In situ stresses specified initially can change as the calculation proceeds, in contrast to the boundary conditions as mentioned above (Itasca, 1998).

In addition to the in situ stresses applied to the 3DEC model, the effect of gravity on the rigid blocks was also considered in this first step of the analysis. The acceleration of gravity, approximately 10 m/s^2, was applied in the vertical direction. The effect of gravity in this initial step is to possibly close any gaps or openings that may have been created during the introduction of the failure surfaces around the block.

In order to minimize the 'shocking' effect, as previously mentioned, the shear strength parameters of the existing failure surfaces are set to an unreasonably high value during the 'consolidation' stages to generate the initial in-situ stresses along the discontinuities. This will ensure that the block will not slide under its own weight when subjected to the in situ stresses and will ease 3DEC in reaching equilibrium. More specifically, the friction angles of all five failure surfaces surrounding the sliding block were set to 90^o, ensuring zero sliding movement of the block. After allowing sufficient calculation cycles, the displacement vectors in the model and history plots of the horizontal and vertical component of the displacement of the monitored point are shown in Figs. 6.4 and 6.5.

Fig. 6.4 shows that the effect of gravity was to close the small gaps along the failure surfaces since all displacement vectors are purely vertical and the total displacement is very small. The displacement history plot in Fig. 6.5 indicates that the overhanging rock has moved by a very small distance and has stopped, since the plot levels out with increasing calculation steps. This proves that the model has reached equilibrium and further changes can now be made to the model.

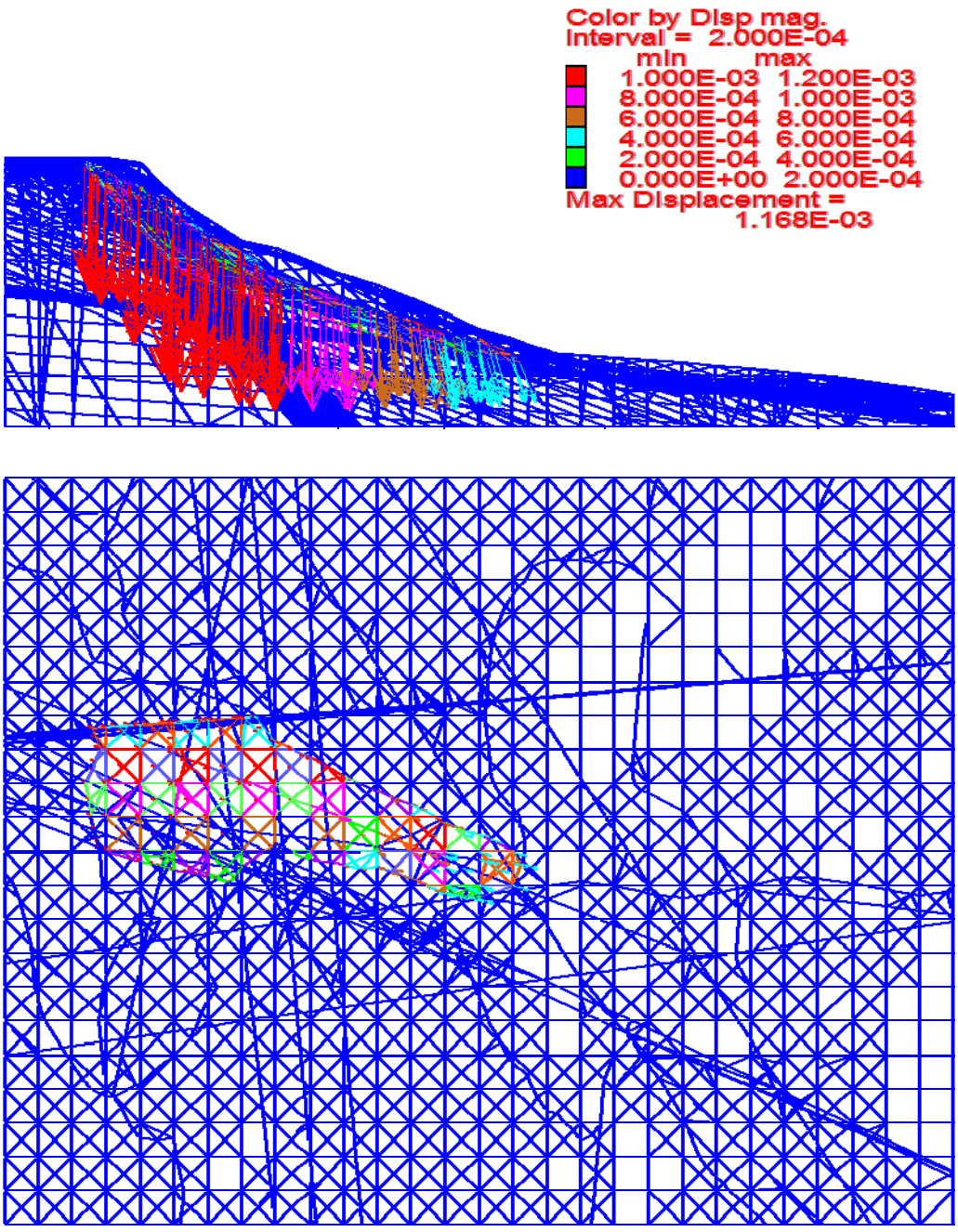

Fig. 6.4: Profile and plan view of 3DEC model showing displacement vectors of overhanging block – Stage A

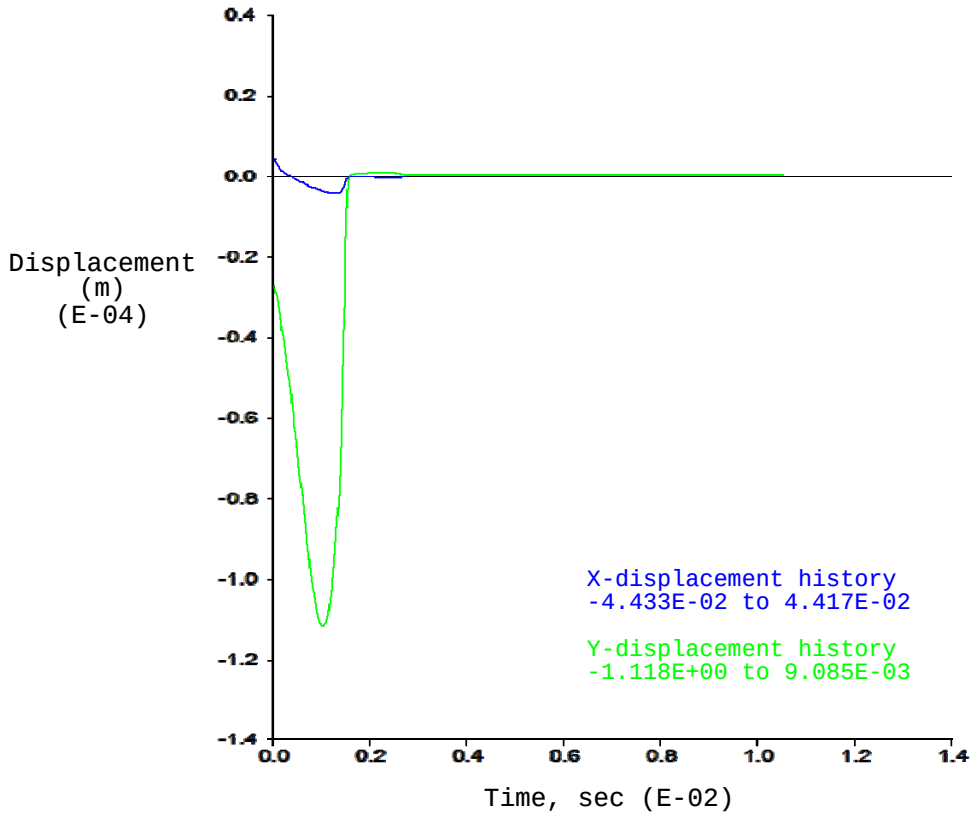

Fig. 6.5: Displacement history plot corresponding to point A on sliding block vs. Time – Stage-A

6.2.3 - REDUCE FRICTION ANGLE (B)

Once the model reached equilibrium under in-situ stresses and the acceleration of gravity, shear strength properties of the failure surfaces were reduced to the actual estimated values. An unreasonably high friction angle of 90^o was used in the consolidation step (Stage A) to ensure that the block would not slide along the failure surfaces. Once equilibrium was reached, as shown in the previous section, the shear strength properties of the failure surfaces were reduced to the peak shear strength properties calculated in Chapter 5.

The first step prior to proceeding with the actual numerical analysis of the pressurized mode was to ensure that the overhanging block does not have the tendency to slide under its own weight. A simple numerical analysis on the selected 3DEC model was performed, considering the overhanging rock as one rigid, intact block having a moist unit weight equal to $20.5kN/m^3$, as determined in Chapter 5. The peak shear strength properties used for each of the modeled failure surfaces were calculated in Chapter 5 and are summarized below. Properties that are not mentioned were considered to be zero.

- Main Fault:
  ϕ_p = peak friction angle = 25^o
  JKN = joint normal stiffness = 1GPa
  JKS = joint shear stiffness = 1GPa

- Vertical Shear Failure Surface:
  ϕ_p = peak friction angle = 33^o
  c = cohesion = 6.7 MPa
  σ_t = tensile strength = 3 MPa
  JKN = joint normal stiffness = 1GPa
  JKS = joint shear stiffness = 1GPa

- Side Fault and Left and Right Valley surfaces:
  ϕ_p = peak friction angle = 39^o

JKN = joint normal stiffness = 1GPa
JKS = joint shear stiffness = 1GPa

Sufficient number of calculation steps (cycles) was allowed in order for the model to reach equilibrium under the actual peak shear strength properties, the in situ stresses and the acceleration of gravity. Displacement and unbalanced force history plots indicated that 2,000 calculation cycles were sufficient for the system to reach equilibrium (Figs. 6.6 and 6.7). The displacement vectors after 2,000 calculation steps in the overhanging rock are shown in Fig. 6.6. The relatively insignificant maximum displacement (about 0.6 mm) indicates that the block did not undergo any significant movement and that the model is still in equilibrium and does not slide under its own weight when the fault is not pressurized. The calculated initial displacements along the discontinuities will be set to zero before subsequent analyses for triggering of the slide are performed.

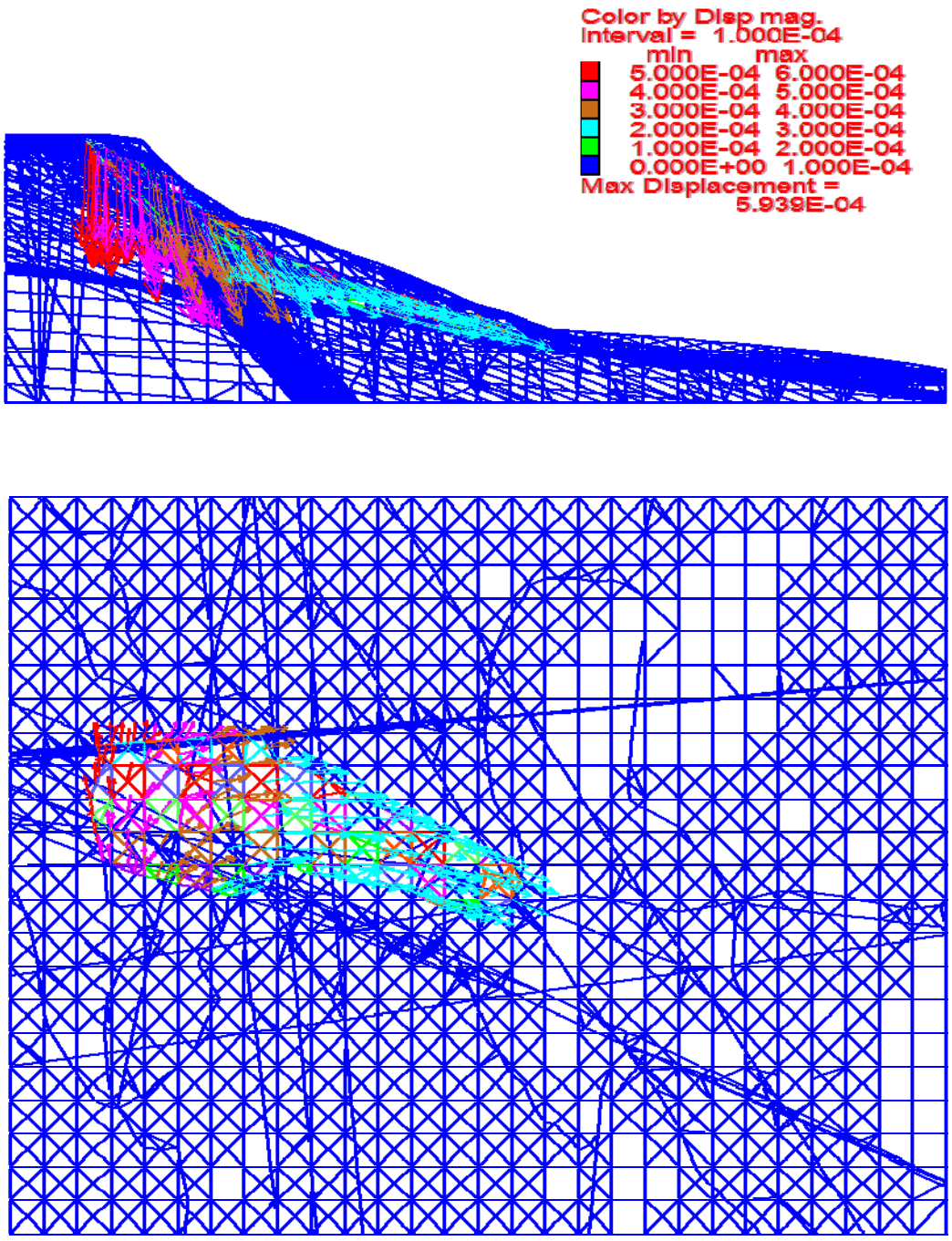

Fig. 6.6: Profile and plan view of 3DEC model showing displacement vectors of overhanging block – Stage B

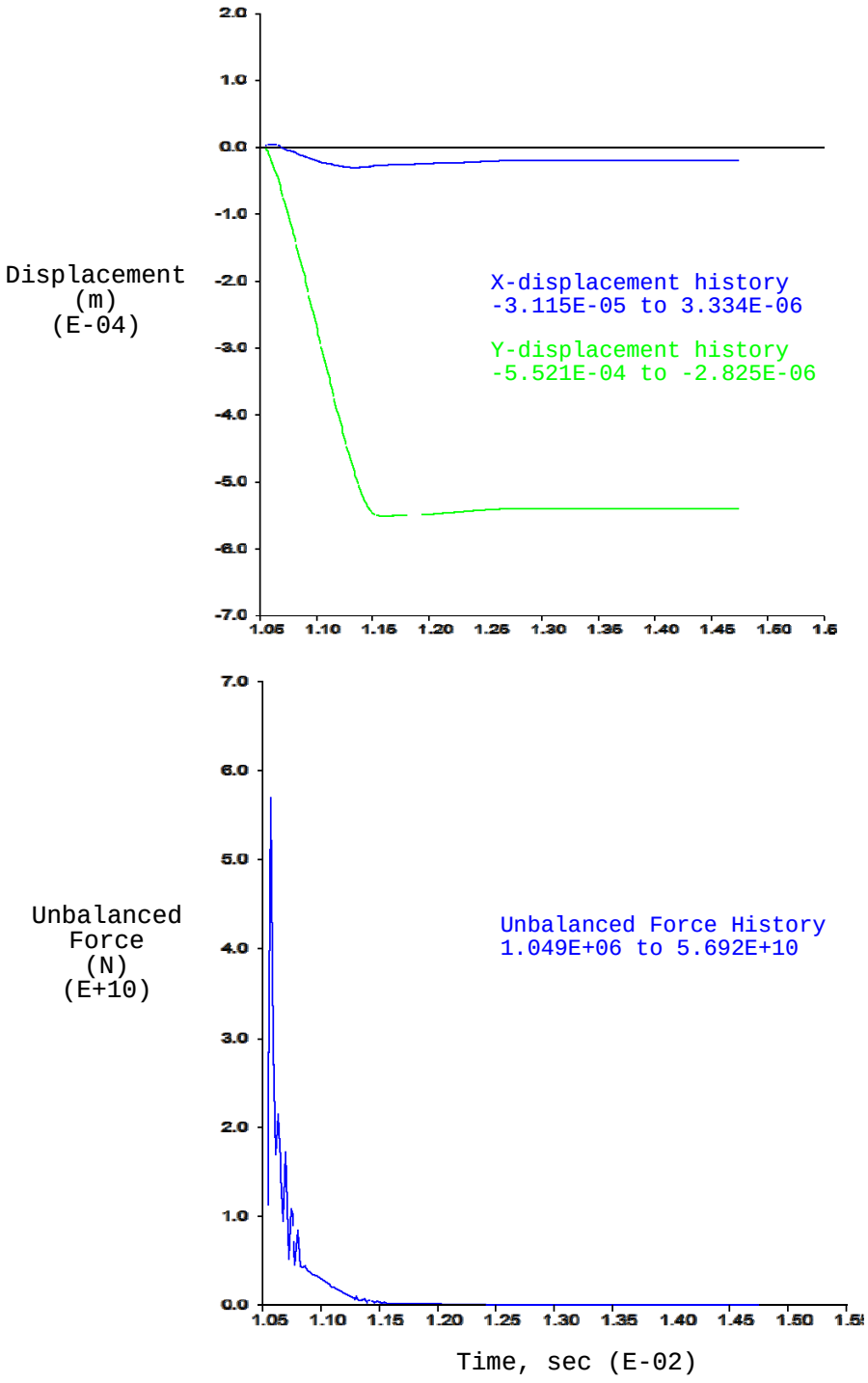

Fig. 6.7: Top: Displacement history plot of point A on sliding block vs. Time
Bottom: Unbalanced Force History plot of model vs. Time
(Stage B)

6.3 – HYDRAULIC PRESSURIZATION

The effect of the continuous heavy rainfall in the Southern Leyte region in the Philippines in February, 2006 on the triggering of the massive Guinsaugon rockslide will be modeled in 3DEC by assuming hydraulic pressurization of the main fault. The fault will be assumed to be pressurized with a linearly varying hydrostatic pore pressure acting perpendicular to the fault surface. Fig. 6.8 provides a graphical representation of the main fault being subjected to linearly varying hydraulic pressure.

The pore pressure at any height, h, from the top of the exposed fault surface is given by:

$$p(h) = \gamma_w \cdot h \qquad \text{Equation 6.1}$$

where,

p = pore pressure at any height

h = height measured from the top of the exposed fault surface (in m)

γ_w = unit weight of water = 9.81 kN/m^3

Assuming the fault is full, the total pore pressure at the bottom of the model, i.e. at zero elevation and 776 m from the top, is calculated for h=776m. Hence, Equation 6.1 results in $p(776m) = 7.6MPa$.

Similarly, the total pore pressure at the bottom of the exposed portion of the fault surface, which is located at an elevation of 440 m and therefore 336 m from the top, is calculated for h=336m. Hence Equation 6.1 results in $p(336m) = 3.3MPa$.

The pore pressure at the top of the fault surface, i.e. at h=0, is, as expected, $p(0m) = 0$.

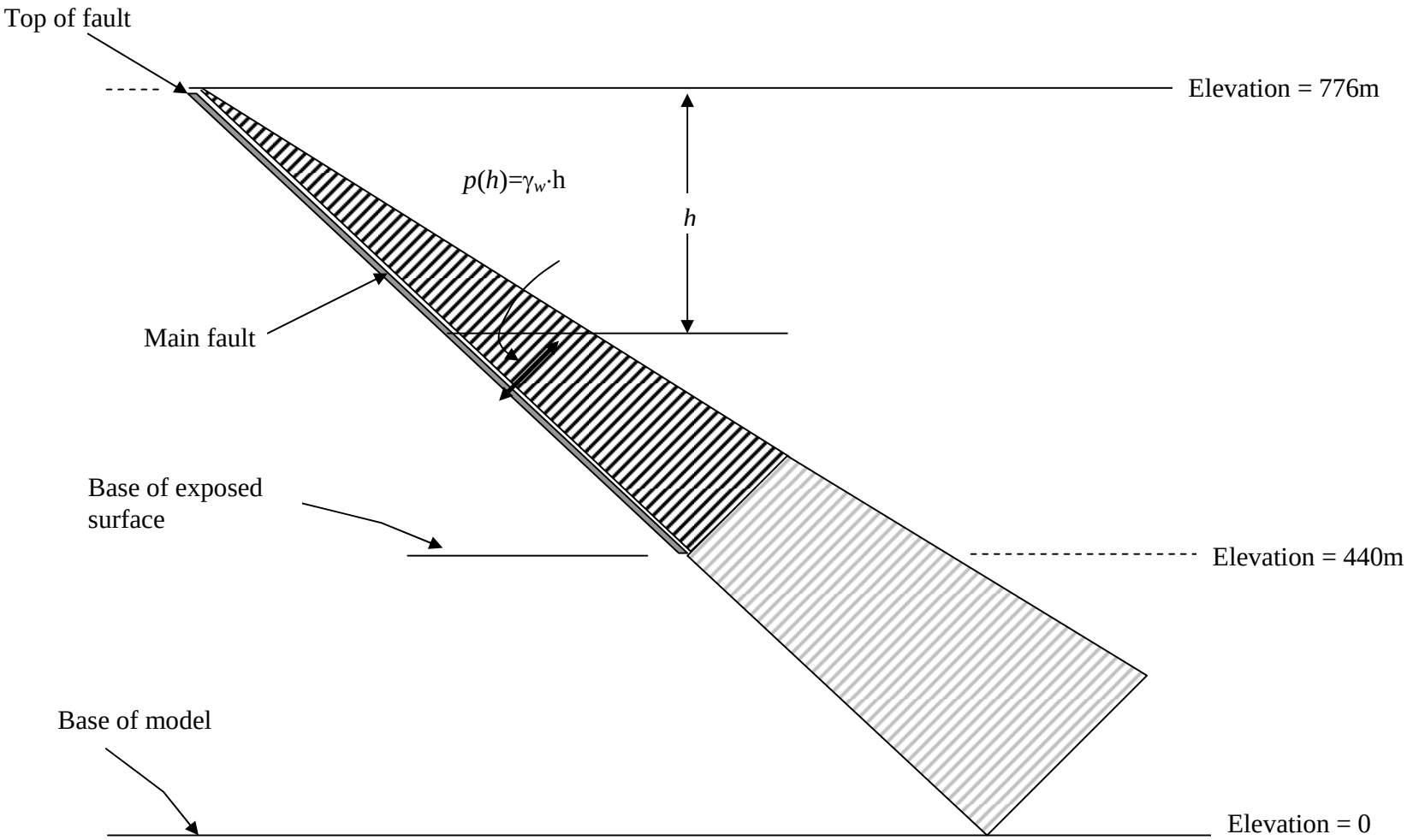

Figure 6.8: Main Fault subject to linearly varying pore pressure in the fault.

In order to avoid 'shocking' the system by suddenly applying large magnitude of water pressure in the fault, it was decided that the hydraulic pressurization will be applied in four separate steps. After each application the system will be allowed to come to equilibrium, if possible, by allowing 3DEC to perform sufficient calculation cycles.

This gradual method of application of the pore pressure in the main fault also serves another important purpose. It provides an indication of the minimum pore pressure in the fault necessary to cause movement or, in other words, trigger the sliding of the overhanging block. The results after each of the four increments of pressure will be analyzed to determine whether or not the hydraulic pressure applied would be sufficient to cause the triggering of the slide.

The total calculated pore pressure of 3.3 MPa at the bottom of the *exposed* fault surface will be reached gradually by applying hydraulic pressure in four steps. The steps have been separated such that the exposed fault surface will be filled gradually from ¼ of the total exposed surface height to full height. More specifically, in the first step a pore pressure equivalent to filling the exposed fault to ¼ of its height with water will be applied. In the second step, sufficient pore pressure will be added to reach a total pore pressure equivalent to filling the exposed fault to ½ of its height with water. In the third step, sufficient pore pressure will be added to reach a total pore pressure equivalent to filling the exposed fault to ¾ of its height with water. The final step will add sufficient pressure to reach a total hydraulic pressure equivalent to the full height of the exposed fault being filled with water. Fig. 6.9 graphically indicates the hydraulic pressure applied in each of the four steps.

The pore pressure at the base of the exposed fault surface for each step is calculated using Equation 6.1:

Step 1: $p(84m) = \gamma_w \cdot h = (9.8kN/m^3)(84m) = 823kPa$

Step 2: $p(168m) = \gamma_w \cdot h = (9.8kN/m^3)(168m) = 1.64MPa$

Step 3: $p(252m) = \gamma_w \cdot h = (9.8kN/m^3)(252m) = 2.5MPa$

Step4: $p(336m) = \gamma_w \cdot h = (9.8kN/m^3)(336m) = 3.3MPa$

Gradual Application of Hydraulic Pore Pressure in Main Fault

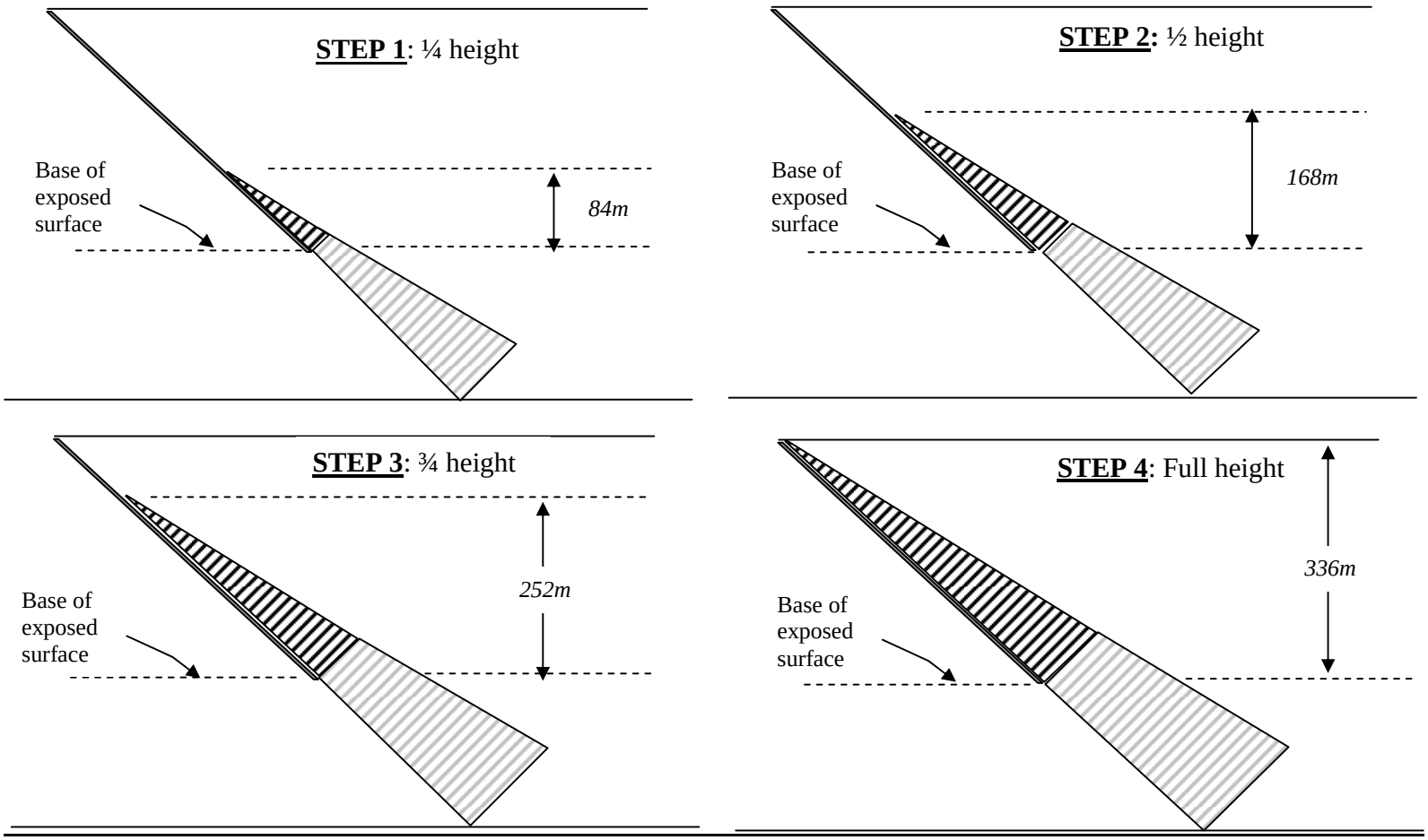

Figure 6.9: Graphical representation of gradual application of pore pressure in the main fault.

6.3.1 – APPLICATION OF PORE PRESSURE – STEP 1 (C1))

As previously mentioned, the first step in the pore pressure application process involves the application of a pore pressure equivalent to pressure induced by ¼ of the exposed fault height filled with water (Fig. 6.10). This results in a 823 kPa total hydrostatic pressure at the base of the exposed surface (elevation 440 m) and consequently in a 5.1 MPa hydrostatic pressure at the base of the model. It must be noted that despite the fact that the entire main fault surface is subjected to hydrostatic pressure, the section below the exposed area does not have an effect on the results since the material not involved in the sliding block is considered rigid and intact and thus cannot separate.

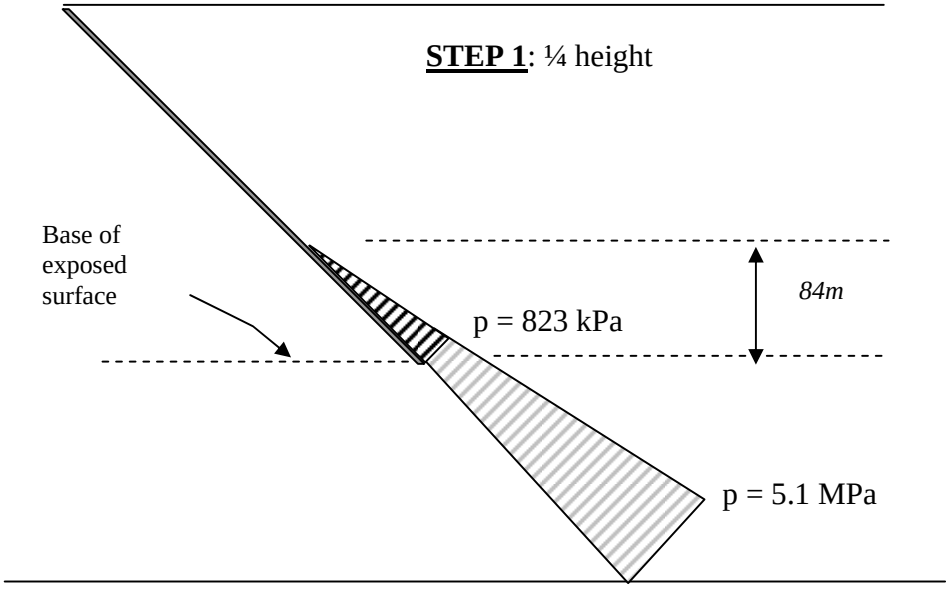

Figure 6.10: First step in hydraulic pressurization process

Once the first step of hydraulic pressure is applied, 3DEC is prompted to perform five thousand calculation cycles. The results after completion of the calculation are shown in Figs. 6.11 and 6.12. The displacement vectors on the sliding block clearly show the effect of the hydrostatic pressure on the behavior of the block itself. Even though the total displacement is minimal, the direction of the displacement vectors indicates that the applied hydrostatic pressure has caused the fault to open or be

'hydraulically parted' by only 4e-5 m. Hence, it can be concluded that a hydrostatic pressure equivalent to pressure induced by ¼ of the exposed fault height filled with water is *not* sufficient to initiate sliding of the overhanging rock.

The history plots of the horizontal and vertical displacement, as well as the history plots of the total unbalanced force in the model indicate that the system has reached equilibrium after being briefly loaded by the applied pore pressure in the fault. The upward direction of the displacement vectors indicate that the hydrostatic pressure is causing the fault to open, but is not causing sliding of the block itself. Hence, more pressure is required to initiate the slide.

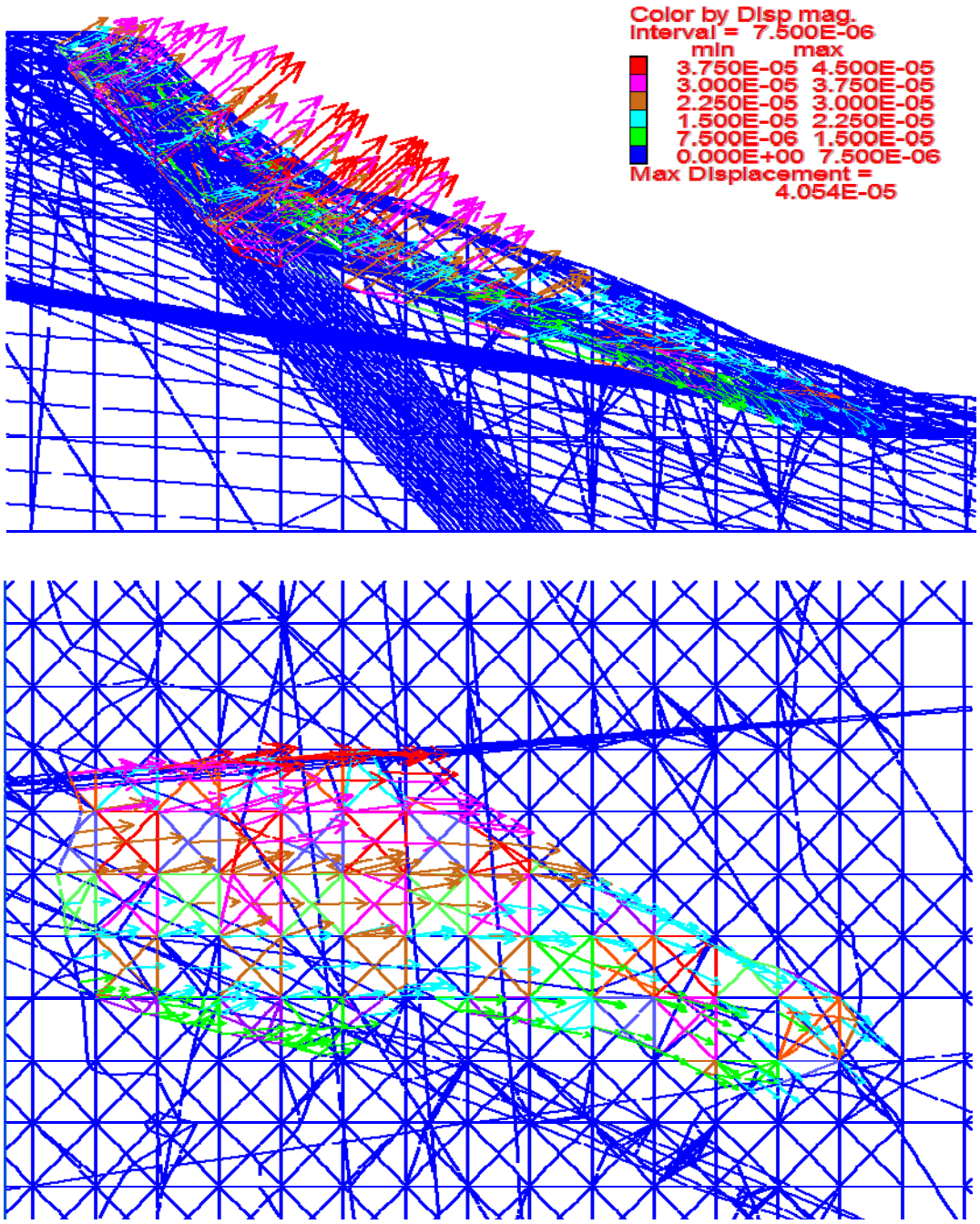

Fig. 6.11: Profile and plan view of 3DEC model showing displacement vectors of overhanging block – Scenario C1

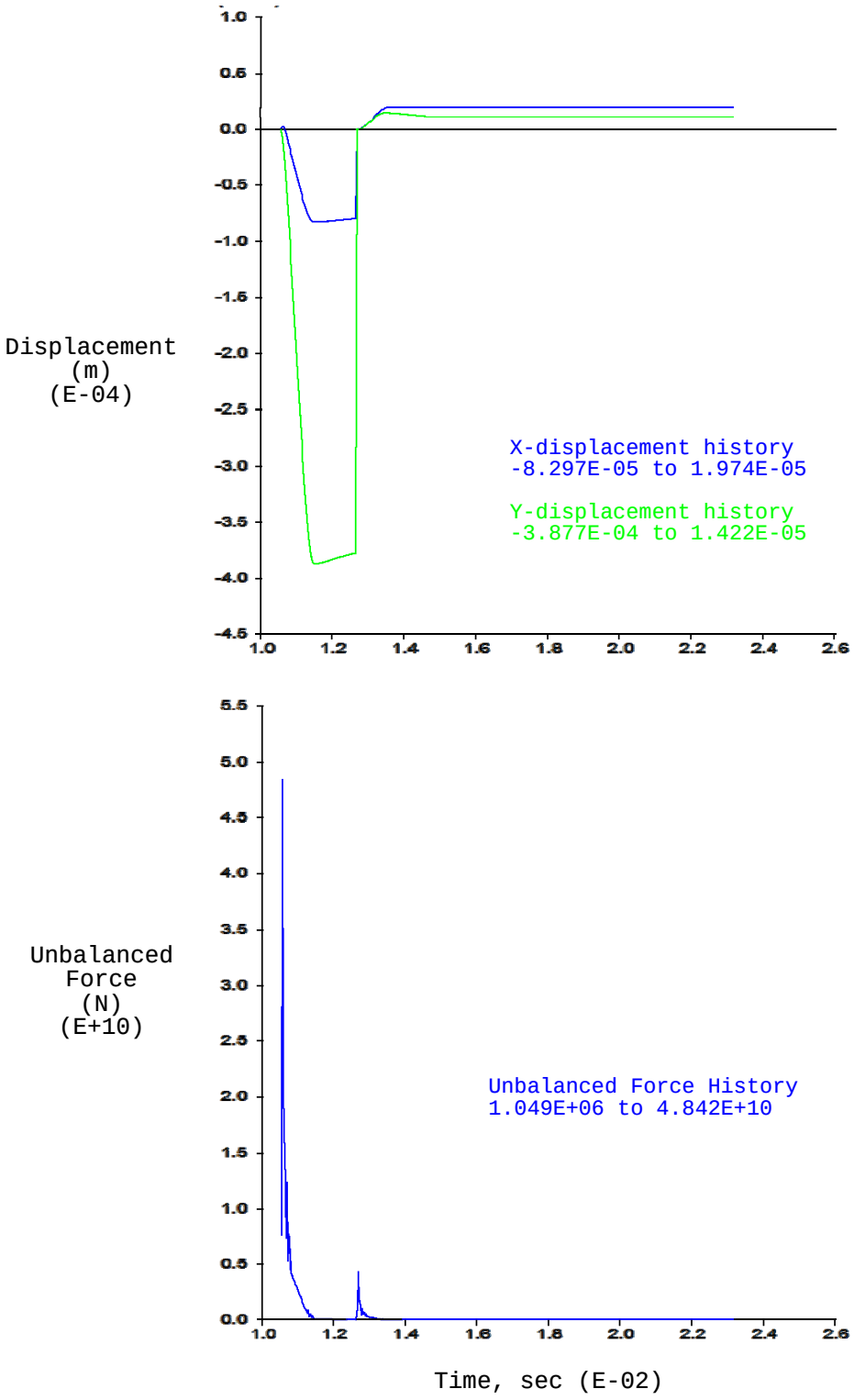

Fig. 6.12: Top: Displacement history plot of point A on sliding block vs. Time
Bottom: Unbalanced Force History plot of model vs. Time (Scenario C1)

6.3.2 – APPLICATION OF PORE PRESSURE – STEP 2 (C2)

The second step in the pore pressure application process involves the addition of pressure in order to achieve a total pore pressure equivalent to pressure induced by ½ of the exposed fault height filled with water (Fig. 6.13). This results in a total of 1.64 MPa total hydrostatic pressure at the base of the exposed surface and a 5.9 MPa hydrostatic pressure at the base of the model.

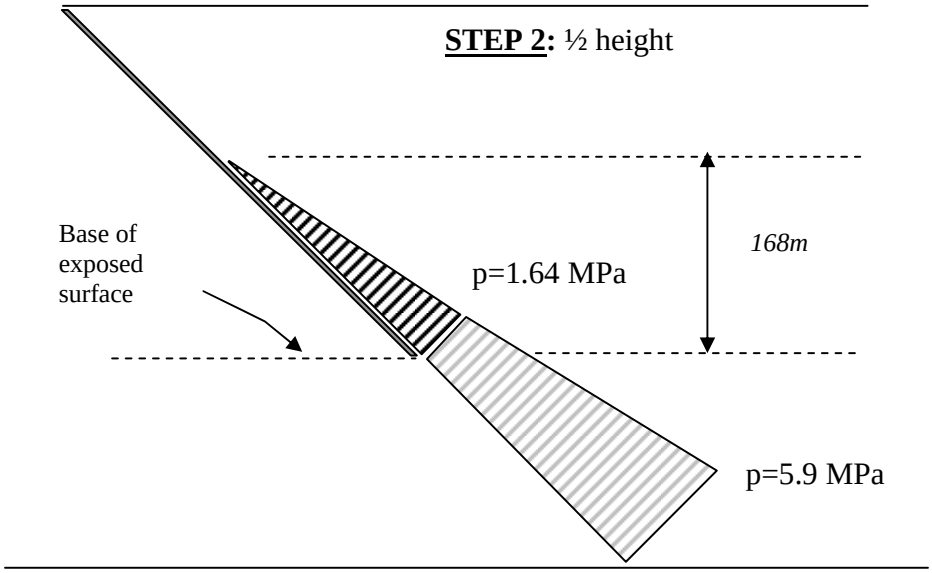

Figure 6.13: Second step in hydraulic pressurization process

After increase of the total hydrostatic pressure from Step 1, 3DEC was allowed to perform five thousand calculation cycles. The results after completion of the calculation are shown in Figs. 6.14 and 6.15. The displacement vectors on the sliding block clearly show the effect of the hydrostatic pressure on the behavior of the block itself. The total displacement has increased from Step 1 but the direction of the displacement vectors is still upwards. Fig. 6.14 indicates that the applied hydrostatic pressure is causing the fault to open by 1.5e-4 m but without causing any sliding to the overhanging rock. Hence, it can be concluded that a hydrostatic pressure equivalent to pressure induced by ½ of the exposed fault height filled with water is *not* sufficient to initiate sliding of the overhanging rock. The displacement and unbalanced force history plots also indicate that the system has reached equilibrium within the five thousand cycles allowed.

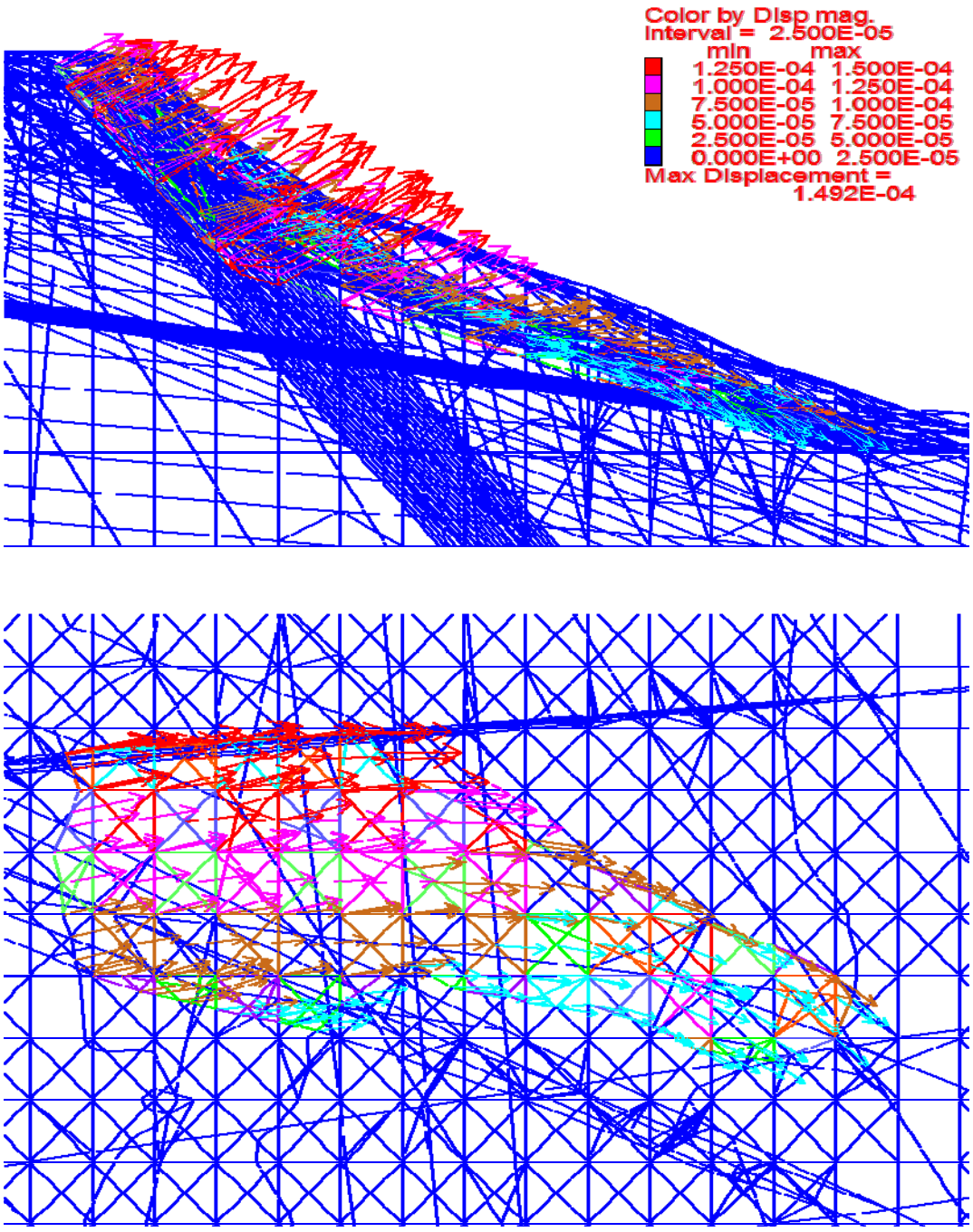

Fig. 6.14: Profile and plan view of 3DEC model showing displacement vectors of overhanging block – Scenario C2

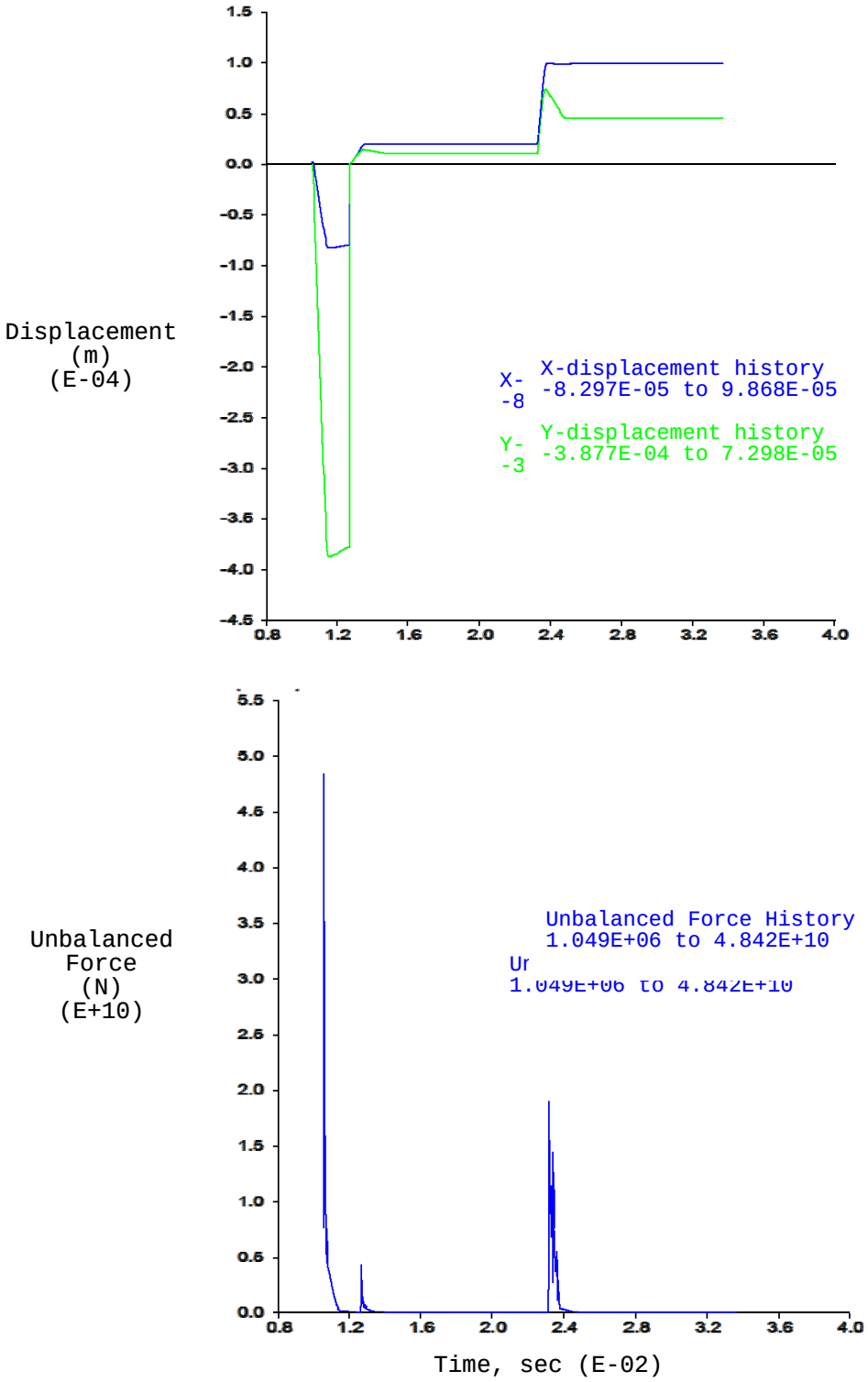

Fig. 6.15: Top: Displacement history plot of point A on sliding block vs. Time
Bottom: Unbalanced Force History plot of model vs. Time (Scenario C2)

6.3.3 – APPLICATION OF PORE PRESSURE – STEP 3 (C3)

The third step in the pore pressure application process involves the addition of pressure in order to achieve a total pore pressure equivalent to pressure induced by ¾ of the exposed fault height filled with water (Fig. 6.16). This results in a total of 2.5 MPa total hydrostatic pressure at the base of the exposed surface and a 6.8 MPa hydrostatic pressure at the base of the model.

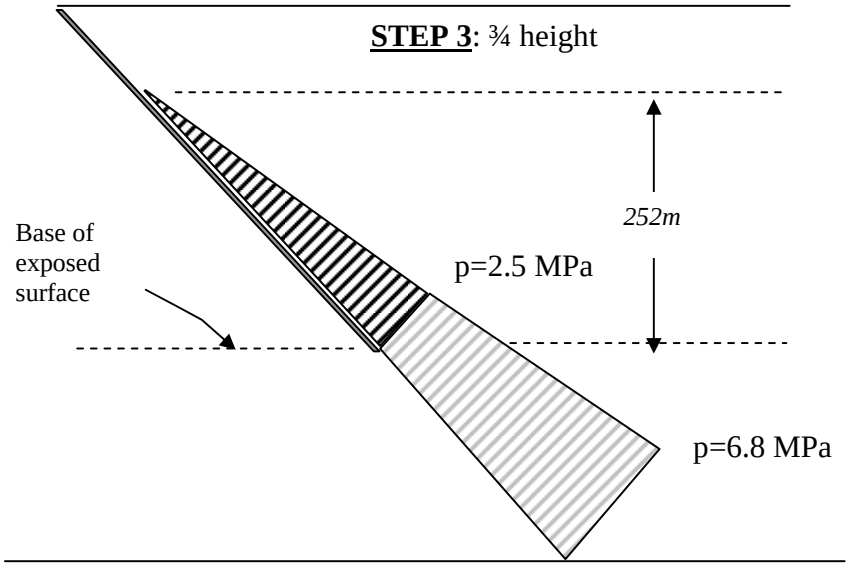

Figure 6.16: Third step in hydraulic pressurization process

After increase of the total hydrostatic pressure from Step 2, 3DEC was allowed to perform five thousand calculation cycles. The results after completion of the calculation are shown in Figs. 6.17 and 6.18. The displacement vectors on the sliding block clearly show the effect of the hydrostatic pressure on the behavior of the block itself. The total displacement has increased from Step 3 but the direction of the displacement vectors is still upwards. This indicates that the applied hydrostatic pressure is causing the fault to open by 5.1e-4 m but without causing any sliding to the overhanging rock. Hence, it can be concluded that a hydrostatic pressure equivalent to pressure induced by ¾ of the exposed fault height filled with water is *not* sufficient to initiate sliding of the overhanging rock. The displacement and unbalanced force history plots indicate that the system has reached equilibrium within the five thousand cycles allowed.

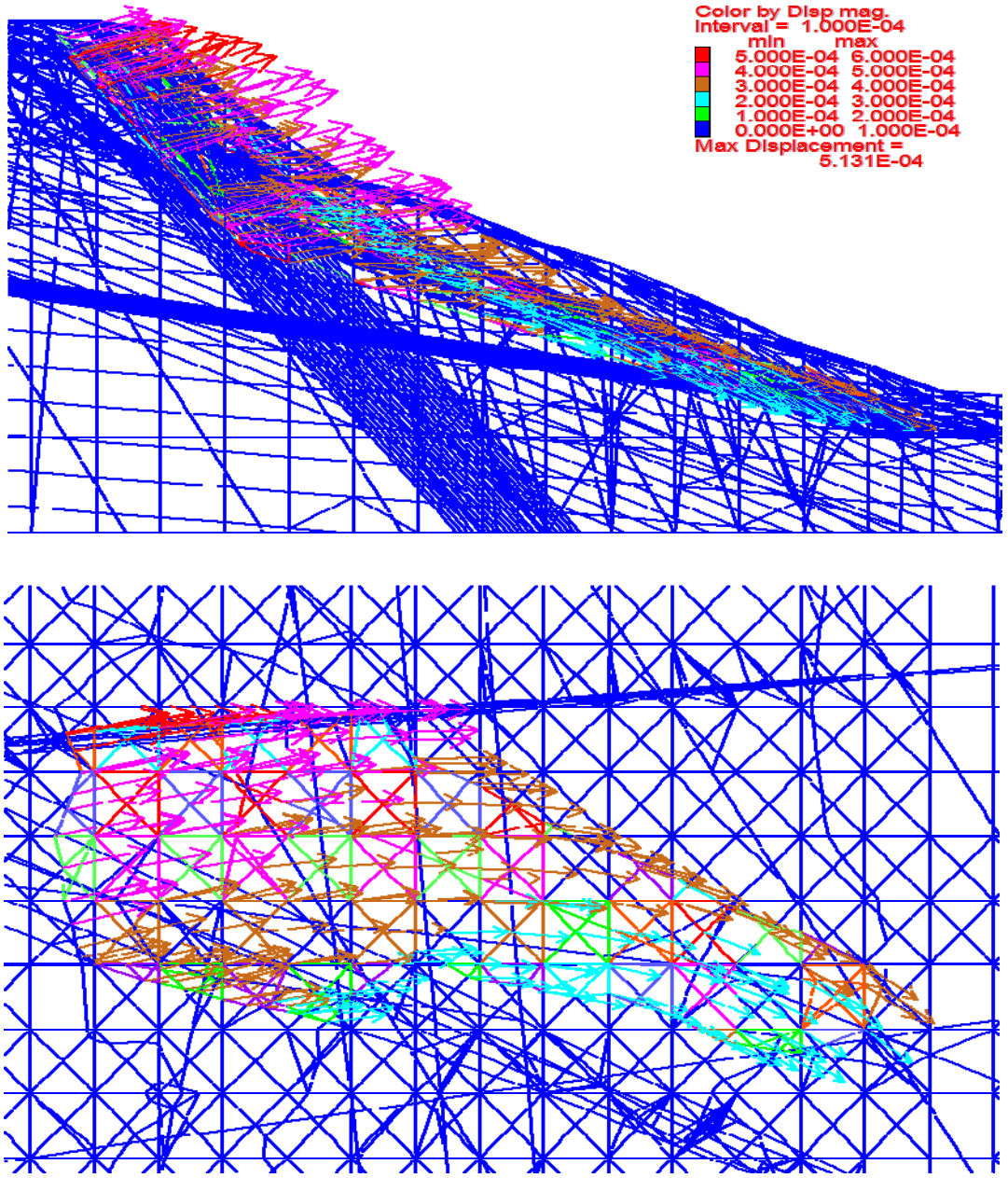

Fig. 6.17: Profile and plan view of 3DEC model showing displacement vectors of overhanging block – Scenario C3

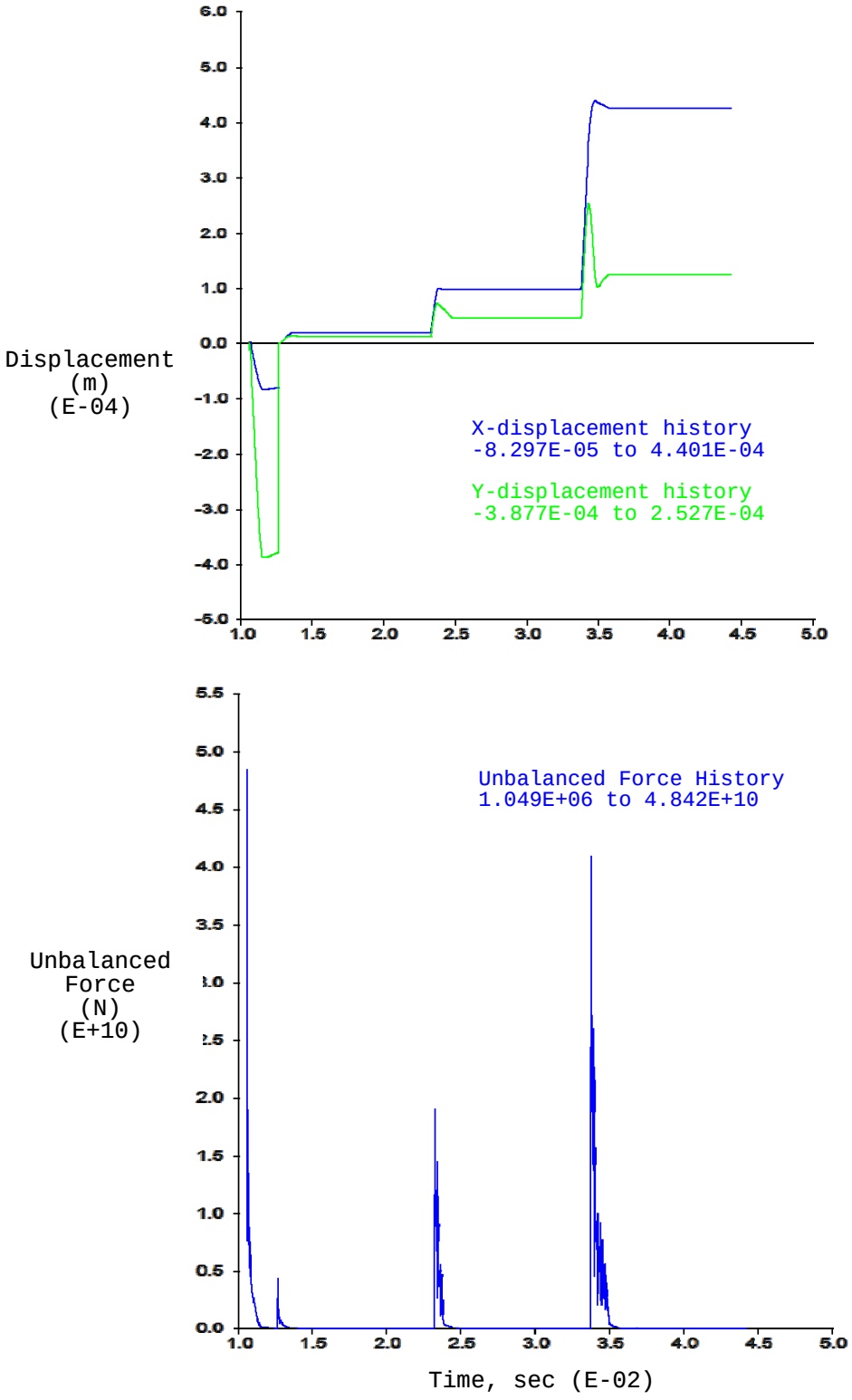

Fig. 6.18: Top: Displacement history plot of point A on sliding block vs. Time
Bottom: Unbalanced Force History plot of model vs. Time (Scenario C3)

6.3.4 – APPLICATION OF PORE PRESSURE – STEP 4 (C4)

The fourth and last step in the pore pressure application analysis of the triggering of the slide involves the application of pressure in order to achieve a total pore pressure equivalent to pressure induced by the full height of the exposed fault filled with water (Fig. 6.19). This results in a total of 3.3 MPa total hydrostatic pressure at the base of the exposed surface and a 7.6 MPa hydrostatic pressure at the base of the model.

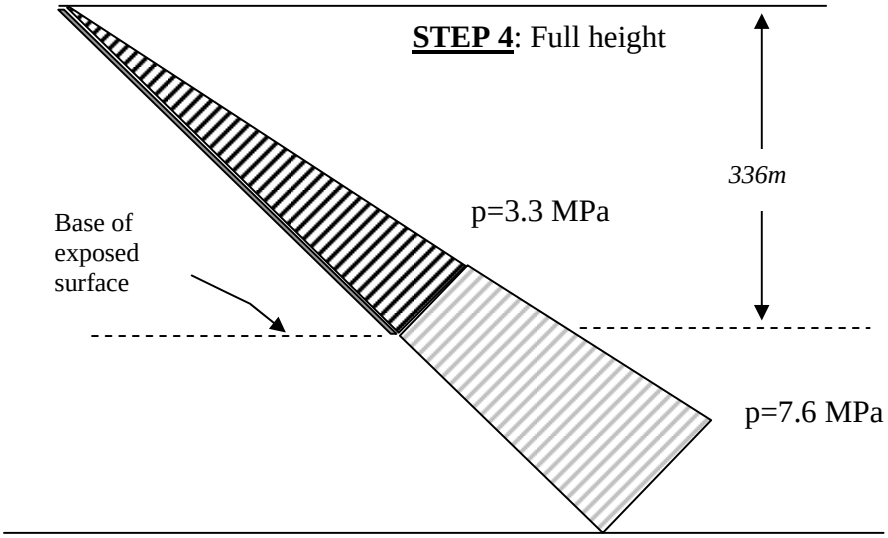

Figure 6.19: Fourth and last step in hydraulic pressurization process

After increase of the total hydrostatic pressure from Step 3, 3DEC was allowed to perform five thousand calculation cycles. The results after completion of the calculation are shown in Figs. 6.20 and 6.21. The displacement vectors on the sliding block clearly show the effect of the hydrostatic pressure on the behavior of the block itself.

In comparison to the three previous steps, when the total hydrostatic pressure was less than maximum, the displacement vectors in this case have changed direction and are pointing downslope rather than upward as in the previous steps. Also, the magnitude of the displacement is considered large enough, in the order of a few mm, to cause the decrease of the shear strength properties of the failure surfaces from peak to residual. The fact that the direction of the displacement vectors has reversed is an indication that the overhanging rock has begun to slide along the prescribed failure

surfaces. Hence, this proves that in the case when the fault is full of water, the pore pressure generated by the water in the fracture is enough to trigger sliding of the block.

Despite the fact that the displacement vectors have reversed direction, from predominantly upwards to downwards movement, the displacement history plot, as well as the unbalanced force history plot indicate that the block has stopped moving and has reached equilibrium. This suggests that although the full height hydrostatic pressure is sufficient to initiate sliding it is not sufficient to cause further downward movement and sliding of the monolithic block. It is possible that the block, being intact and rigid, might have been 'wedged' in the valley at the foot of the main scarp and not be able to slide further as is. Additionally, the reduction of shear strength values from peak to residual, which will be applied at the next step of the analysis, may be needed to cause the block to slide monolithically some additional distance.

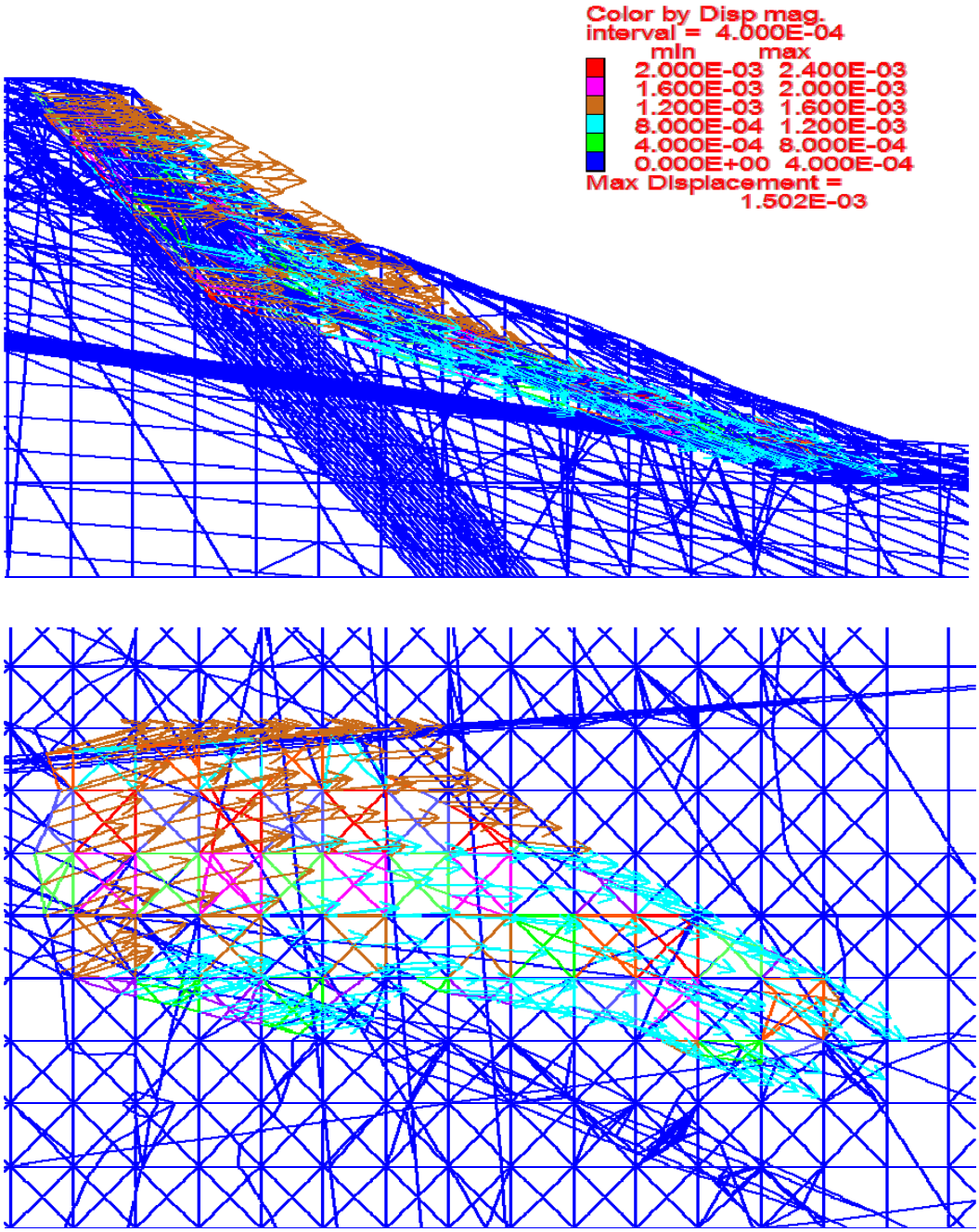

Fig. 6.20: Profile and plan view of 3DEC model showing displacement vectors of overhanging block – Scenario C4

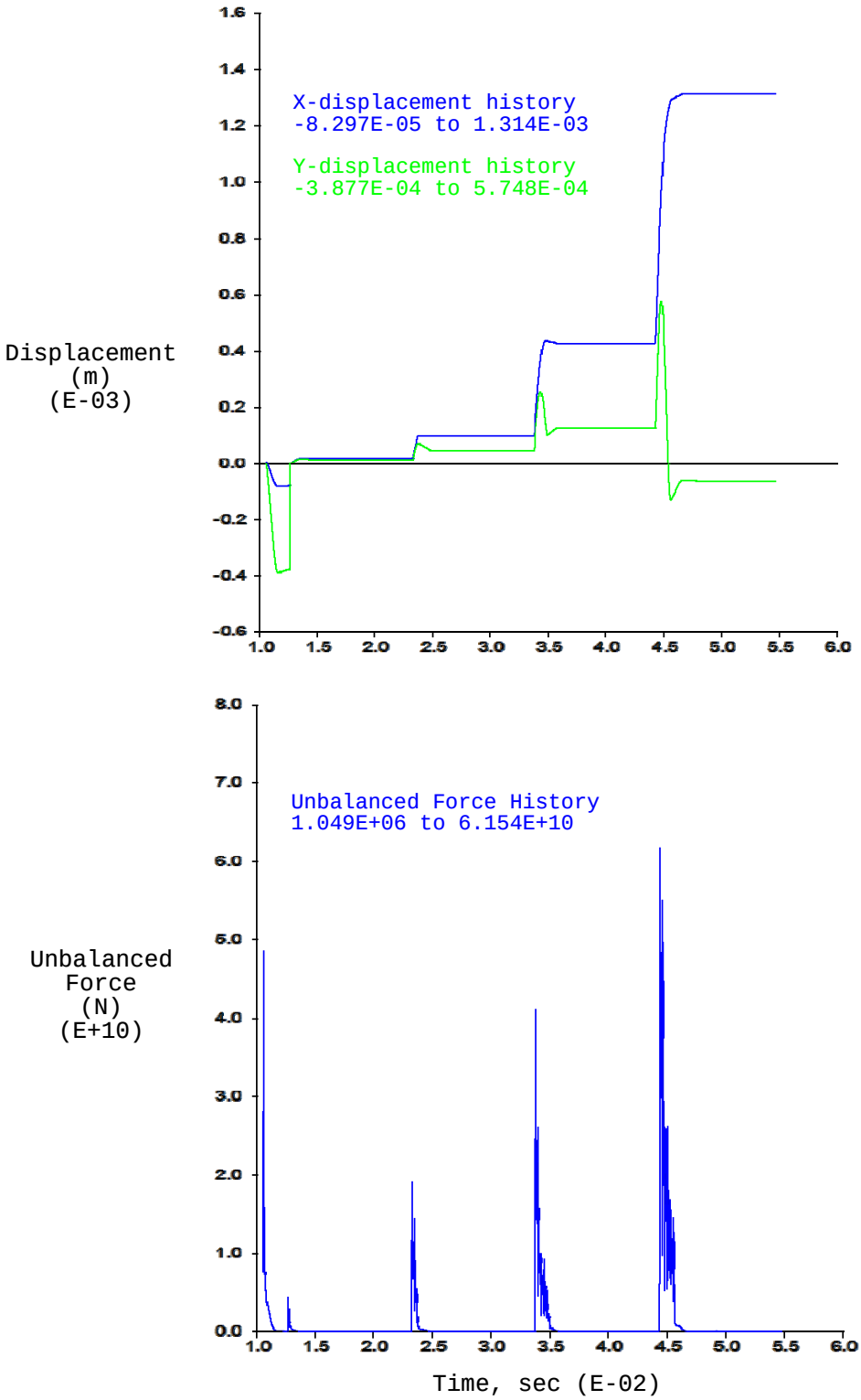

Fig. 6.21: Top: Displacement history plot of point A on sliding block vs. Time
Bottom: Unbalanced Force History plot of model vs. Time (Scenario C4)

6.3.5 – EFFECTS OF THE PEAK FRICTIONAL RESISTANCE OF THE MAIN FAULT

As mentioned in Chapter 5, a low peak friction angle, $\phi_p=25^o$, was estimated for the main fault due to the scale effects and the high effective normal stress across the fault, in connection with the Joint Compressive Strength of the fault surface. The slide initiation might be largely due to this low friction angle. To investigate the effects of the peak friction angle of the fault, a separate analysis was performed to investigate the possibility of initiation of the slide using peak friction angle, ϕ_p, based on the Barton-Bandis joint model and ignoring the fracture scaling laws. The peak friction angle, ϕ_p, used in this analysis was equal to $\phi_p=39^o$. The high peak friction angle is used in conjunction with the full pressurization of the main fault. The resulting displacement vectors had also been reversed, pointing downslope, fact which proves that even with a higher friction angle the full hydrostatic pressure in the fault is sufficient to initiate the slide.

In conclusion, hydrostatic pressure induced by the fault being full of water is sufficient to trigger sliding of the overhanging rock, as modeled in 3DEC. However, the hydrostatic pressure is not enough to cause continuous sliding of the monolithic block. This indicates that the overhanging rock mass must have disintegrated in order to slide down the slope and reach the village, as it actually occurred. The magnitude of the induced displacement is also considered large enough for application of the residual shear strength properties of the failure surfaces which will be applied at this point in time in order to proceed with the analysis.

6.3.6 – Parametric Study of the Effects of the Duration of Pore Pressure Application and Residual Shear Strength

Once the main overhanging block has begun to slide, the fault aperture is expected to increase as the fault opens up and is still moving. Consequently, the hydrostatic pressure in the fault is expected to dissipate and eventually become zero as the falling block is detached from the surface of the scarp. However, in order to create a realistic model of the slide initiation, dissipation of pore pressures after certain amount of movement must be taken into account. In 3DEC, this could be simulated by releasing the pore pressures in the fault after a certain fault normal displacement has been reached of after a number of calculation steps have been performed following initiation of the slide. The displacement history plot indicates that the block is moving, which is expected since it is still subjected to the hydrostatic pressure that initially caused it to slide. Strictly, this type of analysis will require full coupling between the mechanical response and hydraulic behavior of the fault since mechanical response depends on the hydraulic pressure condition of the fault and vice versa. However, such analysis is extremely complicated and beyond the current capabilities of 3DEC. Therefore, in order to get realistic results the pore pressures must be released after a certain number of calculation steps *after* the slide has been triggered.

Therefore, in order to observe the behavior of the model based on the amount of time the maximum hydrostatic pressure is applied, a parametric study was performed. In the parametric study, the initial state of the model is assumed to be the state at Step 4, i.e. after maximum pore pressure has been applied and five thousand calculation cycles have been performed. At this point, i.e. a total of five thousand calculation cycles after first application of the maximum pore pressure, the shear strength properties are reduced to residual properties based on the fact that the maximum displacement at Step 4 was considered large enough to have initiated movement and thus application of the residual shear strength properties.

The residual shear strength properties of the failure surfaces as calculated in Chapter 5 of this report are summarized below. Properties that are not mentioned were considered to be zero for both peak and residual states.

- Main Fault:
  ϕ_r = residual friction angle = 25°
  JKN = joint normal stiffness = 1GPa
  JKS = joint shear stiffness = 1GPa

- Vertical Shear Failure Surface:
  ϕ_r = residual friction angle = 33°
  c = cohesion = 0 MPa
  σ_t = tensile strength = 0 MPa
  JKN = joint normal stiffness = 1GPa
  JKS = joint shear stiffness = 1GPa

- Side Fault and Left and Right Valley surfaces:
  ϕ_r = residual friction angle = 30°
  JKN = joint normal stiffness = 1GPa
  JKS = joint shear stiffness = 1GPa

Simulations are performed using different amounts of time the main fault is kept under full hydrostatic pressure. The purpose of the parametric study is to understand the effect of the time period the pore pressure is applied to the model on the total displacement of the overhanging rock. The event diagram for this parametric study (Fig. 6.21) provides a graphical representation of the parametric study and the steps followed.

As shown on the event diagram of the parametric study (Fig. 6.21), the initial scenario on which the study is based is scenario C4, which corresponds to the state of the model five thousand calculation cycles after application of the maximum hydrostatic pressure. At that point, the shear strength properties of the failure surfaces were reduced to residual, as mentioned above. The number of calculation cycles allowed after reduction of the shear strength properties is varied and eight different scenarios are created. The pore pressure in the main fault is then reduced to zero, simulating the effect of dissipation of pore pressures in the field after certain displacement of the fault opening has been reached. After the fault pressure has been reduced to zero, further cycling is carried out until a steady state solution is achieved.

The pressurization study results provide input regarding the time at which the fault should be depressurized, or, in other words, the opening of the fault that is sufficient to cause complete dissipation of the pore pressures in the fault. In reality the pore pressures in the fault will dissipate gradually as the opening of the fault increases, but as mentioned, this would require a fully-coupled analysis, which is beyond the scope of the current study. Thus, it has been assumed that the hydrostatic pressure in the fault dissipates instantly after a certain fault opening has occurred.

As shown in the event diagram (Fig. 6.21) eight different scenarios were studied, named Scenario D1 through D8. In each scenario, the shear strength properties were reduced to residual, a variable number of calculation cycles performed, pore pressures reduced to zero and finally another five thousand calculation cycles performed until the model reached equilibrium. Therefore, the total number of calculation cycles performed while the model was under maximum hydrostatic pressure is calculated as follows:

Total Cycles with Max. Pressure = 5,000 cycles + X cycles with residual properties

The number of cycles performed in each of the eight scenarios while the model was subjected to pressure and after material properties reduced to residual is shown in Table 6.1. Note that Scenario D8 is an extreme scenario during which the pore pressure in the fault was applied for 105,000 cycles in total, inducing a maximum displacement of 67 cm or 0.67 m at the instance of pore pressure dissipation. It is unreasonable to expect that pore pressures up to a maximum of 3.3 MPa would still be affecting the sliding block after the fault had opened 67 cm. Common sense suggests that the pore pressures would not be sustained at much smaller smaller fault openings of a few mm or at the most a few cm.

Table 6.1 also contains the maximum displacement at the instance the pore pressure is reduced to zero, as well as the maximum displacement once the model has reached equilibrium after the pore pressures in the fault have dissipated. Fig. 6.23 provides a graphical representation of the effect of the duration of pore pressure application on the immediate and ultimate maximum displacement experienced by the overhanging rock. The overall trend indicates a linear relationship between the duration

of pore pressure application to the maximum displacement. However, a closer look at the smaller cycle range indicates that the relationship is not exactly linear but slightly curved (Fig. 6.24). A power trendline can be fit to the first part of the data with a relatively good fit of R^2=97% (Fig. 6.24).

The results of the study proved that the longer the hydrostatic pressure was applied in the fault, the larger the total maximum displacement once equilibrium was reached after pore pressure dissipation. Also, it must be noted that the intact block representing the overhanging rock did not slide much further after the pore pressures in the fault were allowed to dissipate. Thus, a sustained pressure is needed in order to continuously move the detached block as an intact material. However, as noted above, such sustained pressure is not realistic. This implies that the block must have disintegrated into smaller blocks in order to slide as far as 3 km, which it actually did. The overhanging block when modeled as an intact rigid block will only move under the application of hydraulic pressurization in the main fault and will not continue sliding on its own once pressures are released. However, this result itself is a proof that the hydraulic pressurization of the fault by a maximum pore pressure of 3.3 MPa at the base of the exposed fault surface is sufficient to initiate the slide.

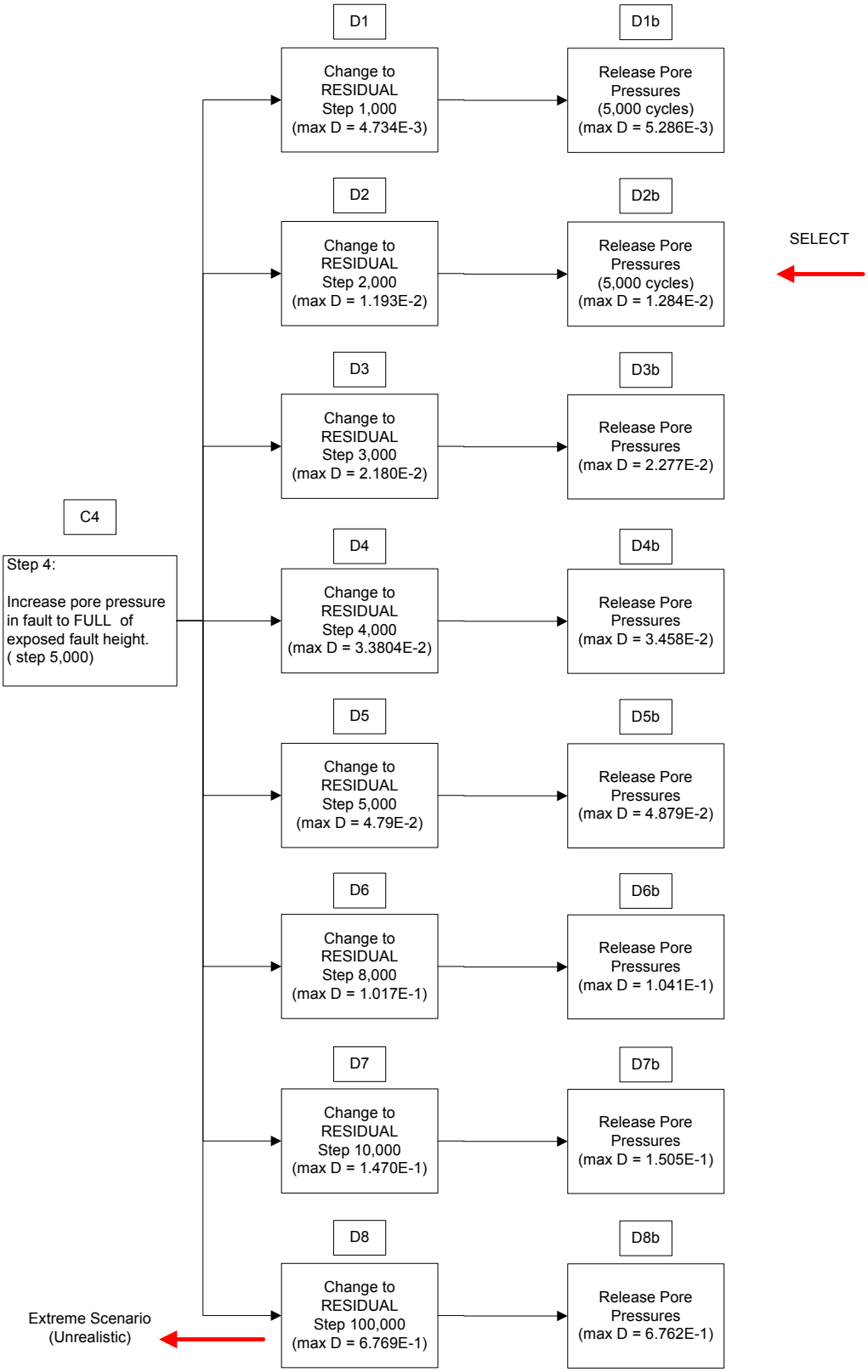

Fig. 6.22: Event diagram of parametric study on duration of pressure application

Table 6.1: Parametric Study on duration of pore pressure application scenarios and corresponding results.

Scenario #	# of Cycles performed after initial application of Max Pore pressure	# Cycles performed after properties reduced to residual	Total # of Cycles performed while model was subjected to max pore pressure	Maximum Displacement at instance of pore pressure dissipation (m)	# of Cycles performed after pore pressure dissipation	Maximum Displacement after 5,000 cycles after pore pressure dissipation (equilibrium reached) (m)
D1	5,000	1,000	6,000	4.73E-03	5,000	5.29E-03
D2	5,000	2,000	7,000	1.19E-02	5,000	1.28E-02
D3	5,000	3,000	8,000	2.18E-02	5,000	2.28E-02
D4	5,000	4,000	9,000	3.38E-02	5,000	3.46E-02
D5	5,000	5,000	10,000	4.79E-02	5,000	4.88E-02
D6	5,000	8,000	13,000	1.02E-01	5,000	1.04E-01
D7	5,000	10,000	15,000	1.47E-01	5,000	1.51E-01
D8	5,000	100,000	105,000	6.77E-01	5,000	6.76E-01

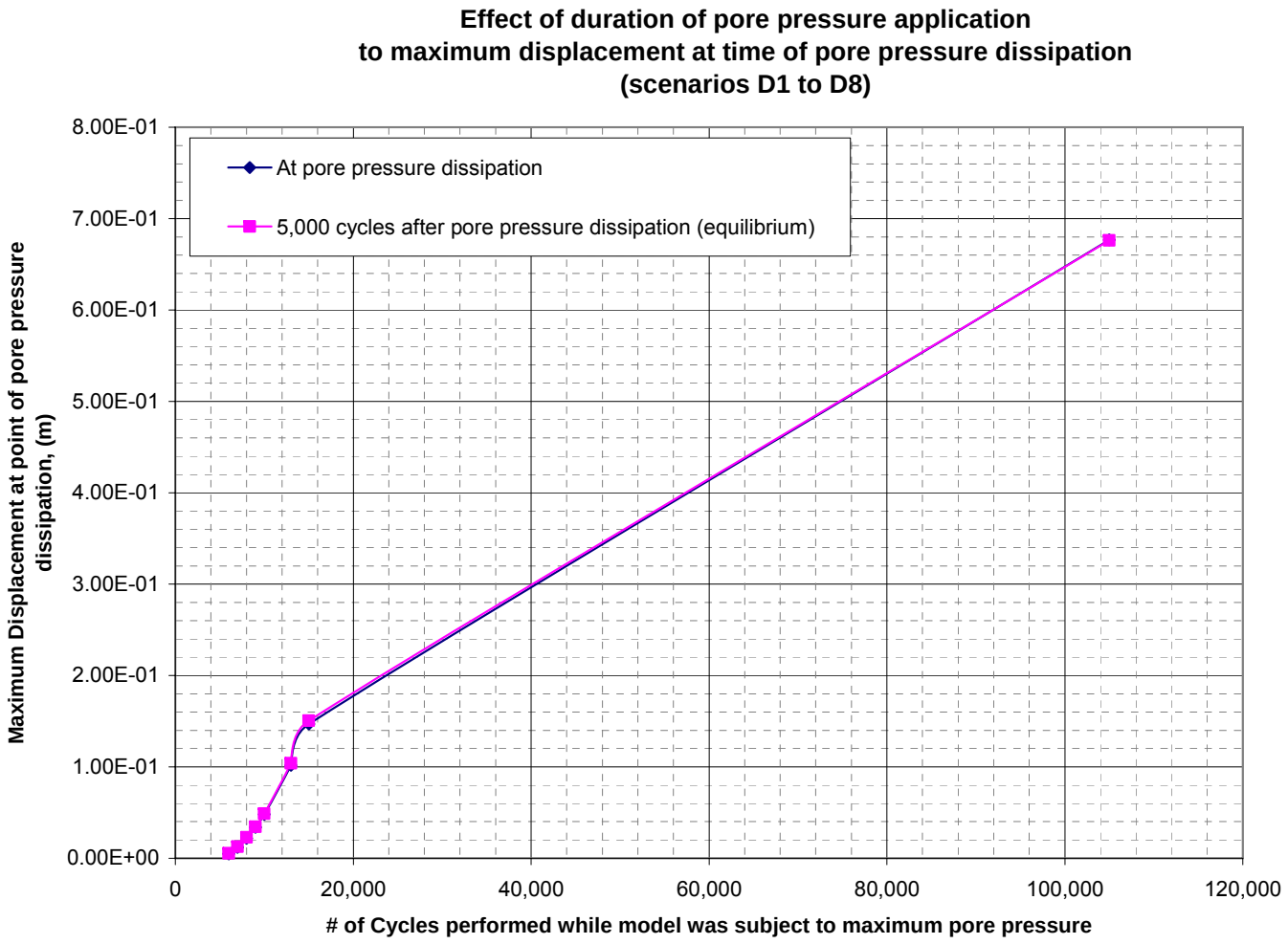

Fig. 6.23: Effect of duration of pore pressure application on maximum displacement at time of pore pressure dissipation (D1-D8)

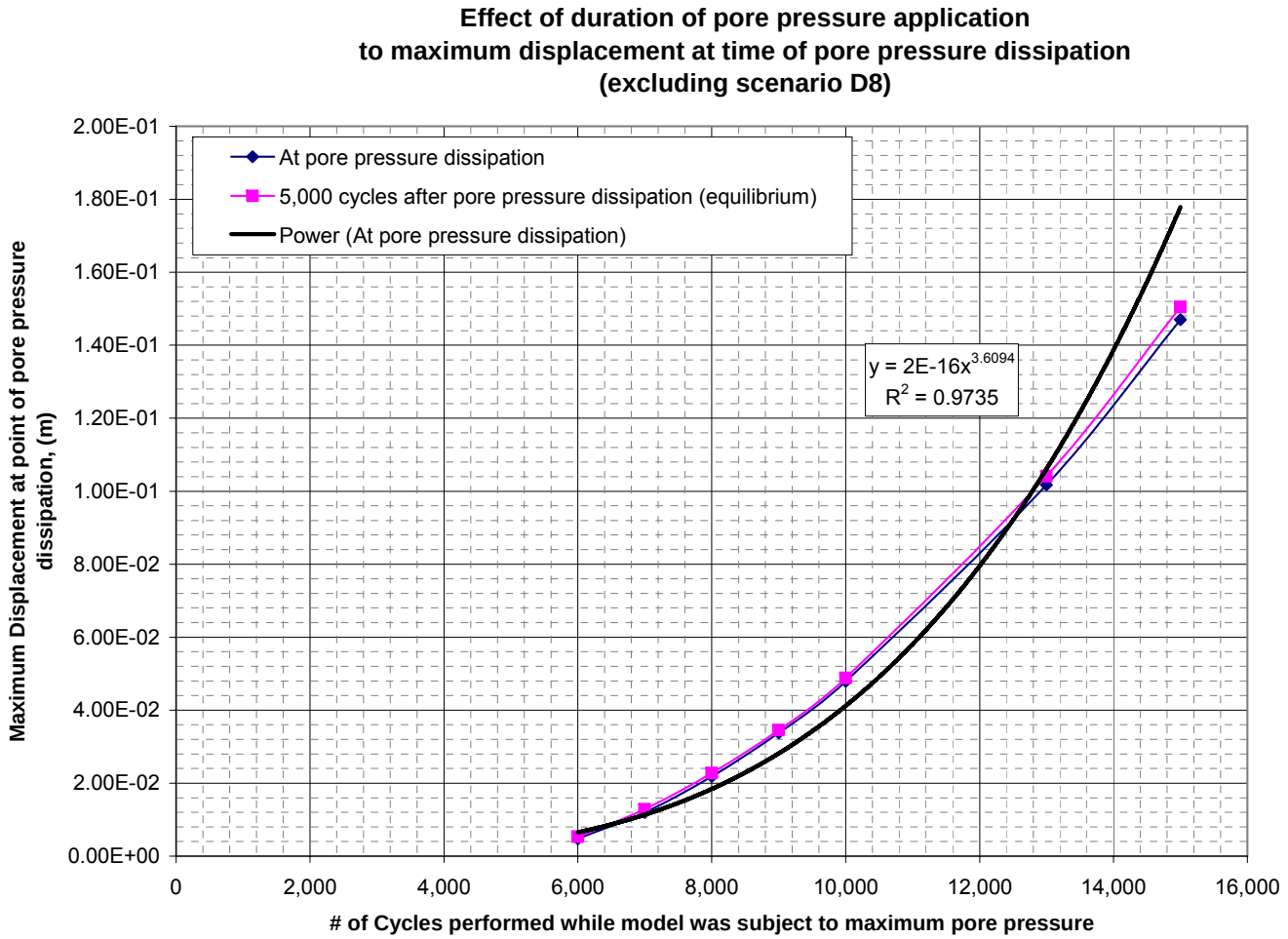

Fig. 6.24: Effect of duration of pore pressure application on maximum displacement at time of pore pressure dissipation (D1-D7)

6.3.7 – SELECTING REPRESENTATIVE SCENARIO FOR ANALYSIS

Selecting the most realistic scenario from the parametric study of the duration of pore pressure application is not an easy task. As previously mentioned, in reality the pore pressures in the fault will dissipate gradually as the opening of the fault increases. Determining the exact fault opening at which the pressure will have completely dissipated requires extensive calculations and falls outside the scope of this study. Hence, a scenario will be selected which results in the maximum, and at the same time reasonable, opening sufficient for complete pore pressure dissipation in the fault.

From the scenarios used in the depressurization parametric study, the most reasonable are D1, D2 and possibly D3. In scenario D1, the pore pressures are allowed to dissipate when the fault opening is approximately 4 mm wide. Even though theoretically this opening is relatively large compared to the initial opening of the fault and pore pressures will have most probably dissipated, a scenario which causes a slightly larger opening will be considered to be conservative. The maximum fault opening at which pore pressure dissipation is allowed in scenarios D2 and D3 is conservative enough and it can safely be assumed that the hydraulic pressure in the fault has dissipated completely. However, the opening in scenario D3, which is approximately 2.2 cm is considered relatively large. Therefore, scenario D2 will be selected as the most reasonable scenario to be used in further analyses.

According to scenario D2, maximum pore pressure is applied for five thousand cycles after which the shear strength properties of the failure surfaces are reduced to residual. The pore pressure is kept constant for another two thousand calculation cycles beyond that point resulting in a maximum displacement of 1.2 cm, or 0.012 m, at the side of the sliding block adjacent to the main fault. Once the fault has opened 1.2 cm the pore pressures in the fault are reduced to zero and another five thousand calculation cycles are performed until the system reaches equilibrium. The overhanging block stops sliding and reaches equilibrium having experienced a total maximum displacement of approximately 1.3 cm at the western face of the block adjacent to the main fault (Fig. 6.27).

The displacement vectors in Fig. 6.25 indicate that the reduction of shear strength properties in the failure surfaces from peak to residual has allowed the block to slide monolithically to a maximum displacement of 1.2 mm. The direction of the displacement vectors indicate that the block is sliding initially along the main fault and then detaches from the vertical shear failure surface on the north side of the scarp and slides downward along the two valleys at the foot of the scarp.

The displacement history plot (Fig. 6.26) indicates that the block has not reached equilibrium and is still sliding. This is expected since the monolithic block is still under the influence of the hydraulic pressure in the main fault. The maximum displacement of the block is considered large enough to cause pore pressure dissipation. Once pore pressures are allowed to dissipate the displacement vectors are still pointing downwards and the block experienced some additional movement to reach a maximum displacement of 1.3mm (Fig. 6.27). This indicates that once pore pressures have dissipated the block cannot longer slide as an intact rock mass. This is also indicated from the displacement and unbalanced force history plots in Fig. 6.28. However, the direction of the displacement vectors still supports the conclusion that the slide has been initiated and the overhanging rock mass is beginning to slide.

The fact that the block is not sliding monolithically does not inhibit the conclusion that the slide has been triggered due to full hydrostatic pressure in the fault and the block is beginning to slide initially along the main fault surface. Further analyses are required where disintegration of the overhanging rock mass is allowed to cause further sliding.

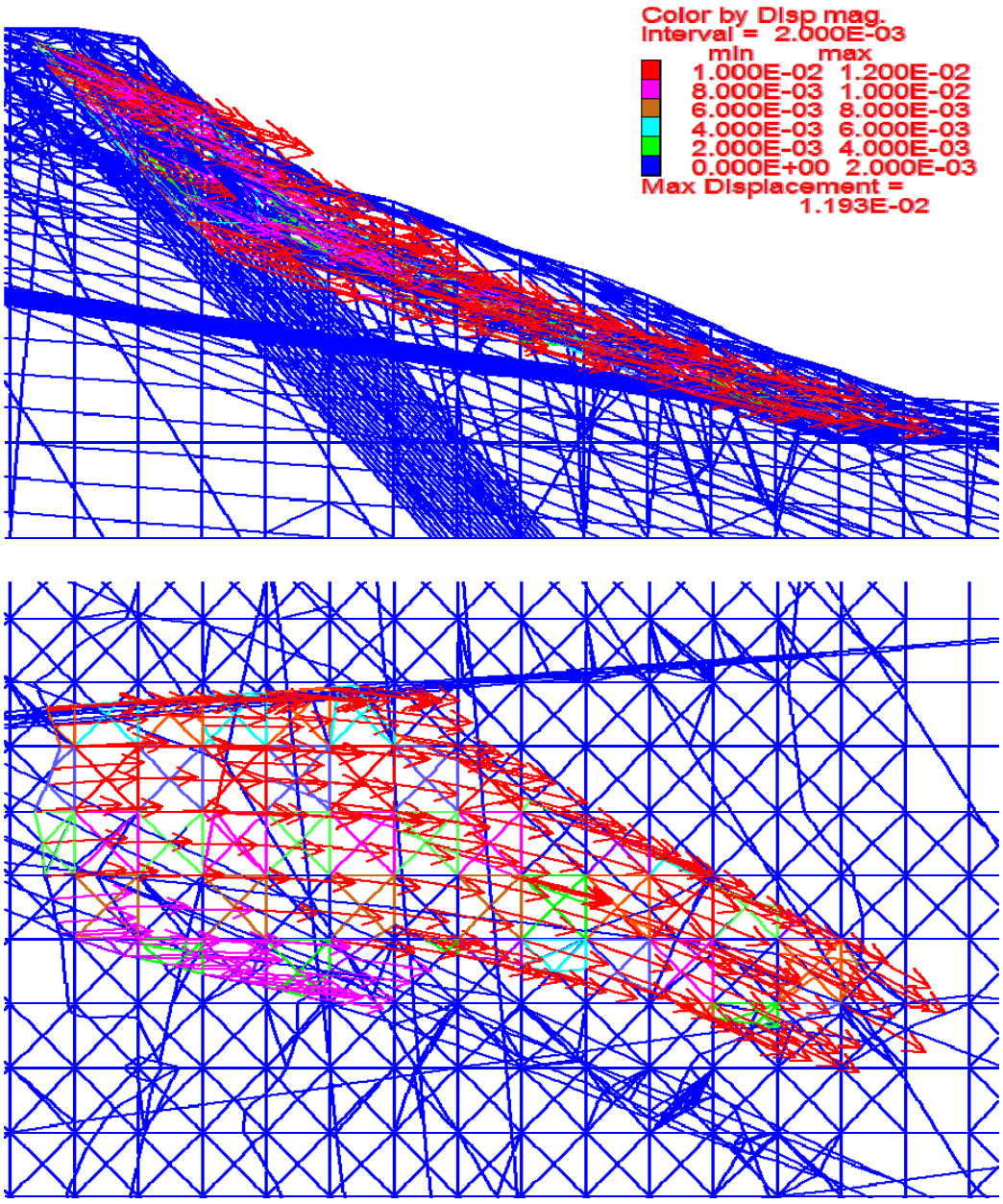

Fig. 6.25: Profile and plan view of 3DEC model showing displacement vectors of overhanging block (Scenario D2)

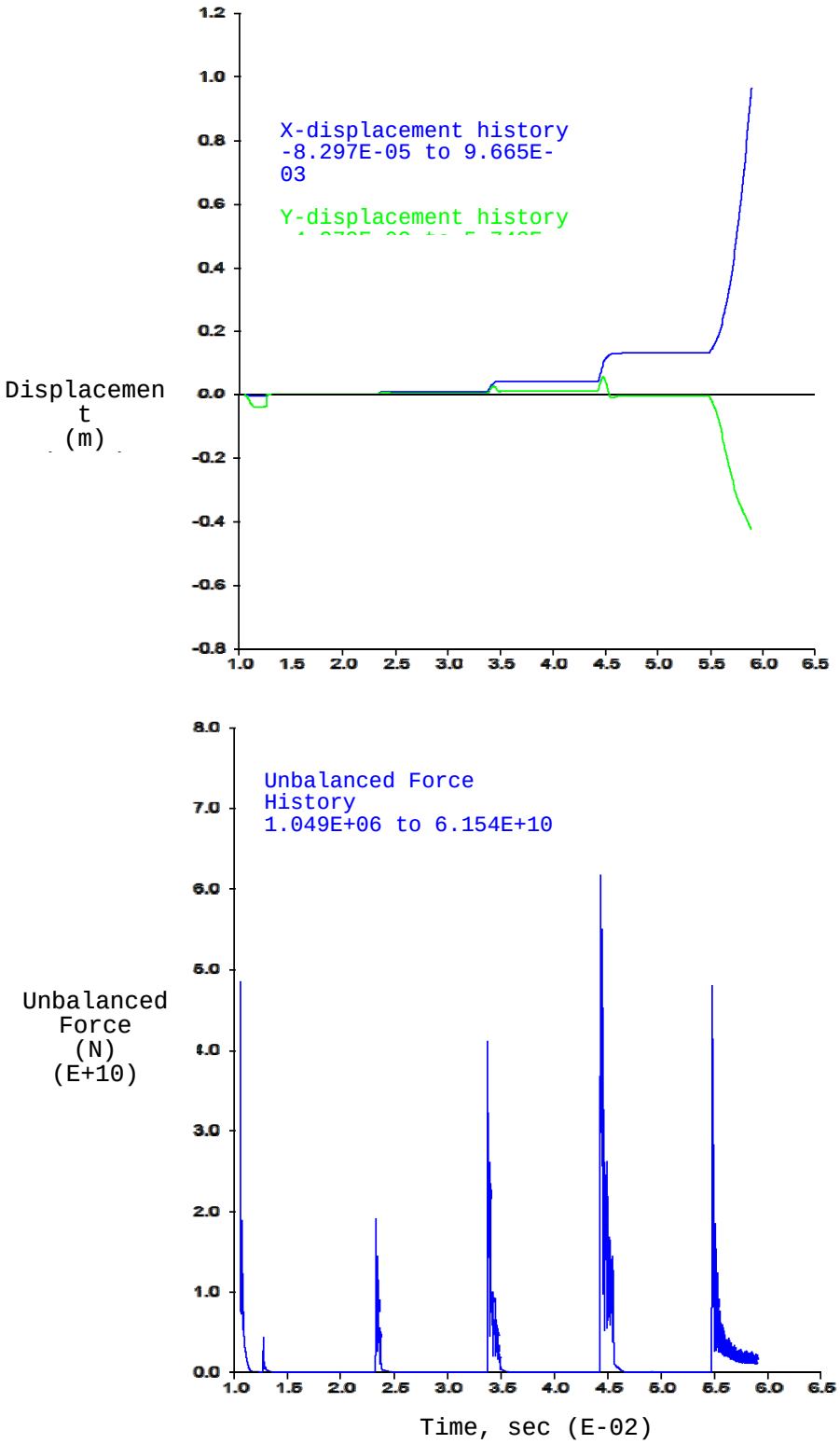

Fig. 6.26: Top: Displacement history plot of point A on sliding block vs. Time
Bottom: Unbalanced Force History plot of model vs. Time (Scenario D2)

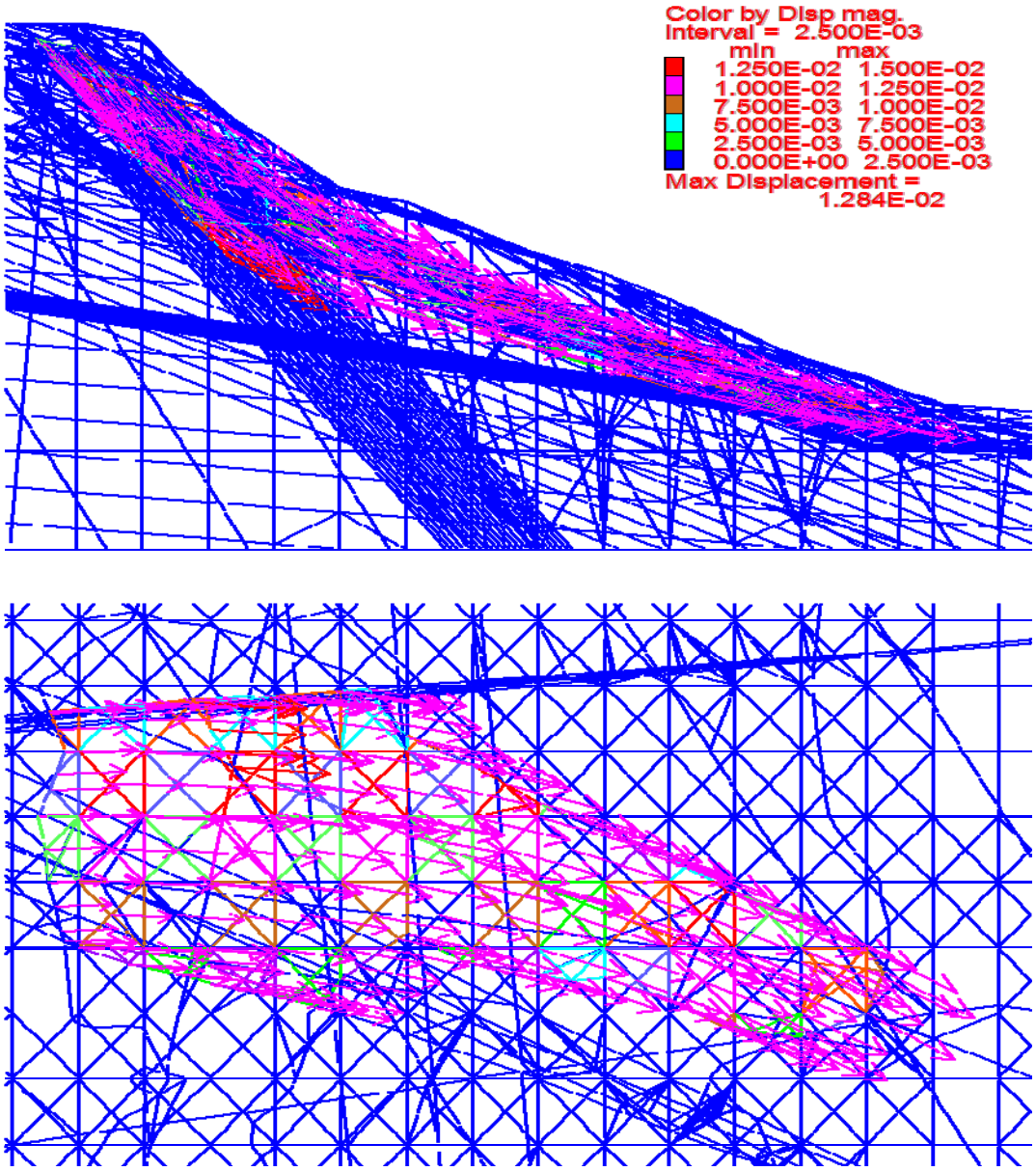

Fig. 6.27: Profile and plan view of 3DEC model showing displacement vectors of overhanging block after pore pressures released – Scenario D2b

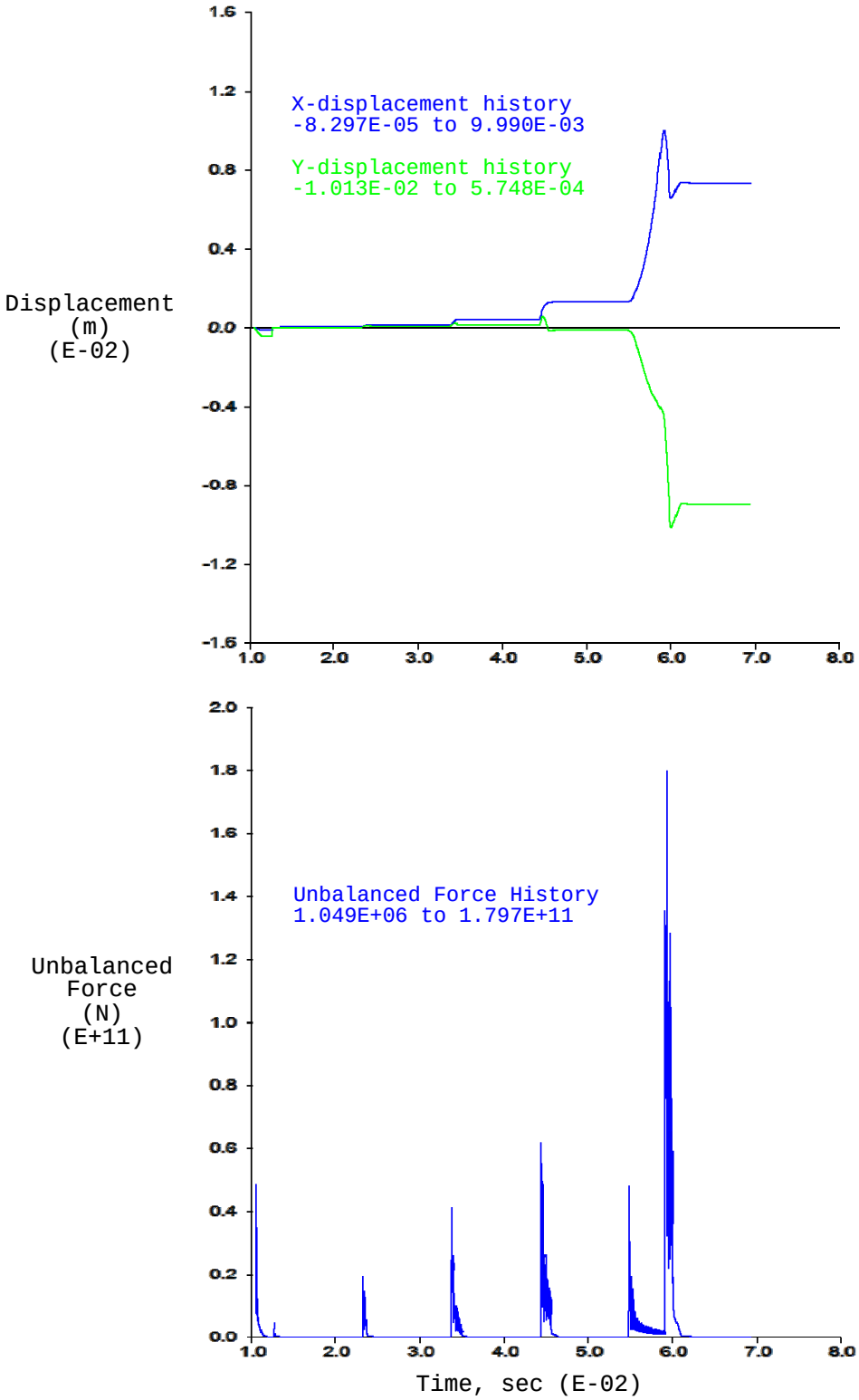

Fig. 6.28: Top: Displacement history plot of point A on sliding block vs. Time
Bottom: Unbalanced Force History plot of model vs. Time (Scenario D2-b)

6.4 – SEISMIC EFFECT ON TRIGGERING OF THE SLIDE

This part of the analysis studies the effect of the four minor earthquakes that occurred the morning of February 17th, 2006 in the area near St. Bernard town on the triggering on the slide. This part of the analysis assumes full hydraulic pressurization of the fault, as well as an intact and rigid sliding block. Three different earthquake scenarios will be considered in this study.

According to records by the Philippine Institute of Volcanology and Seismology (PHIVOLCS) the horizontal acceleration recorded for the four earthquakes that occurred the morning of the slide ranged from 67 to 100 gals (1 gal = 0.01 m/s^2 = 0.001 g). All earthquake scenarios in this study were modeled using the maximum recorded seismic horizontal acceleration of 100 gals or 0.1 g. The seismic acceleration was applied to the model in addition to the gravity applied on the increased unit weight of the block, and the linearly varying hydrostatic pressure in the main fault. The direction of the applied horizontal acceleration is parallel to the main fault along which the earthquake is believed to have been initiated.

The event diagram for the seismic analysis of the 3DEC model is shown in Fig. 6.19 and graphically presents the three earthquake scenarios that will be analyzed. The first earthquake scenario, scenario EQ1, follows scenario D2-b, which is the scenario previously selected based on the results of the depressurization parametric study described in the previous section. This scenario models the effect of the earthquake had it occurred after the slide was actually triggered by the hydraulic pressurization of the fault. After properties have been reduced to residual and pore pressures in the fault have been allowed to dissipate and the system has reached equilibrium, the earthquake is applied along the direction of the main fault. The duration the seismic horizontal acceleration was applied for 0.1 seconds real-time. This duration when converted to computational-time is equivalent to 4,750 cycles. The maximum displacement at the end of 4,750 cycles is recorded in Table 6.2 along with the results from the other two earthquake scenarios. Figures 6.20 and 6.21 present the displacement vectors and history plots for scenario EQ1.

Scenario EQ2 follows scenario C4 as shown in the event diagram. This scenario actually models the effect of the earthquake had it occurred simultaneously with the triggering of the slide due to hydraulic pressurization and caused instant dissipation of the pore pressures in the fault. Therefore, once the slide is triggered by the pore pressures in the fault, the pore pressures are released at the same time as the earthquake of 0.1 g is applied for a duration of 0.1 seconds. The maximum displacement at the end of 4,750 cycles is recorded in Table 6.2 along with the results from the other two earthquake scenarios. Figs. 6.22 and 6.23 present the displacement vectors and history plots for scenario EQ2.

The final earthquake scenario modeled in this study, scenario EQ3, follows scenario C4 directly. In this case, however, the pore pressures are not released immediately after the triggering of the slide had occurred. The 0.1 g equivalent earthquake horizontal acceleration is applied to the model for 0. 1 seconds while the pore pressures in the main fault continue to act. This is the worst-case scenario of the three considered in this study for the seismic effects on the triggering of the slide, and is expected to result in the largest displacement. The maximum displacement at the end of 4,750 cycles is recorded in Table 6.2 along with the results from the other two earthquake scenarios. Figs. 6.24 and 6.25 present the displacement vectors and history plots for scenario EQ3.

Table 6.2: Block displacements before and after earthquake application

Earthquake Scenario #	Maximum Displacement PRIOR to application of 0.1g equivalent earthquake (m)	Maximum Displacement AFTER application of 0.1g equivalent earthquake (m)
EQ1	1.28E-02	1.28E-02
EQ2	1.5E-03	1.21E-03
EQ3	1.5E-03	1.87E-03

By comparing the change in maximum displacement prior to and after application of the 0.1g equivalent earthquake to the system, it appears that the earthquake had little or no effect to the triggering of the slide. The maximum displacement after the

application of the horizontal seismic acceleration for a duration of 0.1 seconds varies insignificantly from the maximum displacement of the falling block prior to application of the equivalent earthquake (Table 6.2). Therefore it can safely be concluded that the earthquake had an insignificant effect on the triggering of the slide and that the hydraulic pressurization of the fault is the main triggering mechanism of the Guinsaugon rockslide.

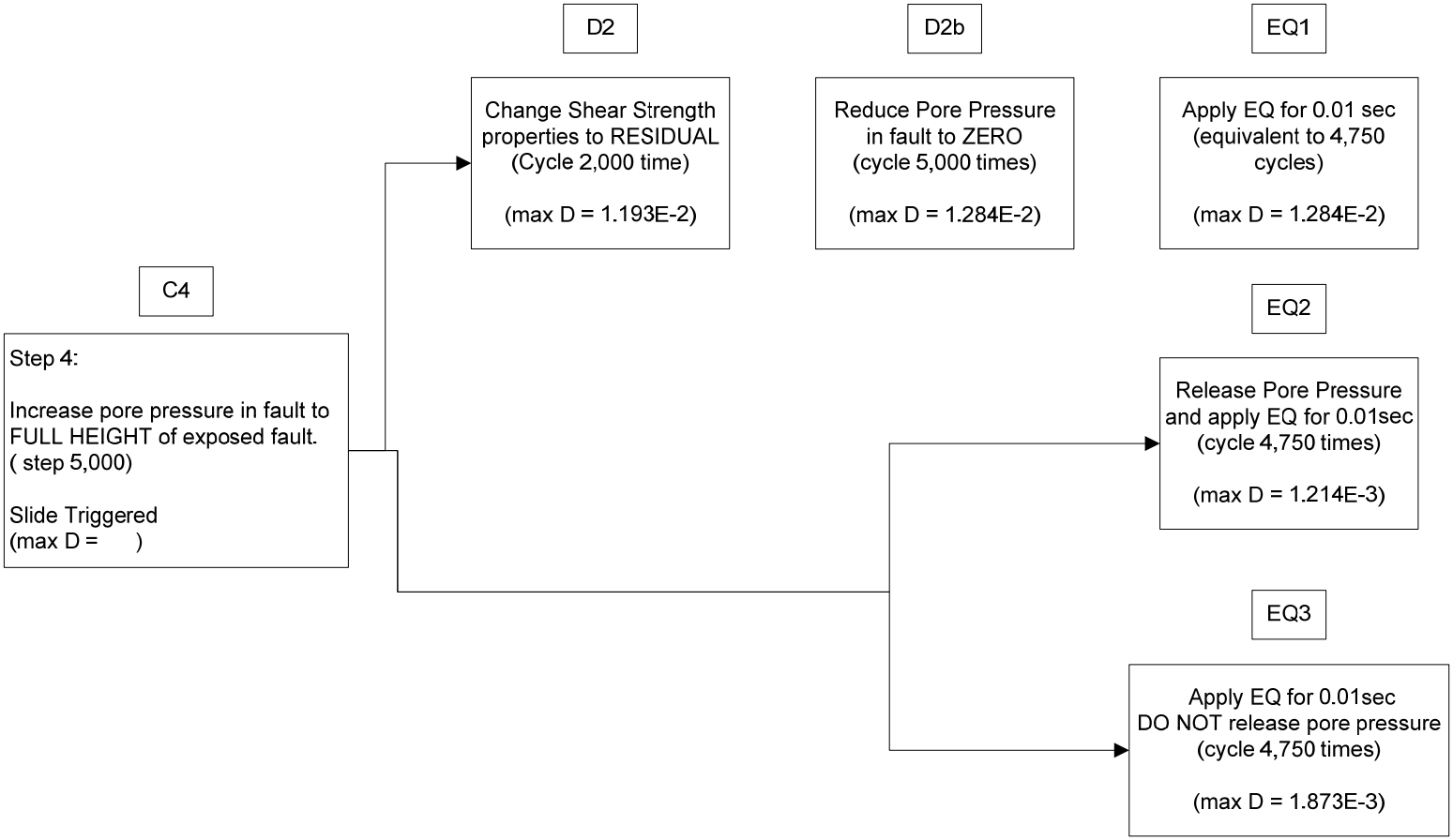

Fig. 6.29: Event diagram of seismic analysis

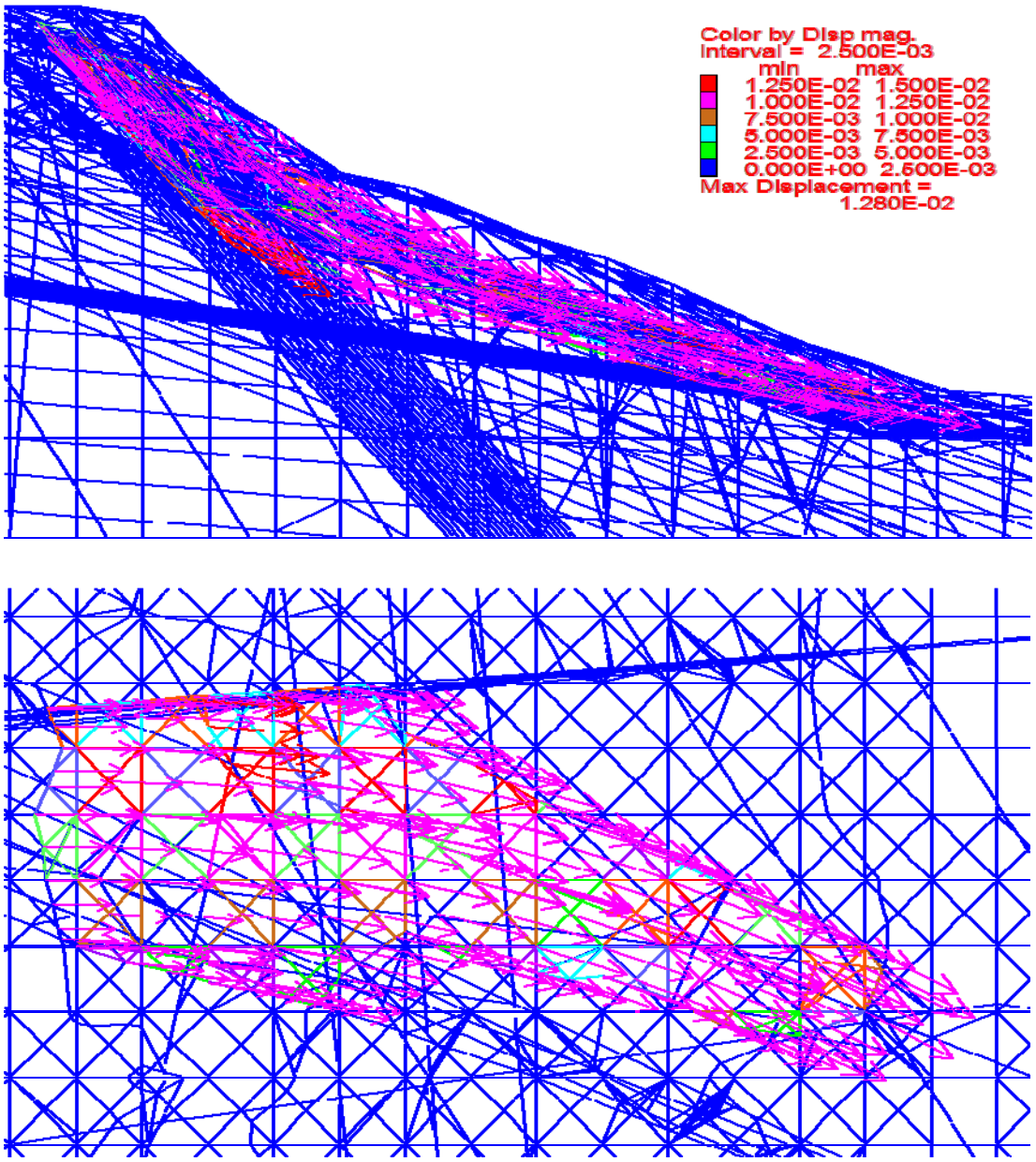

Fig. 6.30: Profile and plan view of 3DEC model showing displacement vectors of overhanging block – Scenario EQ1

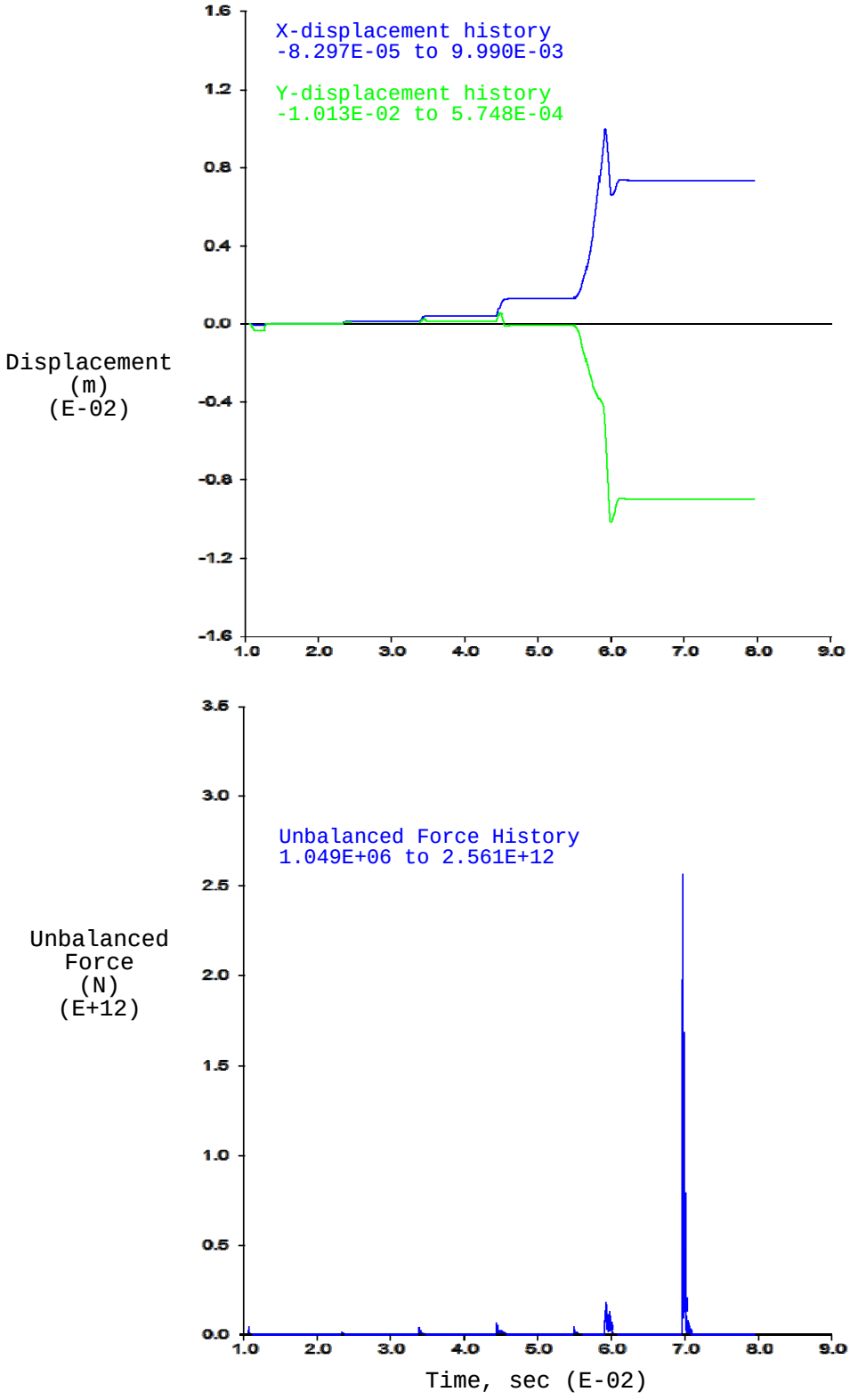

Fig. 6.31: Top: Displacement history plot of point A on sliding block vs. Time
Bottom: Unbalanced Force History plot of model vs. Time (EQ1)

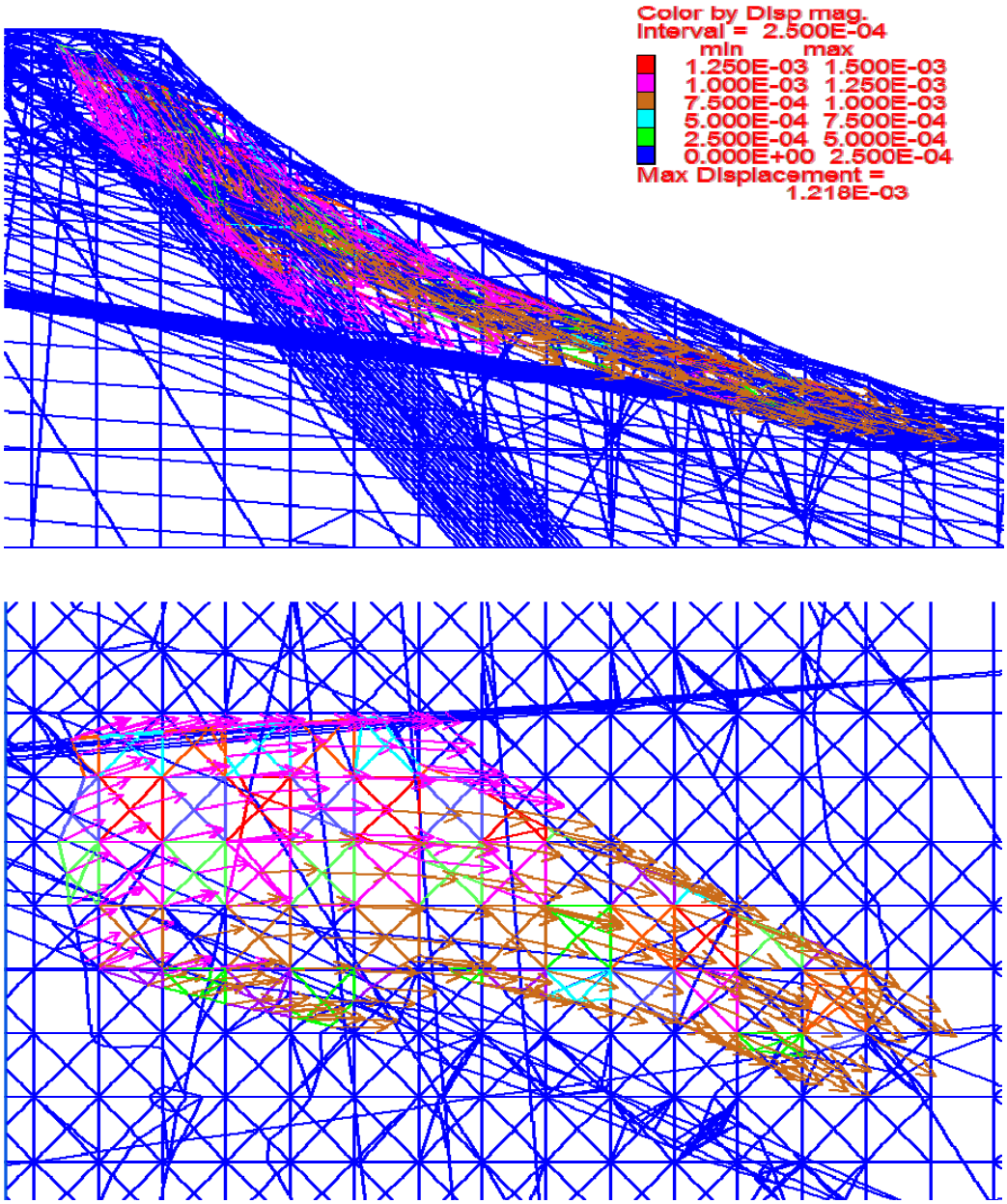

Fig. 6.32: Profile and plan view of 3DEC model showing displacement vectors of overhanging block – Scenario EQ2

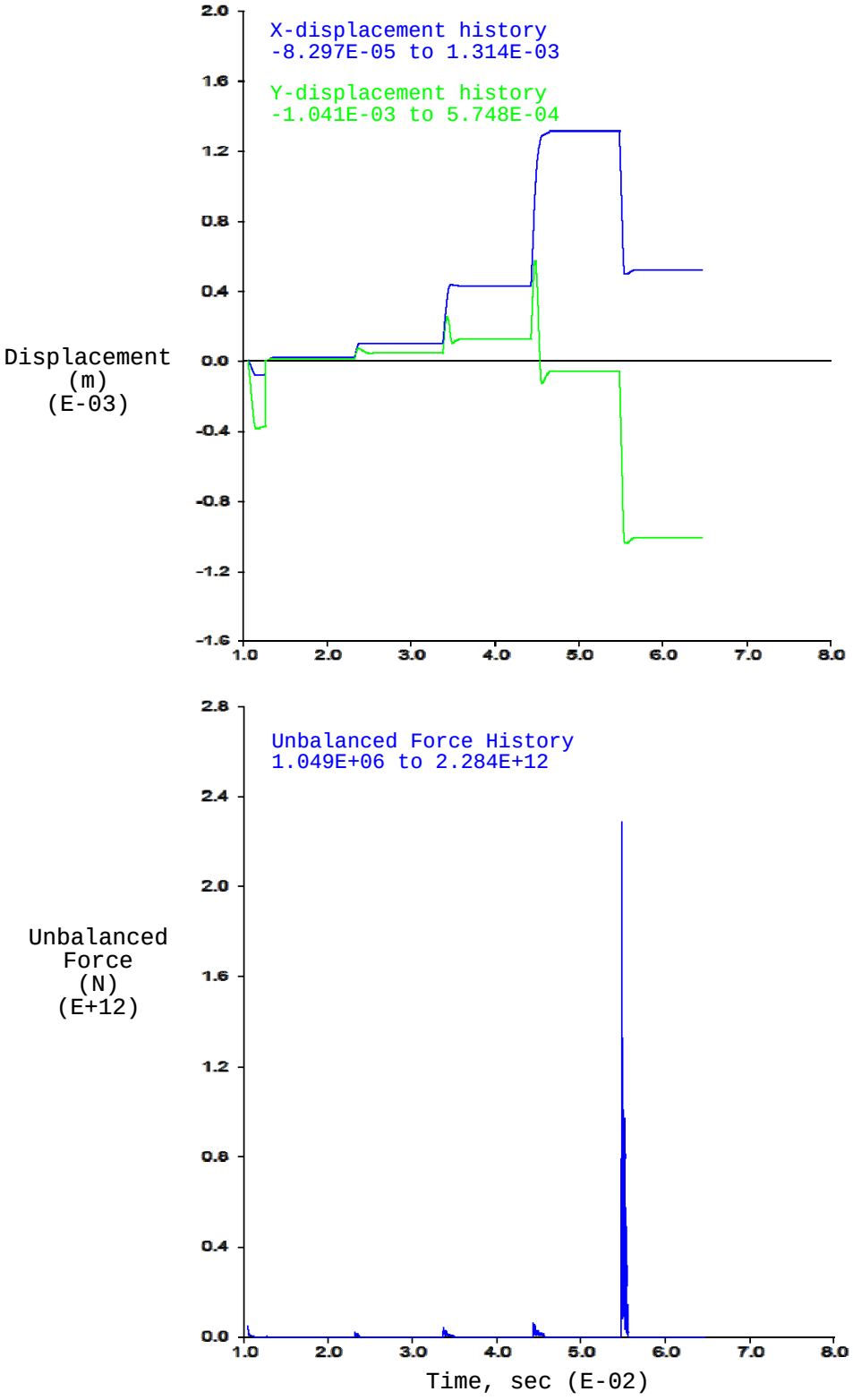

Fig. 6.33: Top: Displacement history plot of point A on sliding block vs. Time
Bottom: Unbalanced Force History plot of model vs. Time (EQ2)

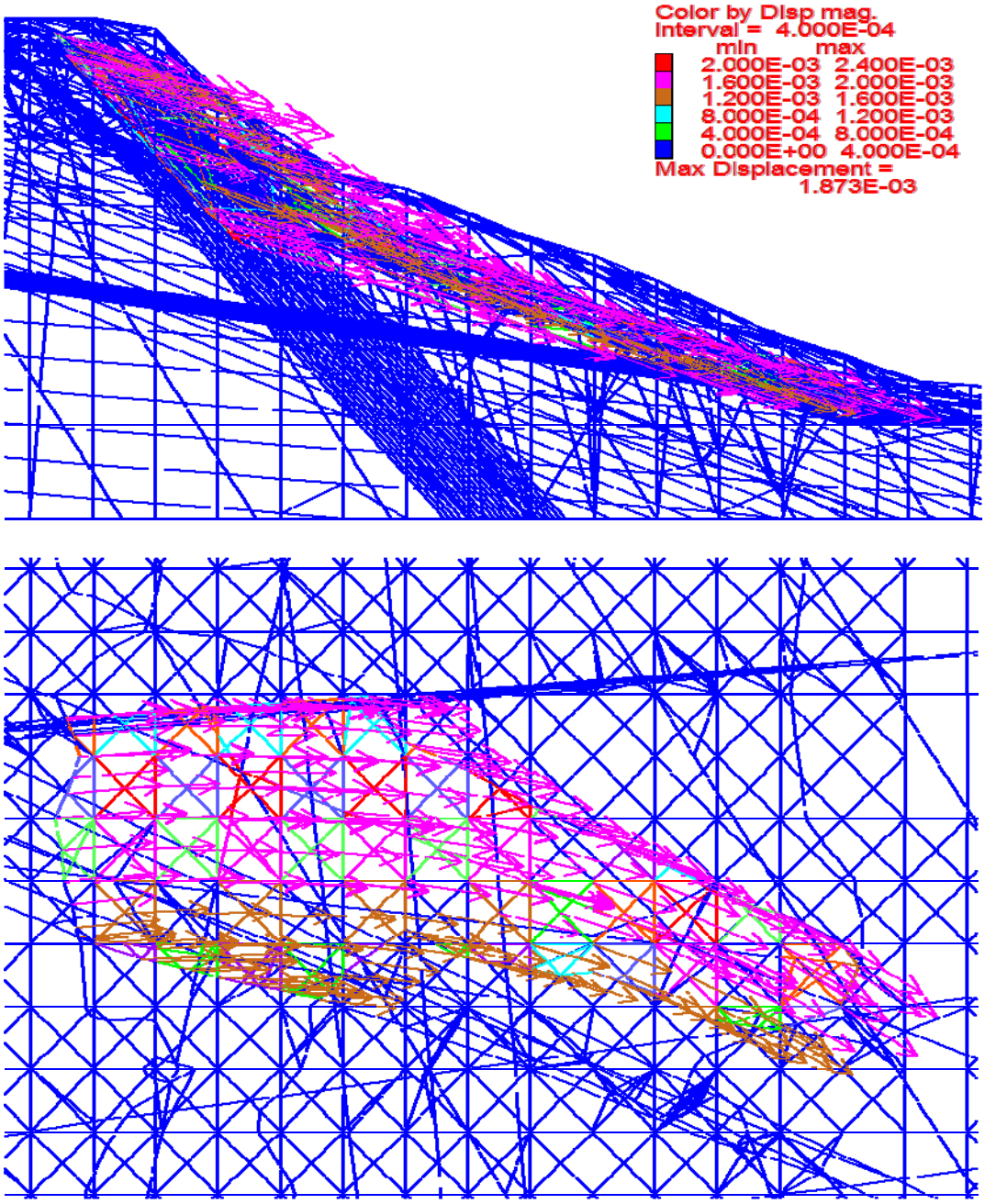

Fig. 6.34: Profile and plan view of 3DEC model showing displacement vectors of overhanging block – Scenario EQ3

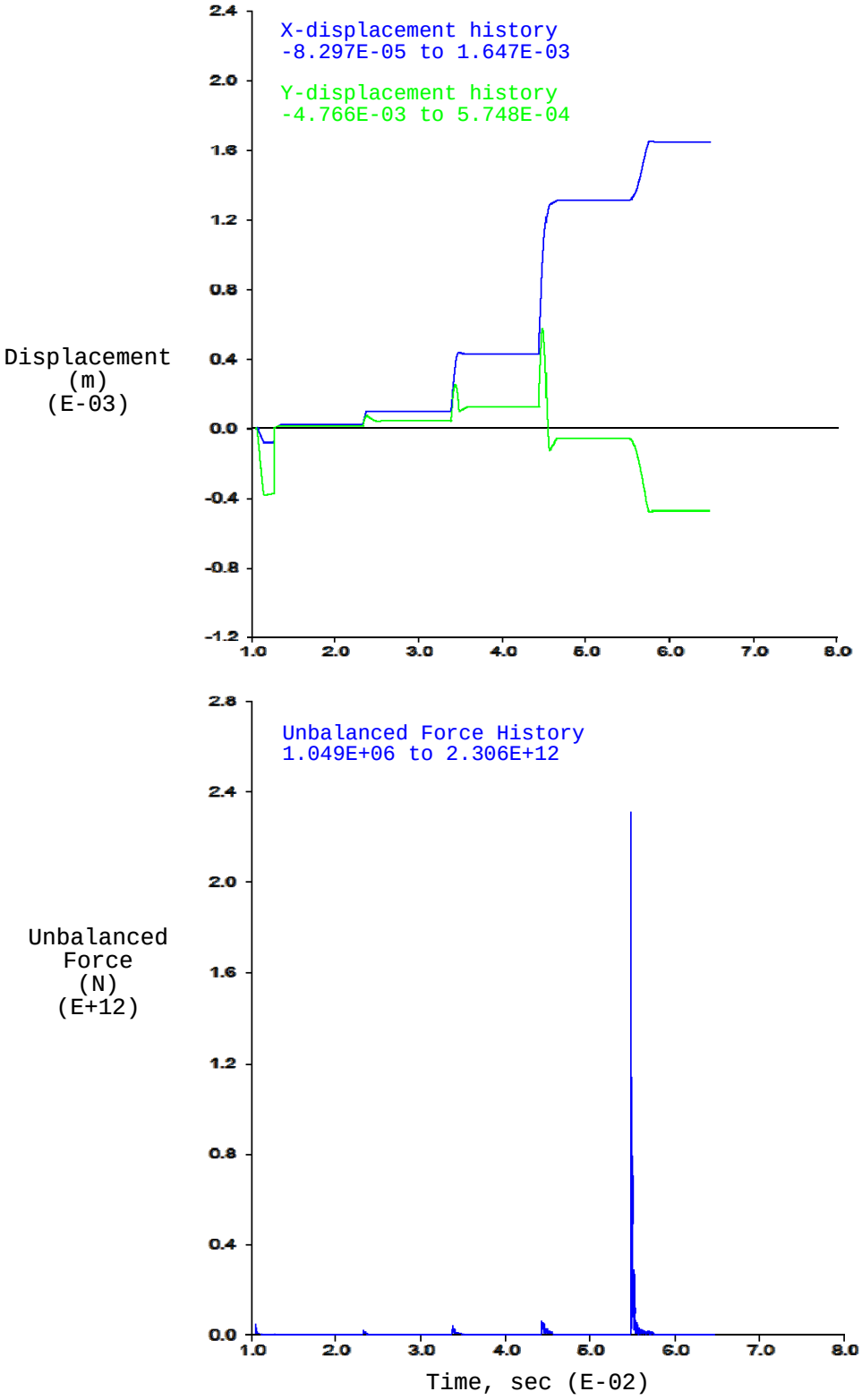

Fig. 6.35: Top: Displacement history plot of point A on sliding block vs. Time
Bottom: Unbalanced Force History plot of model vs. Time (EQ3)

CHAPTER 7: DEBRIS FLOW SIMULATION

7.1 – GENERAL

The second objective of the distinct element simulations of the February 17th, 2006, Leyte, Philippines rockslide is to model the subsequent flow of the debris material following the triggering of the slide. In this analysis, the overhanging rock is subdivided in smaller blocks by introducing several fracture sets representing the natural fractures in the rock. The introduced rock fractures allow the block to disintegrate into smaller pieces due to failure along natural discontinuities.

The U.S. reconnaissance team performed a digital photogrammetry survey of the vertical shear failure surface, which forms one of the scarp surfaces, as well as data logging for field rock mass classification of rock exposures. The survey resulted in identification of three fracture sets from rock exposures. The first fracture set is parallel to the main fault, the second is parallel to the vertical shear failure surface, and the third is perpendicular to the main fault. Data collected about the fracture orientation, length, spacing, persistence and fracture surface characteristics was used in generating the fracture patterns in the falling block. Due to limitations in computational resources, the smallest fracture spacing that could be used, in order to obtain results in a reasonable amount of time, was 25 m. However, the actual fracture spacing in the field was estimated to be less than 1 m, and the largest blocks of rock found among the debris materials has a size of 3 m, but such small spacing was impossible to simulate in the debris flow analysis.

The orientation of each of the fracture sets used in the debris flow simulation model is shown in Figs. 7.1 through 7.3. The orientation of each fracture set is:

- Fractures parallel to main fault:
  - Dip = 48^{o}
  - Dip Direction = 85^{o}
- Fractures perpendicular to main fault:
  - Dip = 48^{o}
  - Dip Direction = 265^{o}

- Fractures parallel to vertical shear failure surface:

  Dip = 88^{o}

  Dip Direction = 175^{o}

Similar to the model used in analysis of the triggering mechanism, the fractured model was also subjected to in-situ stresses, gravity, increased block unit weight and full hydraulic pressurization of the main fault. The seismic horizontal acceleration was not applied since it was shown that it did not have any significant effect in the triggering of the slide.

The objective of the debris flow simulation was to gain an understanding of the behavior of the debris flow once it has been initiated. The distinct element analysis of the debris flow included in this chapter does not examine the conditions under which the debris flow was initiated, but rather the behavior of the debris flow once it was initiated.

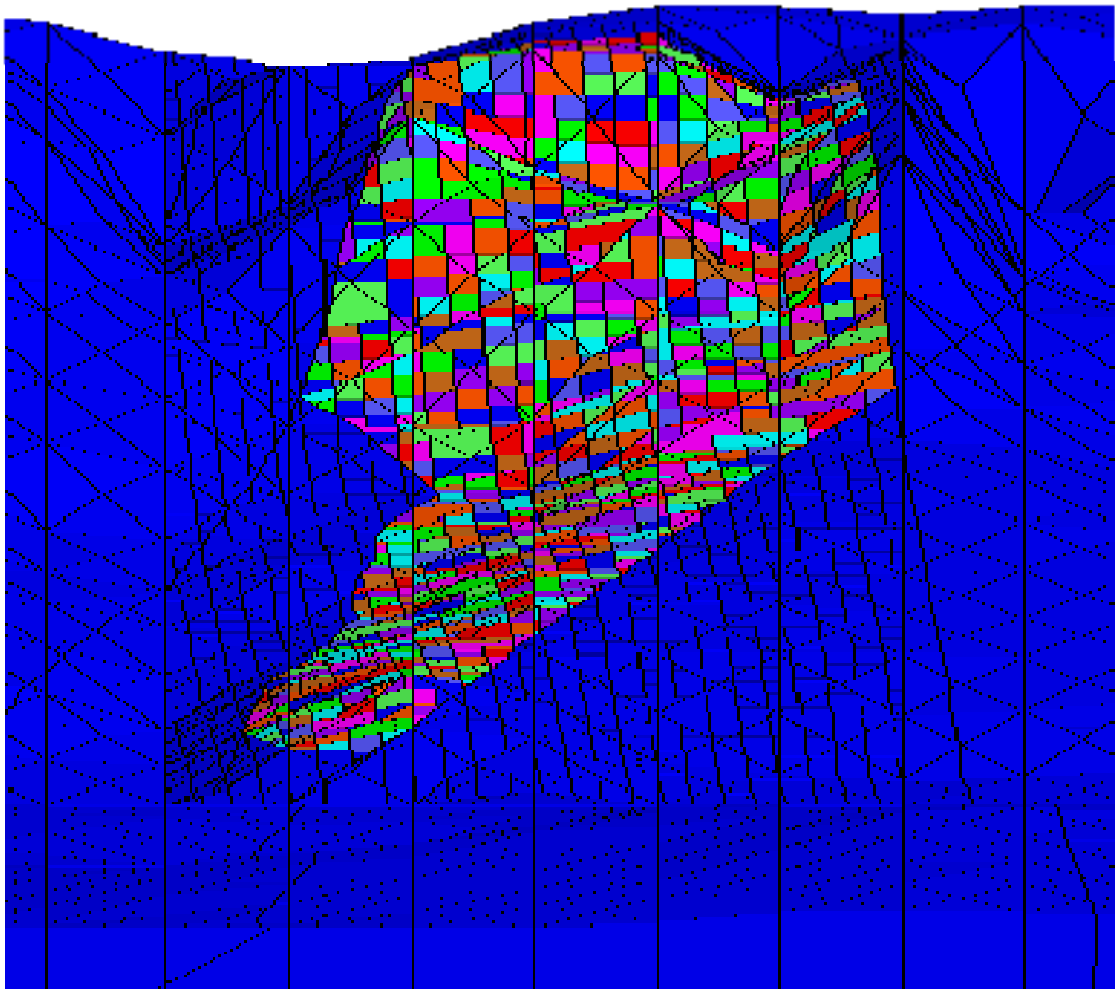

Fig. 7.1 - Front view of the fractured falling block showing the three joint sets.

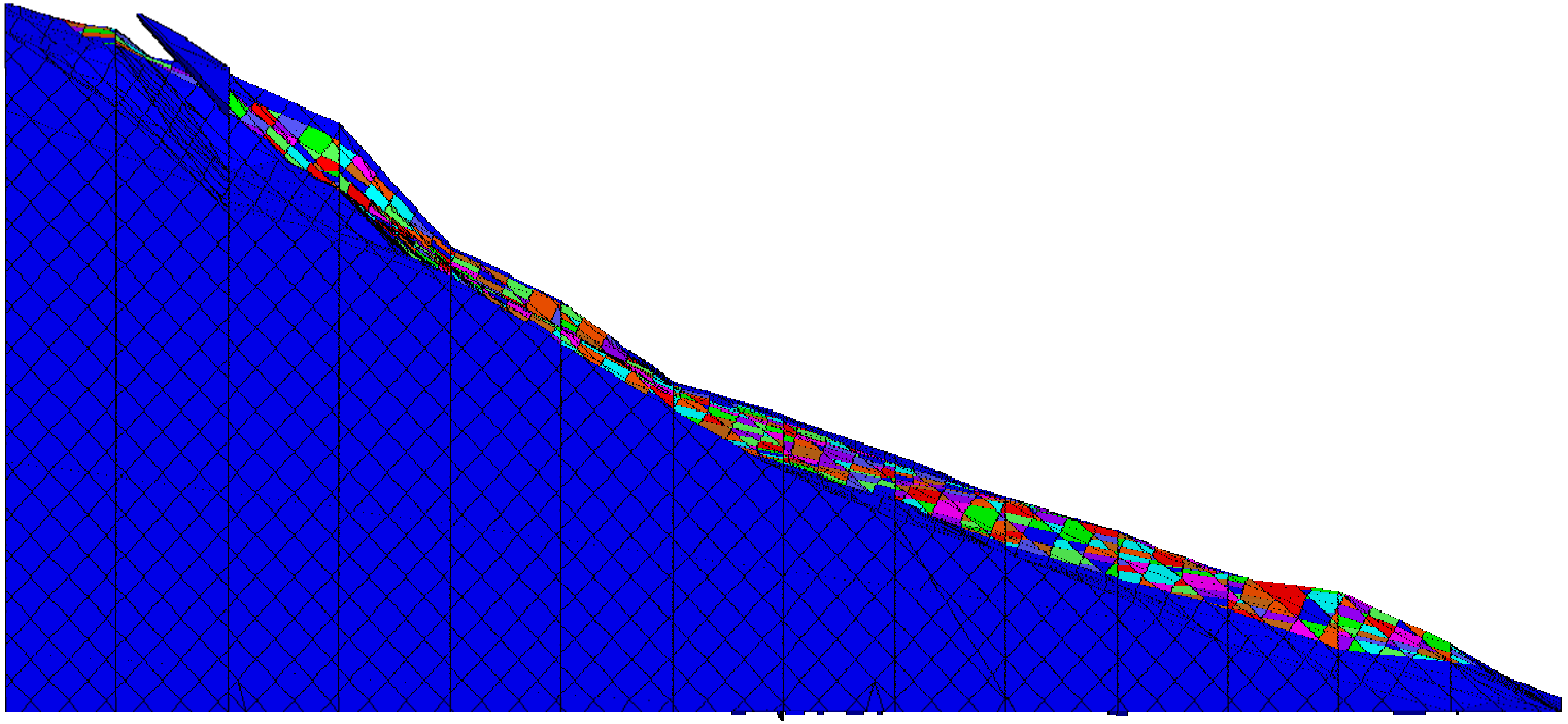

Fig. 7.2 - Side view of the fractured section of the model showing orientation of the joint sets parallel and perpendicular to the main fault surface

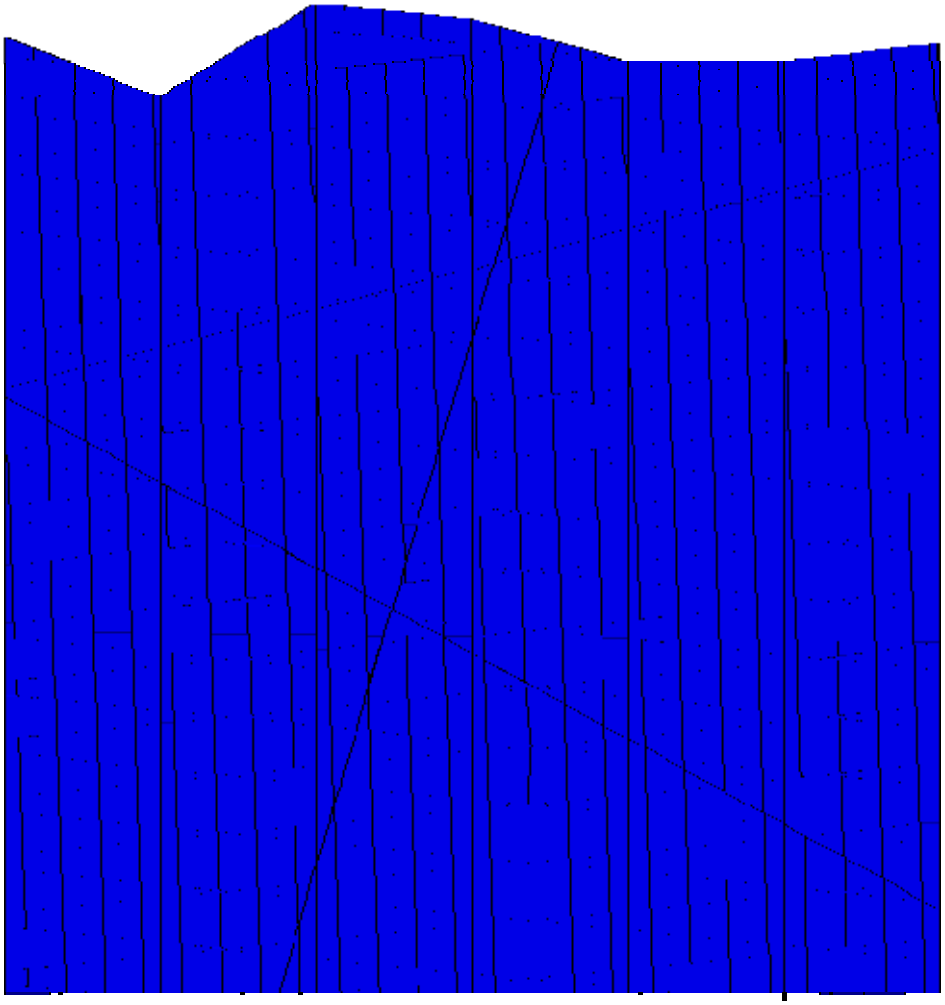

Fig. 7.3 - View from the back side of the fractured section of the model showing the joint set parallel to the vertical shear failure surface.

7.2 – SHEAR STRENGTH PROPERTIES

For this part of the analysis, the peak shear strength properties of the failure surfaces were kept the same as in the triggering analysis where the block was intact. However, determining the residual shear strength properties of the failure surfaces and the joint sets in the falling block was not a simple task. Due to the dynamic nature of the debris flow itself, determination of the residual shear strength properties would require back-analysis taking into account dynamic loading. The back-analysis would be performed to determine the highest residual shear strength properties of the failure surfaces and joints that would cause the debris flow to initiate. However, such analysis was not performed as part of this project since the initiation of the debris flow was not included in the scope of work for this project.

The residual shear strength properties of the failure surfaces and the joint sets in the actual overhanging rock mass were assumed to be $\phi_r = 0°$ in order to expedite the disintegration process and observe the behavior once the debris flow was initiated. As previously mentioned, in order to determine the actual friction angle that would cause the debris flow, a parametric analysis should have been performed. Ultimately, the purpose of parametric study would be to obtain the highest friction angle that could be assigned to the faults, joints and fractures that would initiate disintegration of the overhanging rock mass. However, the purpose of this analysis was only to study the behavior of the debris flow and not the circumstances under which it was initiated.

The actual residual friction angle of the joints and fractures involved in the debris flow is expected to be very low, much lower than the residual friction angle used in the analysis of the triggering mechanism. The use of $\phi_r = 0°$ as the residual friction angle can be supported by the results reported in Tamaoki (2006). The residual friction angle of the slide materials measured and reported by Tamaoki (2006) was $\phi_r = 2°$ which suggests that a very low friction angle is expected. Additionally, the dynamic loading, which was not modeled in this case, would also greatly clarify the use of a very low effective residual friction angle for the contacts. Therefore, the use of $\phi_r = 0°$ as the residual friction angle in modeling the debris flow is not unlikely and will ensure that the debris flow initiates, such that its behavior can be analyzed.

7.3 – OBSERVATIONS AND RESULTS

The debris flow simulations were challenging in terms of computational resources and time, due to the great detail and small fracture spacing required. Due to time limitations the debris flow simulations were not performed to full the extent of expected flow of the material. However, the simulations performed were sufficient to provide a good understanding of the behavior of the disintegrated rock mass once the slide was triggered.

The results of the debris flow simulations are shown in Figs. 7.4 through 7.12 showing the disintegration of the detached rock mass into smaller blocks and the movement of the debris with time. The results indicate that the part of the rock mass at the top of the scarp was the first part of the block to disintegrate into smaller blocks (Fig. 7.5). The bottom part disintegrated shortly thereafter as shown in the sequence of results in Figs. 7.5 to 7.12.

Careful examination of the disintegrating block at early stages of disintegration shows that the rock tended to break more along the horizontal planes (Fig. 7.4) rather than along the vertical fracture sets. Also, the block appears to break into several large sections prior to completely disintegrating in to smaller block, which supports witness accounts that the falling rock mass initially separated into large blocks prior to sliding further down the slope. This effect is more evident in Figs. 7.5 and 7.6.

Once completely disintegrated, the individual blocks at the top of the scarp began sliding downward along the dip direction of the main fault surface. This movement caused the rest of the blocks to bulge upward and eventually begin sliding along the two 'valley' surfaces at the bottom of the scarp. The main flow direction of the debris appears to be parallel to the 'valley' created at the bottom of the scarp. However, some disintegrated blocks tend to spread and flow over the scarp edges (Fig. 7.10b).

The displacement vectors at two separate instances of time, shown in Fig. 7.12, support the above observation. The direction of the displacement vectors proves that the individual blocks at the top part of the scarp are the first to slide downward along the main fault surface. Consequently, the movement of the top blocks caused the bottom

blocks to begin sliding along the ‘valley’ created by the two failure surfaces at the bottom part of the scarp. In addition, the displacement vectors at the latter instance of time indicate that indeed some blocks tended to spread to the sides, some passing over the scarp edges at the bottom part of the scarp.

Unfortunately, due to time limitations, the debris flow simulation could not be performed long enough until the full extent of the slide could be verified. However, field observations and witness accounts indicate that the slide traveled as much as 3 km past the top part of the scarp. The general behavior of the debris indicates that the material is moving in the expected manner and thus further analysis could verify the full extent of the slide. Additionally, witness accounts of flying boulders and pieces of rock could not be verified since dynamic simulation of the debris flow was not carried out.

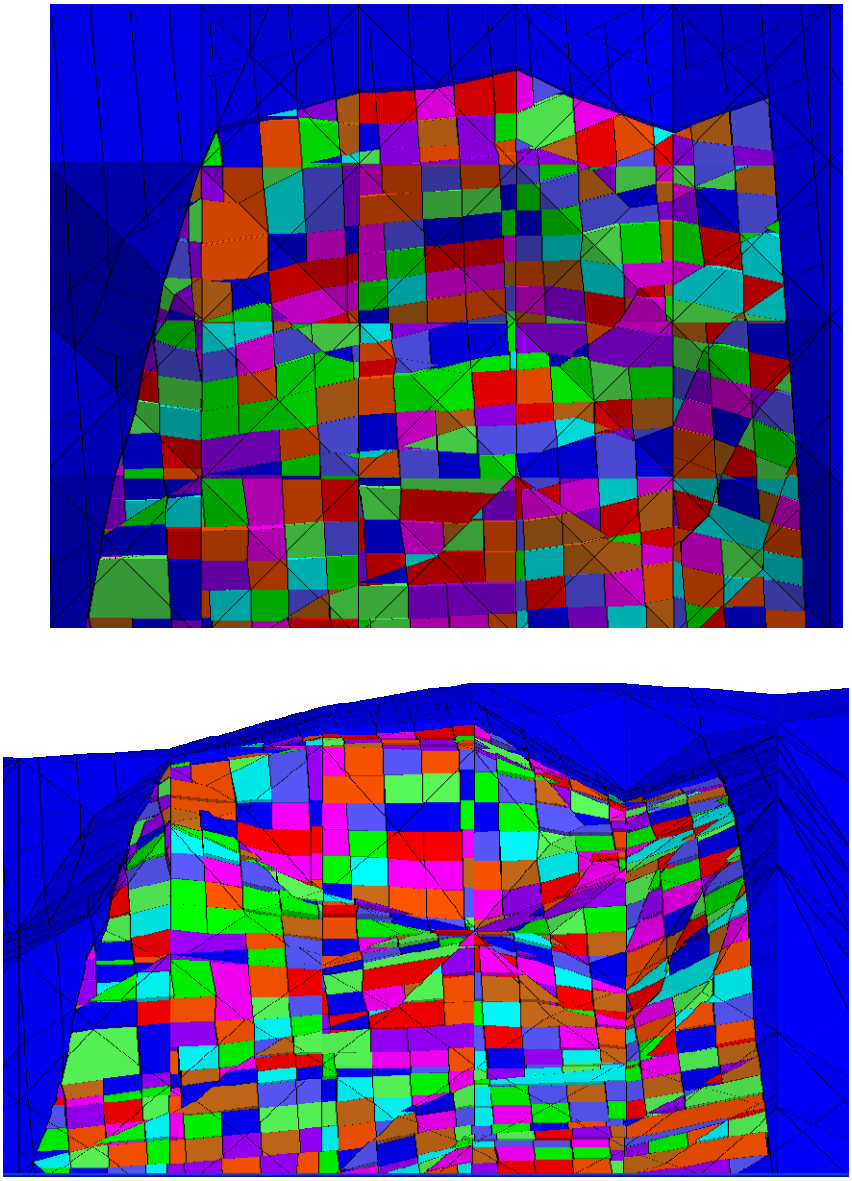

Fig. 7.4 - Plan and front view of top section of failing block showing the initial stages of disintegration of the block at the top part of the rock mass, mainly along the horizontal fracture sets.

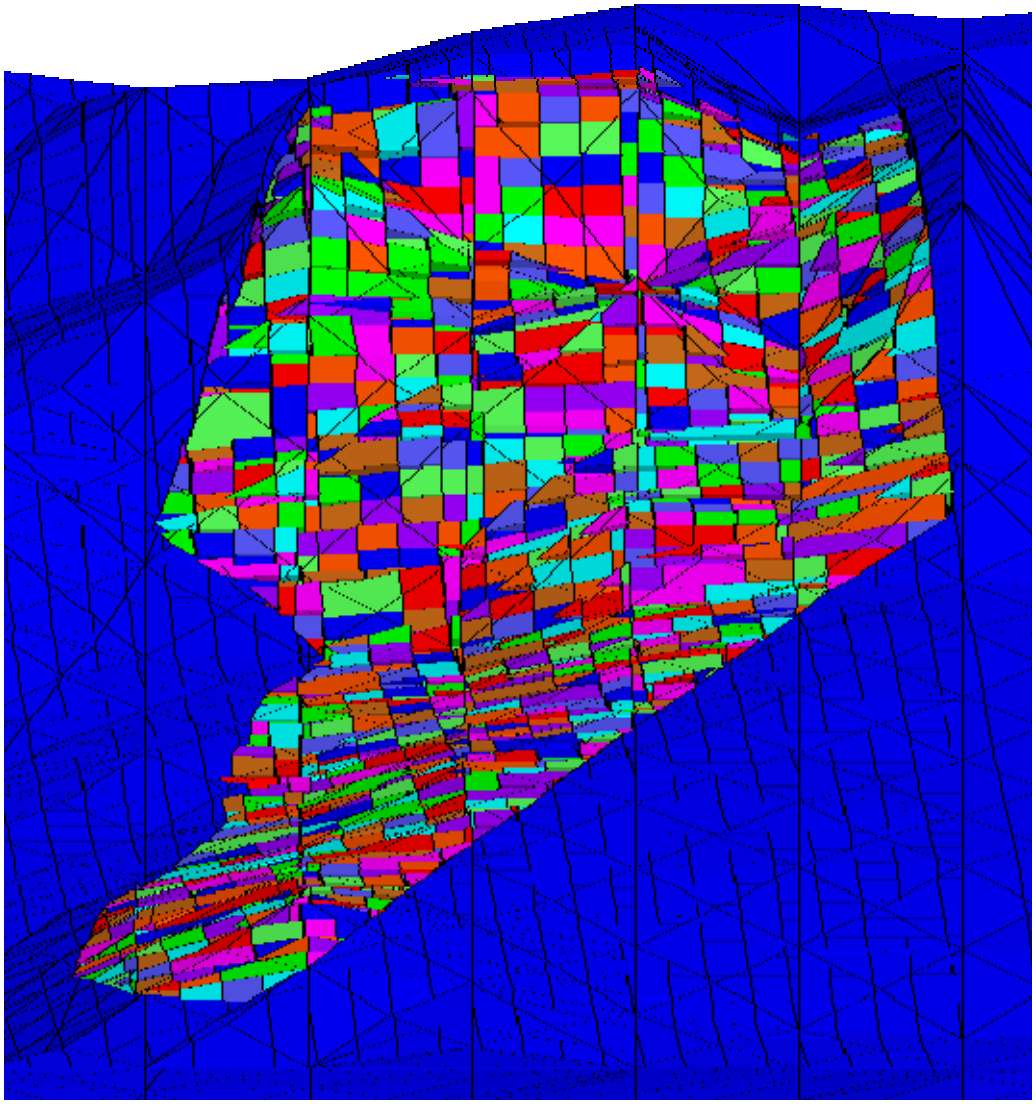

Fig. 7.5 - Initial stages of disintegration showing most disintegration at the top and initiation of sliding along the main fault dip direction.

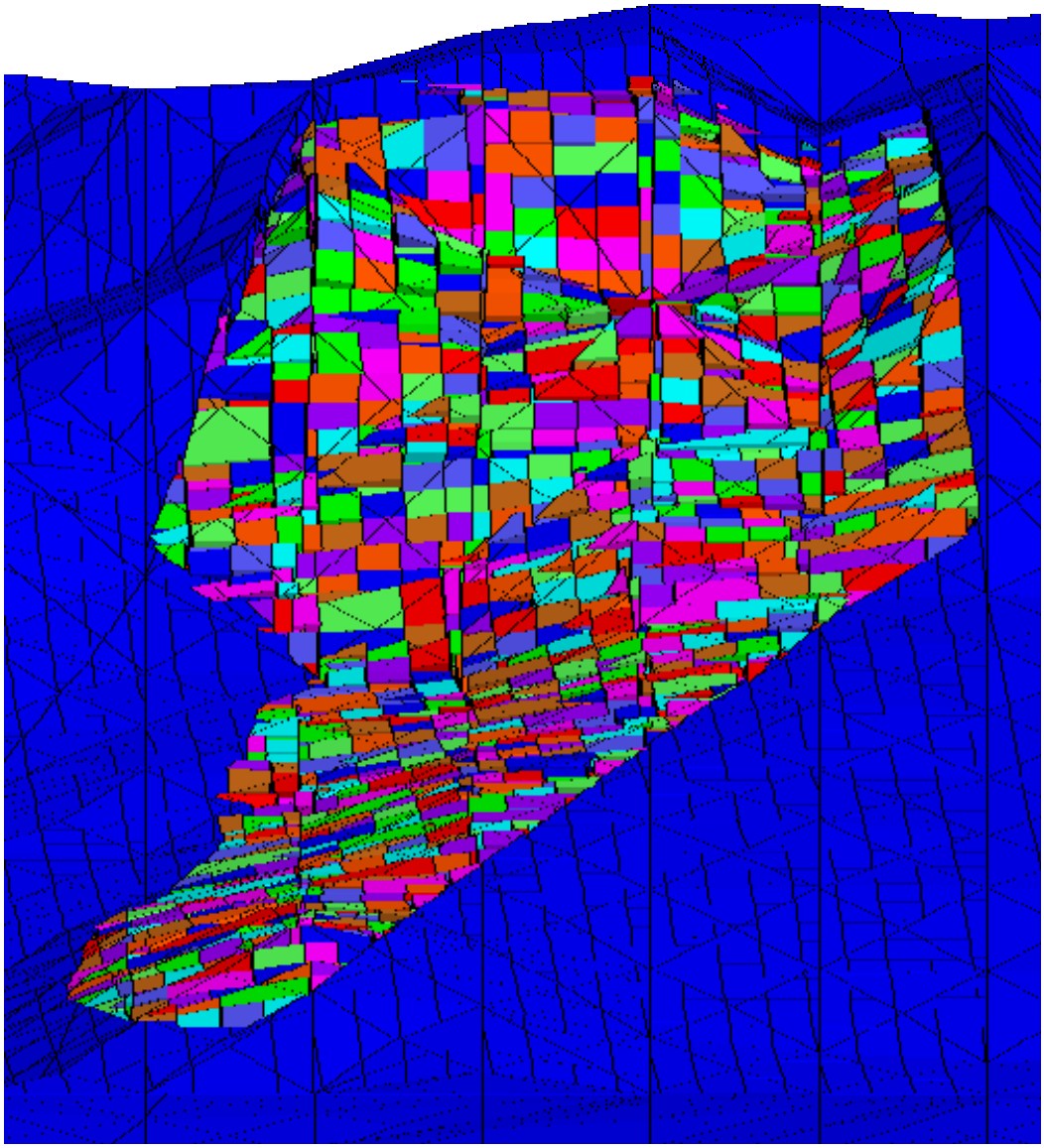

Fig. 7.6 - Disintegration of middle section of rock mass has been initiated. Movement at the top part has increased.

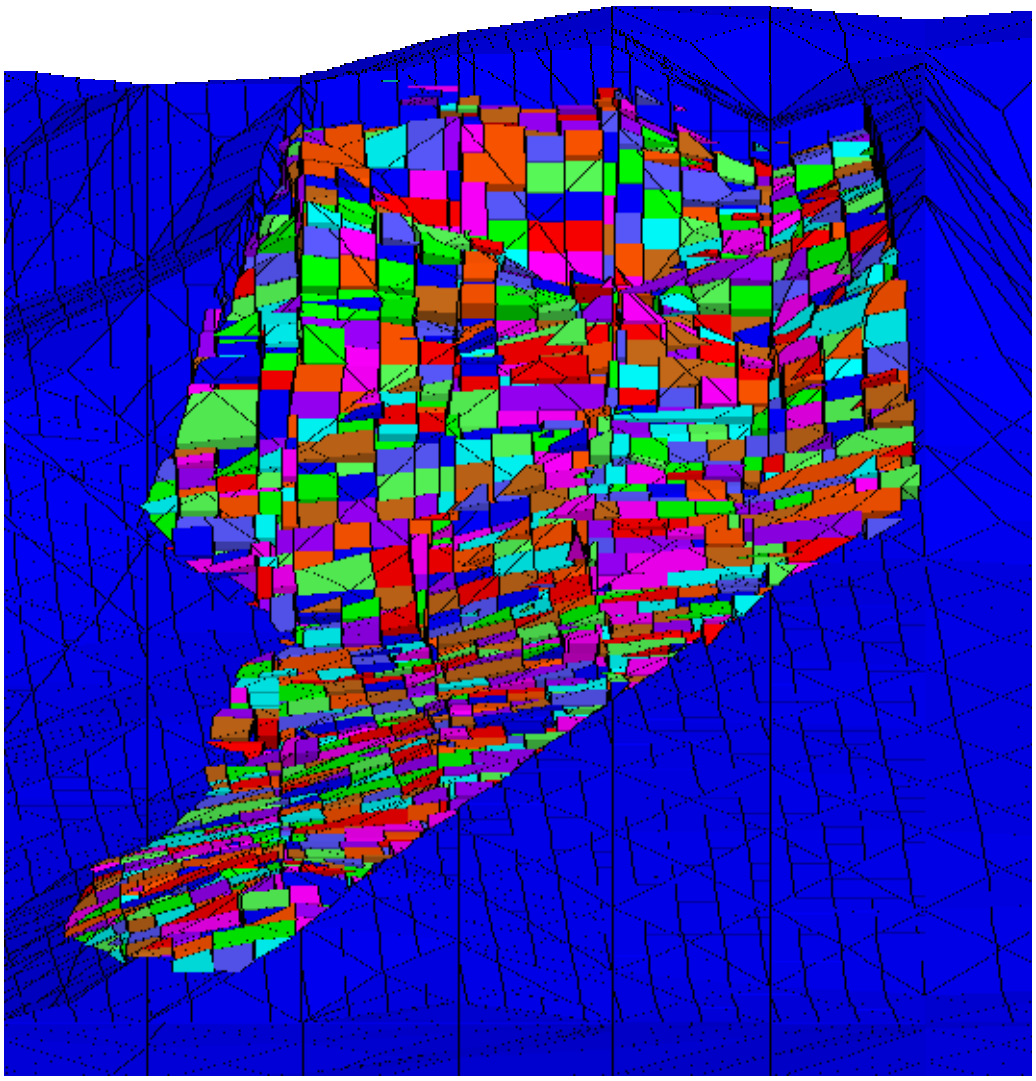

Fig. 7.7 - Bottom part of rock mass has also disintegrated. Movement has progressed and side blocks are beginning to spread laterally.

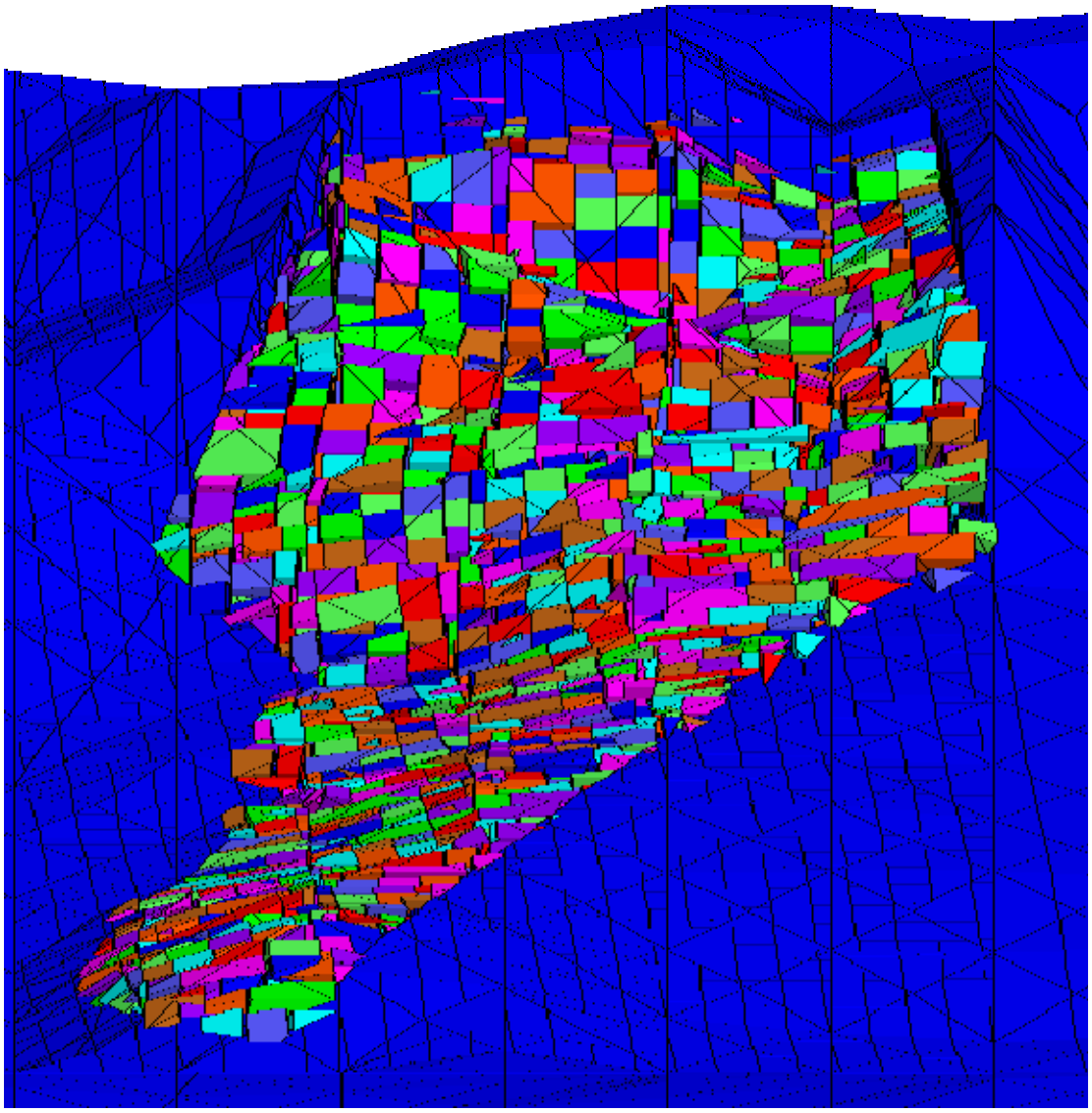

Fig. 7.8 - Top part of the rock mass has slid approximately 100m along the main fault. Bottom blocks have slid out of the scarp edges.

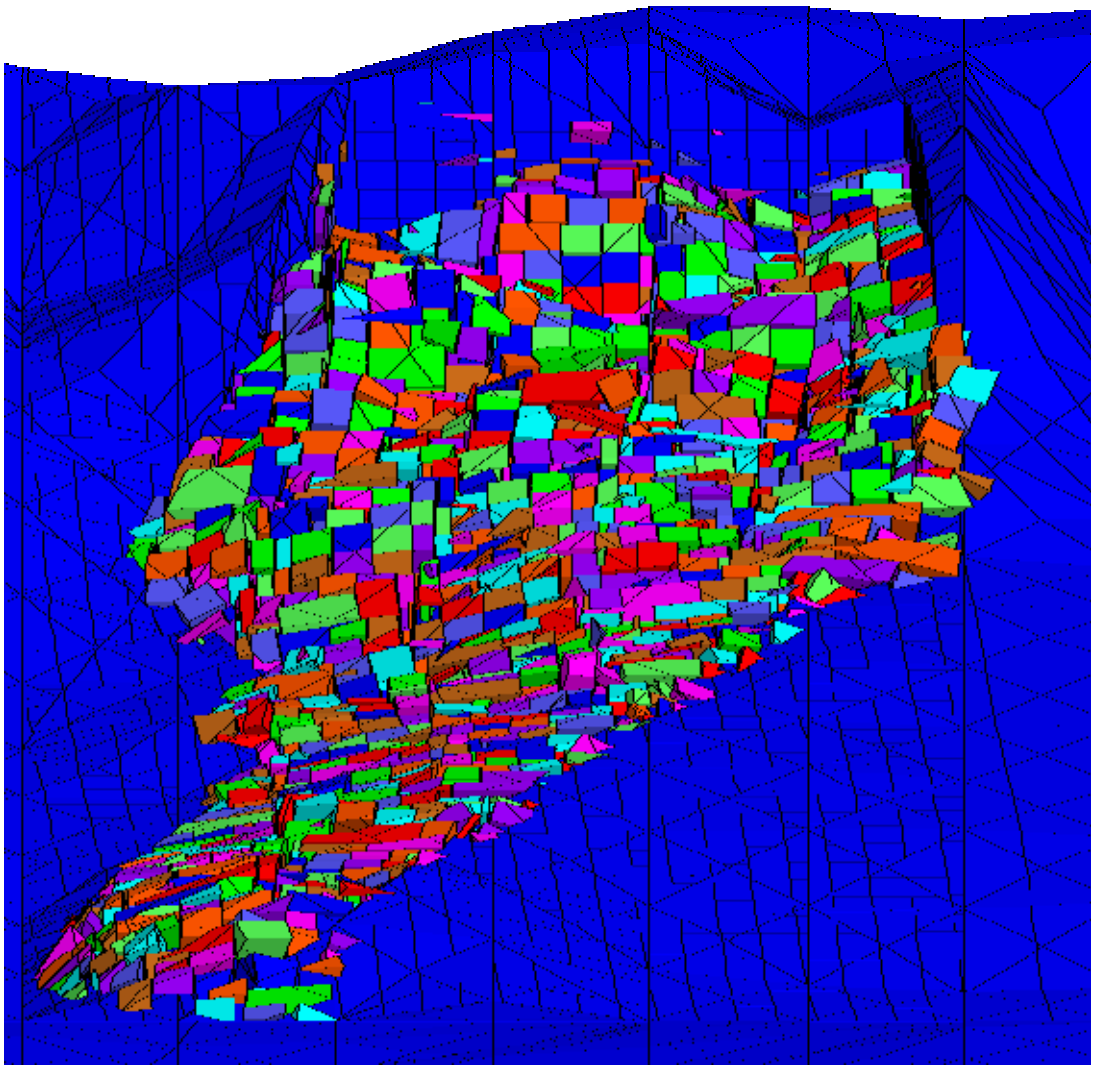

Fig. 7.9 - Direction of flow along the ‘valley’. Side blocks are tending to spread laterally, flowing over the scarp edges.

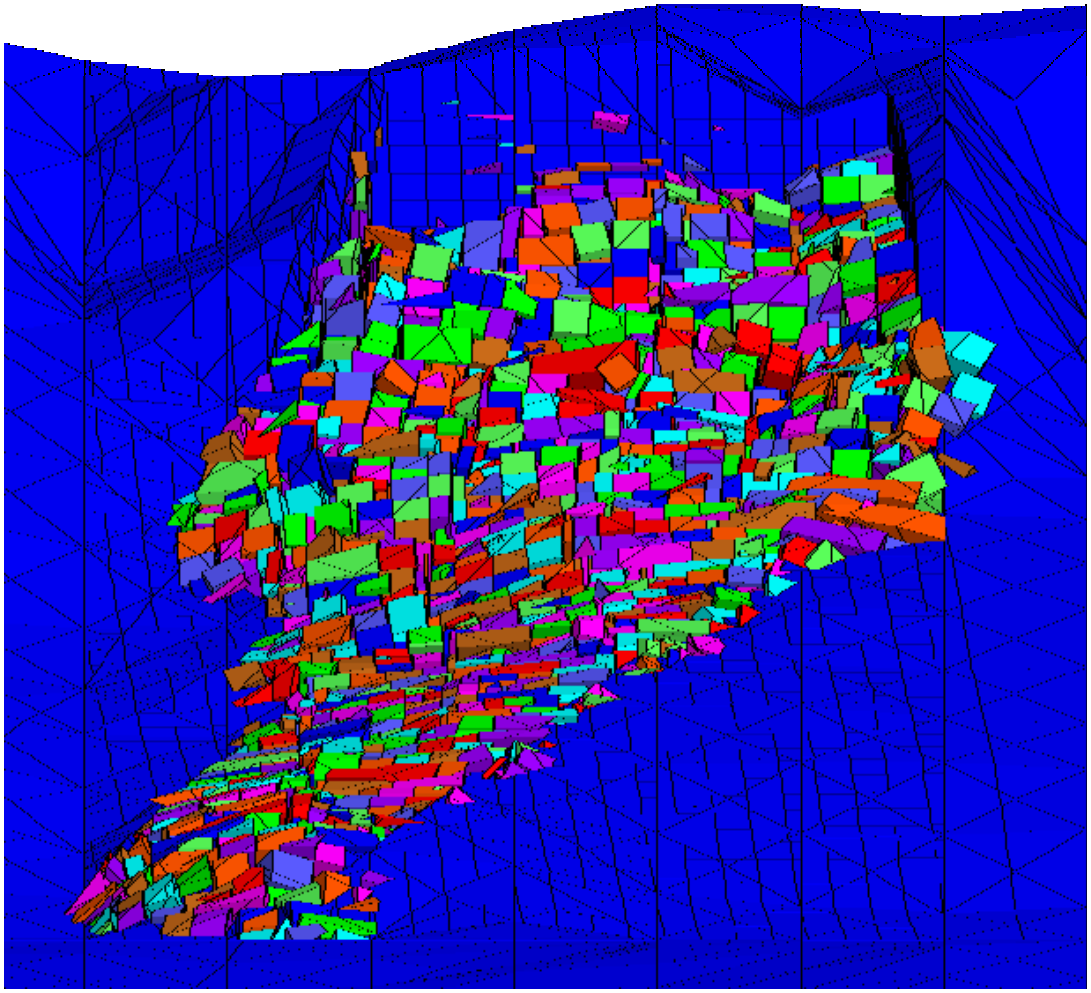

Fig. 7.10a - Final stage of debris flow simulation.

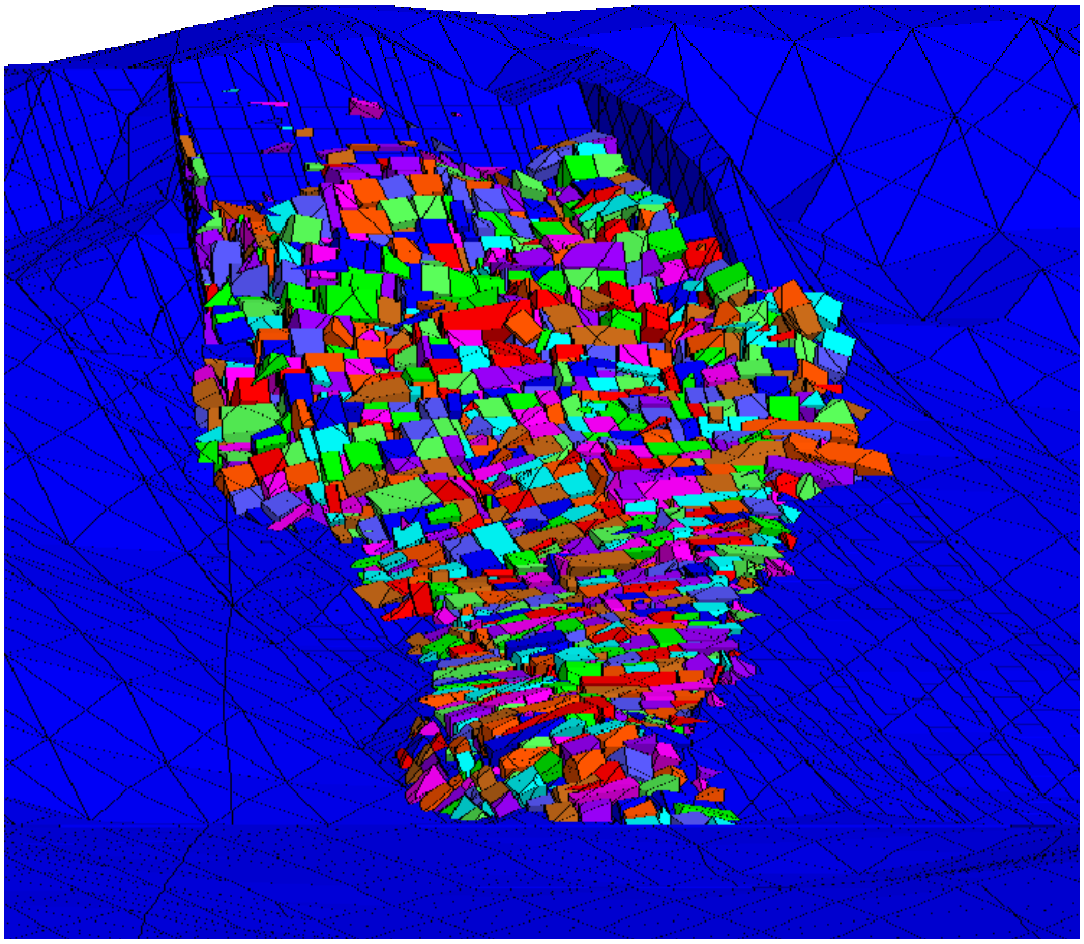

Fig. 7.10b - Final stage of debris flow simulation showing direction of flow.

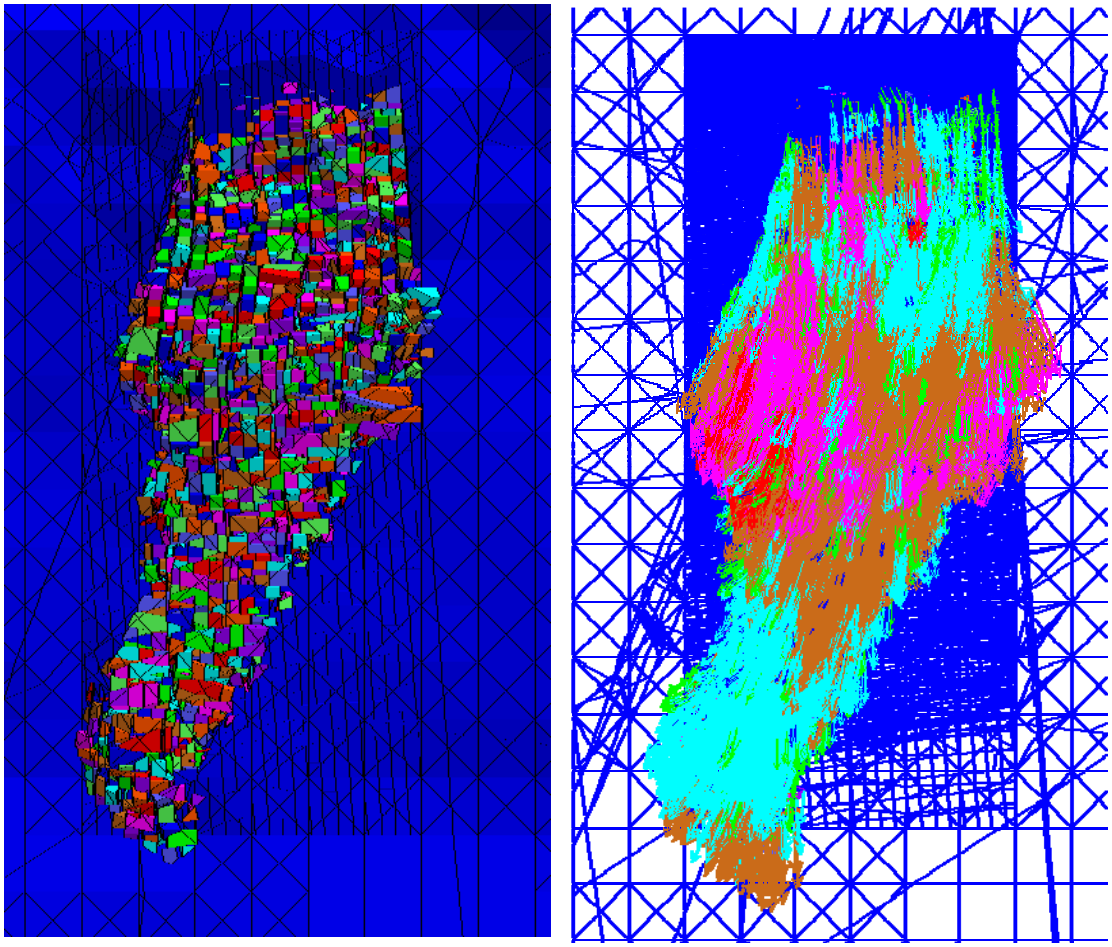

Fig. 7.11 - Plan view of the final stage of debris flow showing corresponding displacement vectors.

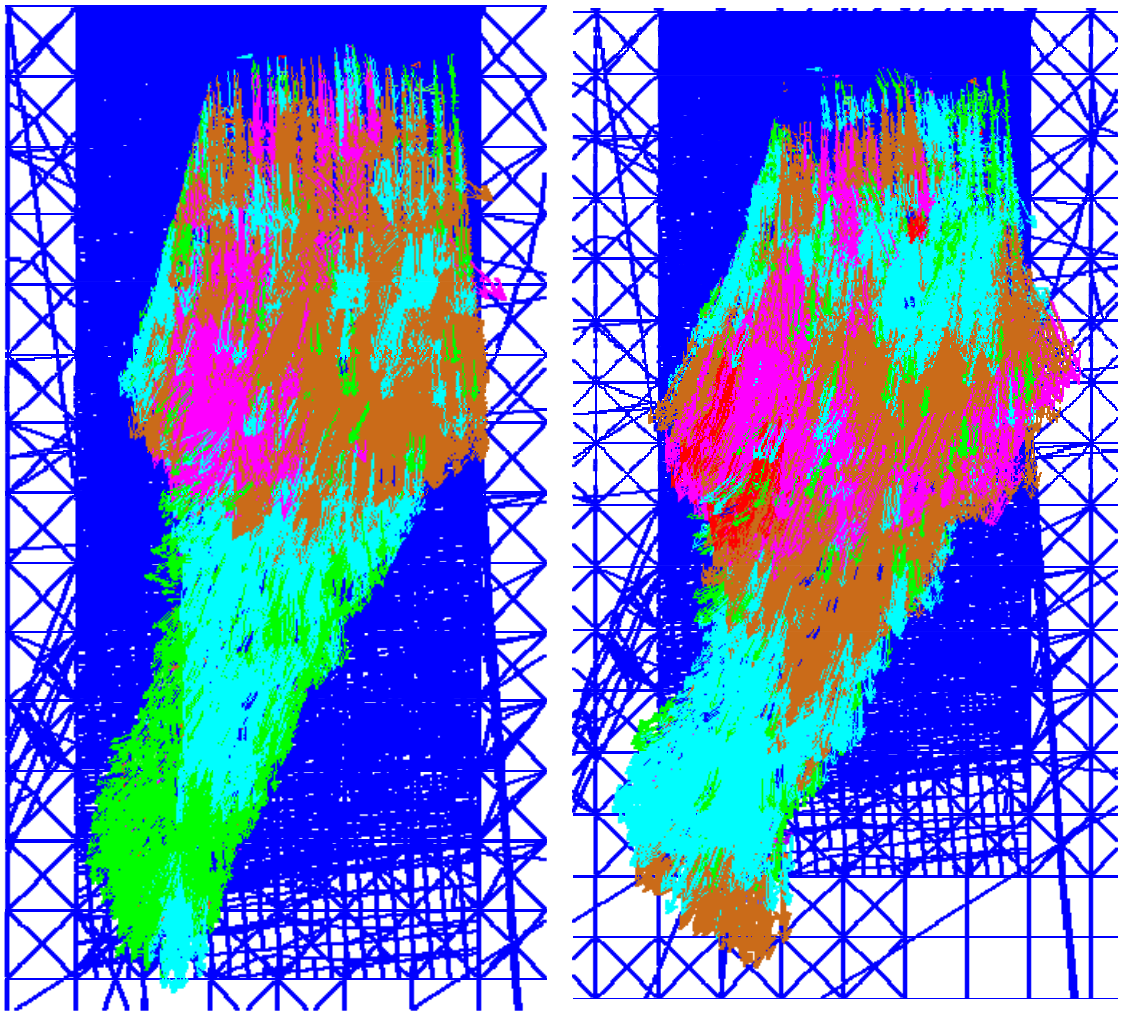

Fig. 7.12 - Initial and Final displacement vectors indicating some lateral spread of the disintegrated blocks.

CHAPTER 8: SUMMARY AND CONCLUSIONS

This study involved performing a series of distinct element analyses of the February 17th, 2006, Leyte, Philippines rockslide using the three-dimensional distinct element code 3DEC. The slide was one of the largest slides in recent history and caused the death of close to 1,500 people by inundating the village of Guinsaugon which was located at the foot of the slide. Three-dimensional distinct element simulations of the slide were executed to obtain a better understanding of the mechanisms responsible for the triggering of the slide and behavior of the debris flow.

The two mechanisms that were investigated as possible triggering causes of the slide were the rainfall-induced hydraulic pressurization of the main fault surface that is part of the main scarp, as well as earthquake-induced horizontal accelerations along the main fault. The main conclusions from the numerical simulations of the Guinsaugon slide are summarized as follows:

1. The rockslide initially occurred due to slip or activation of a fault, which is a splay of the PFZ, and the downwards movement of an overhanging rock along fault dip direction. Following slippage along the fault, a vertical shear failure plane was created causing the overhanging rock to be separated from the face of the mountain. The falling rock then slid along the bedding plane at the base of the overhanging rock, and started to disintegrate to create a rock avalanche and debris flow. The overhanging block experienced almost no rotation indicating that the block did not initially topple or overturn.

2. The triggering mechanism of the slide was determined to be the hydraulic pressurization of the fault due to heavy rainfall in the area the week prior to the slide. This triggering mechanism assumes that the main was full of rain water such that it creates sufficient linearly varying hydrostatic pressure to induce triggering of the slide. Full hydraulic pressurization of the fault was deemed feasible following several days of rainfall, which accumulated to about 70 cm, prior to the rockslide.

3. The earthquake analysis indicates that the maximum seismic horizontal acceleration measured by the earthquake recording stations in the area had little or no effect on the triggering of the slide when considered in addition to the rainfall-induced hydraulic pressurization of the fault.

4. The debris flow simulation indicates that once initiated, the individual blocks at the top of the overhanging failing rock mass initially move downward along the main fault surface and in the fault dip direction. The top blocks then caused bulging at the bottom part of the failing rock mass thus causing the bottom blocks to tend to slide along and in the direction of the 'valley' at the bottom of the scarp.

5. The three-dimensional distinct element code, 3DEC, which was used in this analysis is a powerful tool in analysis of rock slope failures and rockslides. The code is capable of analyzing a debris flow and depicting the behavior of individual blocks, which requires tremendous calculation abilities.

The majority of the results obtained from the distinct element simulations of the Guinsaugon rockslide are consistent with witness accounts and field observations. However, it must be noted that the results are highly depended on the material and joint shear strength properties as well as the geometry of the 3DEC model. Also, in the case of the debris flow simulation, time constraints and limitation of computational resources have not allowed accurate representation of the real joint sets and the very small spacing in the field. However, the initial behavior of the debris has been evaluated.

The use of distinct element simulations in back-analysis of rockslides and rock slope failures have the potential of becoming very useful analysis tools possibly used in mitigation of such events. Such as in the Guinsaugon rockslide case, distinct element simulations can be used to gain a better understanding of the early signs of such a disaster in order to develop a warning system and awareness program that will prevent such catastrophes in the future. In light of better computational resources, such simulations could also seem useful in rescue operations in the aftermath of events like the Guinsaugon rockslide. The simulations could be used to determine whether buildings and other structures have been moved by the impact of the debris and also if such structures have remained intact. In this case for example, such capability could

have potentially saved many lives of victims who were trapped in buildings for days helplessly waiting for rescue teams. However, the available computational resources and hardware available at the time sadly do not allow for such analyses to be performed in such a short period of time.

REFERENCES

1. Barrier, E., Huchon, P. and Aurelio, M.A. (1991). Philippine Fault: A key for Philippine Kinematics, Geology, Vol. 19, pp. 32-35.
2. Barton, N.R. (1973), "Review of a New Shear Strength Criterion for Rock Joints," Engineering Geology, Vol. 7
3. Barton, N.R. (1974), "A Review of Shear Strength of Filled Discontinuities in Rock," Norwegian Geotechnic Institute, Publication No. 105, Oslo, Norway
4. Barton, N.R. and Bandis S.C. (1982), "Effects of Block Size on the Shear Behavior of Jointed Rock," 23rd U.S. Symposium on Rock Mechanics, Berkley, pp. 739-760
5. Barton, N.R. and Choubey, V. (1977), "The Shear Strength of Rock Joints in Theory and Practice," Rock Mechanics, Vol. 10,
6. Besana, G.M. and Ando, M. (2005), The central Philippine Fault Zone: Location of great earthquakes, slow events, and creep activity, Earth, Planets and Space, Vol. 57, pp. 987-994.
7. Cundall, P.A. (1971). Proc. Symp. ISRM, Vol.1, France, 1971.
8. Cundall, P.A. (1988). Formulation of a Three-dimensional Distinct Element Model – Part 1. A Scheme to Detect and Represent Contracts in a System Composed of Many Polyhedral Blocks. Int. J. Rock Mech. Min. Sci. & Geomech. Vol 25, pp. 107-116, 1988.
9. Cundall, P.A., (1987). Distinct Element Models of Rock and Soil Structure. Analytical and Computational Methods in Engineering Rock Mechanics, George Allen and Unwin, pp. 129-163, London, 1987.
10. Cundall, P.A., Strack, O.D.L. (1979). A discrete numerical model for granular assemblies. Geotechnique, Vol. 29, pp. 47-65, 1979.
11. DOST – PAGASA. (2004). Climate of the Philippines. http://www.pagasa.dost.gov.ph/cab/climate.htm
12. DPRI (2006), Philippine, Southern Leyte Landslide Preliminary Report, Disaster Prevention Research Institute, University of Kyoto, March 31, 2006, 30 p.
13. Duquesnoy, T., Barrier, E., Kasser, M., Aurelio, M.A., Gaulon, R., Punongbayan, Rangin, C., and the French-Philippine Cooperation team. (1994). Detection of creep along the Philippine Fault; first results of geodetic measurements on Leyte Island, central Philippine. Geophys. Res. Lett., Vol. 21, pp. 975-978, 1994.

14. Farmer, B.M. (2006). Laboratory Testing for the Leyte, Philippines Rockslide Analysis, Project report submitted in partial fulfillment of the degree of Master of Science, Virginia Tech, December 2006.
15. Google Earth. (2007). 2007 Europa Technologies, Image TerraMetrics, 2007.
16. Google Maps. (2007). Google Imagery 2007, NASA http://maps.google.com/maps?f=q&hl=en&q=philippines&ie=UTF8&t=k&z=5&om=1
17. Gutierrez, M. S. (2006), unpublished photographs of the rockslide site, personal communication
18. Gutierrez, M. S., Schaefer, V.R., Dupio, A., Cardiel, G. (2006). Reconnaissance Survey and Numerical Modeling of the February 17, 2006, Leyte, Landslide. Unpublished report, May 2006.
19. Inter-agency Committee on the Guinsaugon, Southern Leyte, Leyte Tragedy (2006). The 17 February Bgry. Guinsaugon, Southern Leyte, Landslide. Government of the Philippines, 18 p. February 28, 2006.
20. Itasca (1998). 3DEC – Three-Dimensional Distinct Element Code – Command Reference Itasca Consulting Group, Inc., 1998.
21. Itasca (1998). 3DEC – Three-Dimensional Distinct Element Code – Theory and Background. Itasca Consulting Group, Inc., 1998.
22. Itasca (1998). 3DEC – Three-Dimensional Distinct Element Code – User' Guide. Itasca Consulting Group, Inc., 1998.
23. Itasca (1998). 3DEC – Three-Dimensional Distinct Element Code – Verification problems and example applications. Itasca Consulting Group, Inc., 1998.
24. Karolewski, M. (2002). Tracer v.1.6.1, July 2002.
25. Lagmay, A.M.F., Ong, J.B.T., Fernandez, D.F.D., Lapus, M.R., Rodolfo, R.S., Tengonciang, A.M.P., Soria, J.L.A., Baliatan, E.G., Quimba, Z.L., Uichianco, C.L., Pagluican, E.M.R., Remedio, A.R.C., Lorenzo, G.R.H., Valdivia, W., and Avila, F.B. (2006). Scientists investigate recent Philippine landslide. Eos, Vol. 87, p. 121-124, 2006.
26. Lama, R.D., Vutukuri, V.S. (1978). Handbook on Mechanical Properties of Rocks – Testing Techniques and Results – Volume IV. Series on Rock and Soil Mechanics, Vol. 3, No. 3, 1978.
27. Lee, K. L. and Duncan, J. M. (1975). Landslide of April 25, 1974 on the Mantaro River, Peru. National Academy of Sciences, Washington, D.C., 1975.

28. Lorig, L.J., Hart, R.D., and Cundall, P.A. (1991). Slope Stability Analysis of Jointed Rock Using the Distinct Element Method. Transportation Research Record 1330. TRB, National Research Council, pp. 1-9, Washington, D.C., 1991.
29. Mathworks, Inc., The, (2004). Matlab v. 7.0 (R14), May 06, 2004.
30. NASA. (2005). http://earthobservatory.nasa.gov/NaturalHazards/shownh.php3?img_id=13374
31. NOAA. (2005). http://www.elnino.noaa.gov/
32. Norrish, N. I. and Wyllie, D. C. (1996). Landslides Investigation and Mitigation. Transportation Research Board, Special Report 247, National Research Council, pp. 391-425, National Academy Press, Washington, D.C., 1996
33. Orense, R.P., Sapuay, S.E. (2006). Preliminary Report on the 17 February 2006 Leyte, Philippines Landslide. Soils and Foundations - Japanese Geotechnical Society, Vol. 46, No. 5, pp. 693-701, October 2006.
34. Rigo, M.L., Pinheiro, R.J.B., Bressani, L.A., Bica, A.V.D., and da Silveira, R.M. (2006). The residual shear strength of tropical soils. NRC Research Press Website, http://cgj.nrc.ca , March 2006.
35. Stone, R. (2006). Too Late, Earth Scans Reveal the Power of a Killer Landslide. Science, vol. 311, no. 5769, pp. 1844-1845, March 31, 2006
36. Tamaoki, H. (2006), “The Philippines, Southern Leyte Landslide: Preliminary Landslide Investigation,” Unpublished Report, MatLabo Company, 2006.
37. U.S Department of Defense (2006). U.S. Forces Help Victims of Leyte Island Landslide. http://www.defenselink.mil/home/features/Leyte/landslide/
38. UNOSTAT. (2005), http://unosat.web.cern.ch/unosat/asp /prod_free.asp?id=46
39. USGS (2002). http://volcanoes.usgs.gov/Hazards/What/Landslides/MSHSlide.html
40. Velasco, A.A., Ammon, C.J., Lay, T., and Hagerty, M. (1996). Rupture process of the 1990 Luzon, Philippines (Mw=7.7), earthquake. Journal Geophys. Res., Vol. 101 (B10), pp. 22 419- 22 434, 1996.
41. Weingarten, J.S., Perkins, T.K. (1995). Prediction of sand production in gas wells: methods and Gulf of Mexico case studies. J. Petrol Tech, pp. 596-600, 1995.
42. Wikipedia. (2007). Philippines Physical Map, http://en.wikipedia.org/wiki/Image:Ph_physical_map.png

APPENDIX

A. ROCKSLIDE PICTURES

Pictures courtesy of M. S. Gutierrez (Gutierrez, 2006).

B.1 GEOMETRY INPUT FILE IN 3DEC

```
new
;
pol pri a 1000.0  0.0 1600.0  1100.0  0.0 1600.0 &
          1100.0 750.0 1600.0  1000.0 720.4 1600.0 &
        b 1000.0  0.0 1700.0  1100.0  0.0 1700.0 &
          1100.0 750.0 1700.0  1000.0 730.9 1700.0
pol pri a 1000.0  0.0 1700.0  1100.0  0.0 1700.0 &
          1100.0 750.0 1700.0  1000.0 730.9 1700.0 &
        b 1000.0  0.0 1800.0  1100.0  0.0 1800.0 &
          1100.0 750.0 1800.0  1000.0 749.2 1800.0
pol pri a 1000.0  0.0 1800.0  1100.0  0.0 1800.0 &
          1100.0 750.0 1800.0  1000.0 749.2 1800.0 &
        b 1000.0  0.0 1900.0  1100.0  0.0 1900.0 &
          1100.0 757.9 1900.0  1000.0 753.0 1900.0
pol pri a 1000.0  0.0 1900.0  1100.0  0.0 1900.0 &
          1100.0 757.9 1900.0  1000.0 753.0 1900.0 &
        b 1000.0  0.0 2000.0  1100.0  0.0 2000.0 &
          1100.0 795.3 2000.0  1000.0 784.1 2000.0
pol pri a 1000.0  0.0 2000.0  1100.0  0.0 2000.0 &
          1100.0 795.3 2000.0  1000.0 784.1 2000.0 &
        b 1000.0  0.0 2100.0  1100.0  0.0 2100.0 &
          1100.0 800.0 2100.0  1000.0 800.0 2100.0
                               [...]
pol pri a 3700.0  0.0 3200.0  3800.0  0.0 3200.0 &
          3800.0 61.0 3200.0  3700.0 84.8 3200.0 &
        b 3700.0  0.0 3300.0  3800.0  0.0 3300.0 &
          3800.0 58.9 3300.0  3700.0 77.5 3300.0
pol pri a 3700.0  0.0 3300.0  3800.0  0.0 3300.0 &
          3800.0 58.9 3300.0  3700.0 77.5 3300.0 &
        b 3700.0  0.0 3400.0  3800.0  0.0 3400.0 &
          3800.0 58.1 3400.0  3700.0 80.6 3400.0
pol pri a 3700.0  0.0 3400.0  3800.0  0.0 3400.0 &
          3800.0 58.1 3400.0  3700.0 80.6 3400.0 &
        b 3700.0  0.0 3500.0  3800.0  0.0 3500.0 &
          3800.0 64.8 3500.0  3700.0 86.0 3500.0
pol pri a 3700.0  0.0 3500.0  3800.0  0.0 3500.0 &
          3800.0 64.8 3500.0  3700.0 86.0 3500.0 &
        b 3700.0  0.0 3600.0  3800.0  0.0 3600.0 &
          3800.0 72.5 3600.0  3700.0 91.3 3600.0
pol pri a 3700.0  0.0 3600.0  3800.0  0.0 3600.0 &
          3800.0 72.5 3600.0  3700.0 91.3 3600.0 &
        b 3700.0  0.0 3700.0  3800.0  0.0 3700.0 &
          3800.0 83.7 3700.0  3700.0 100.8 3700.0
pol pri a 3700.0  0.0 3700.0  3800.0  0.0 3700.0 &
          3800.0 83.7 3700.0  3700.0 100.8 3700.0 &
        b 3700.0  0.0 3800.0  3800.0  0.0 3800.0 &
          3800.0 96.8 3800.0  3700.0 112.4 3800.0

save geom.sav
ret
```

B.2 MAIN INPUT 3DEC FILE

- Scenario A: Model Definition and Consolidation under in-situ stresses

```
; fault.dat P2 (final geometry, block moist weight)
rest geom.sav
;
;join
;
set ismax 3300000
;
; add boundary blocks
;
poly bri 1000 3800 -100   0 1600 3800 ; base
poly bri  900 1000 -100 800 1600 3800 ; west wall
poly bri 1000 3800 -100 800 1500 1600 ; south wall
poly bri 1000 3800 -100 800 3800 3900 ; north wall
;
mark 1000 3800 -100   0 1600 3800 region=1 ; base
mark  900 1000 -100 800 1600 3800 region=2 ; west wall
mark 1000 3800 -100 800 1500 1600 region=3 ; south wall
mark 1000 3800 -100 800 3800 3900 region=4 ; north wall
;
hide reg 1 2 3 4
;
;  create failure planes
;
jset dd  85 dip 48 org 1250 760 2942 ; main fault
jset dd  25 dip 75 org 1380 760 2660 ; main fault - fault 2
jset dd 175 dip 88 org 1572 500 3080 ; vertical shear fail. plane
jset dd  57 dip 25 org 1622 540  2450 ; fault 4 - left valley
jset dd 172 dip 29 org 1922 470  3085 ; fault 5 - right valley
;
jset dd  95 dip  8 org 1900 280 2700 ; 8 degree plane
jset dd   0 dip  0 org 1900 150 2700 ; glued horizontal plane
;
;
hide xr 1000,1100
hide xr 2200,3900
hide zr 1000,2500
hide zr 3000,3300
hide yr    0  300
;
;
;  assign material properties
;
seek
change dd  85 dip 48 org 1250 760 2942 below mat=2; main fault
change dd  25 dip 75 org 1380 760 2660 below mat=2; fault 2
change dd 175 dip 88 org 1572 500 3080 below mat=2; vert. sh. Pl.
change dd  57 dip 25 org 1622 540 2450 below mat=2; left valley
change dd 172 dip 29 org 1922 470 3085 below mat=2; right valley
;
change dd  95 dip  8 org 1900 280 2700 below mat=2; 8 deg plane
change dd   0 dip  0 org 1900 150 2700 below mat=2; glued hor.pl.
;
change jcons=7 jmat=1
;
```

```
; boundary conditions
;
fix region 1
fix region 2
fix region 3
fix region 4
;
hide mat=1
hide reg 1 2 3 4
join
seek
;
;
;assign material properties
;
prop mat=1 dens=2600   ;falling block moist weight

prop mat=2 dens=2000
;
prop jmat=1 kn=1e12 ks=1e12
;
;
; assign joint material properties
;
change mint 1 2 jmat=3 jcons=1;  actual faults
prop jmat=3 kn=1e9 ks=1e9 f=90
;
;
; apply gravity
;
grav 0 -10 0
;
;
; assign in-situ stress
;
insitu topo kox 0.25 koy 0.25
;
;
hide region 1 2 3 4
;
hist yvel (1500,600,2750) type 1
hist unbal type 2
hist xvel (1300 760 2900) type 3   ;point on block
hist yvel (1300 760 2900) type 4   ;point on block
;
step 5000
;
save fault.sav
;
ret
```

B.3 TRIGGERING ANALYSIS: 3DEC FILES – FAULT PRESSURIZATION ONLY

- Scenario B: Reduce Shear Strength to Actual (Peak)

```
; fail0.dat
;
rest fault.sav
;
reset disp
hist yvel (1500,600,2750) type 5
hist unbal type 6
hist xdis (1242 776 2900) type 7  ;top point
hist ydis (1242 776 2900) type 8  ;top point
;
;change mint 1 1 jmat=2 jcons=1; fractures in falling block
;prop jmat=2 kn=1e9 ks=1e9 f=0
;
change mint 1 2 jmat=3 jcons=1;  actual faults
prop jmat=3 kn=1e9 ks=1e9 fr=39
;
change dd  85 dip 48 org 1250 760 2942 jmat=4 jcons=1; main fault
prop jmat=4 kn=1e9 ks=1e9 fr=25
;
change dd 175 dip 88 org 1572 500 3080 jmat=5 jcons=1; vertical
surface
prop jmat=5 kn=1e9 ks=1e9 fr=33 jco=6.7e6 jte=3e6
;
step 2000
save fail0.sav
ret
```

- Scenario C1: Increase pore pressure to equivalent to ¼ of fault height

```
; fail1.dat
;
rest fail0.sav

reset disp
hist yvel (1500,600,2750) type 5
hist unbal type 6
hist xdis (1242 776 2900) type 7  ;top point
hist ydis (1242 776 2900) type 8  ;top point
;
; apply pore pressure in the main fault (equivalent to .25 of
fault height)
;
insitu dd  85 dip 48 org 1250 760 2942 pp 5135200 pgrad 0 -9800 0
;
step 5000
save fail1.sav
;
ret
```

- Scenario C2: Increase pore pressure to equivalent to ½ of fault height

```
; fail2.dat
;
rest fail1.sav
;
; apply pore pressure in the main fault (equivalent to .5 of
fault height)
;
insitu dd  85 dip 48 org 1250 760 2942 pp 0
insitu dd  85 dip 48 org 1250 760 2942 pp 5958400 pgrad 0 -9800 0
;
step 5000
save fail2.sav
;
ret
```

- Scenario C3: Increase pore pressure to equivalent to ¾ of fault height

```
; fail3.dat
;
rest fail2.sav
;
; apply pore pressure in the main fault (equivalent to .75 of
fault height)
;
insitu dd  85 dip 48 org 1250 760 2942 pp 0
insitu dd  85 dip 48 org 1250 760 2942 pp 6781600 pgrad 0 -9800 0
;
step 5000
save fail3.sav
;
ret
```

- Scenario C4: Increase pore pressure to equivalent to full fault height

```
; fail4.dat
;
rest fail3.sav
;
; apply pore pressure in the main fault
;
insitu dd  85 dip 48 org 1250 760 2942 pp 0
insitu dd  85 dip 48 org 1250 760 2942 pp 7604800 pgrad 0 -9800 0
;
step 5000
save fail4.sav
;
ret
```

- Scenario D2: Change shear strength to residual

```
rest fail4.sav
;
; change properties to residual
;
change mint 1 2 jmat=3 jcons=1;  actual faults
prop jmat=3 kn=1e9 ks=1e9 fr=30
;
;change dd  85 dip 48 org 1250 760 2942 jmat=4 jcons=1; main
fault
;prop jmat=4 kn=1e9 ks=1e9 fr=25
;
change dd 175 dip 88 org 1572 500 3080 jmat=5 jcons=1; vertical
surface
prop jmat=5 kn=1e9 ks=1e9 fr=33
;
step 2000
save fail4b0.sav
;
ret
```

- Scenario D2b: Release pore pressures in main fault

```
rest fail4b0.sav
;
; pore pressures dissipate
;
insitu dd  85 dip 48 org 1250 760 2942 pp 0
;
step 5000
save fail4b.sav
;
ret
```

B.4 TRIGGERING ANALYSIS: 3DEC FILES-EARTHQUAKE & PRESSURIZATION

- Scenario EQ1:

```
rest fail4b.sav
;
; apply earthquake for 0.01 sec
;
grav 0, -10, -1

step 4750
save eq2.sav

ret
```

- Scenario EQ2:

```
rest fail4.sav
;
;
; pore pressures dissipate
;
insitu dd  85 dip 48 org 1250 760 2942 pp 0
;
;
;apply earthquake for 0.01 sec
;
grav 0, -10, -1

step 4750
save eq1.sav

ret
```

- Scenario EQ3:

```
rest fail4.sav
;
;
;apply earthquake for 0.01 sec
;
grav 0, -10, -1

step 4750
save eq3.sav

ret
```